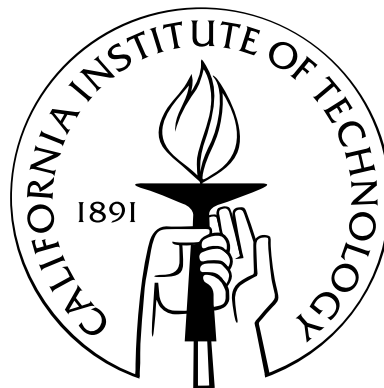


# Coulomb drag and tunneling studies in quantum Hall bilayers

Thesis by

Debaleena Nandi

In Partial Fulfillment of the Requirements  
for the Degree of  
Doctor of Philosophy



California Institute of Technology  
Pasadena, California

2016

(Defended September 18th, 2015)

© 2016

Debaleena Nandi

All Rights Reserved

# Acknowledgements

I am deeply grateful to my PhD advisor Jim Eisenstein for sharing his profound knowledge of quantum Hall systems with us and making every effort to carve us into good researchers. Whatever little bit I have learnt, I greatly owe it to him. In every way, he epitomizes the virtues of a mentor. He and his wife Barbara Eisenstein have been a family away from home to me.

This opportunity to do my doctoral research at Caltech would perhaps not come my way without my Master's research under the guidance of Prof. Ajay Sood at IISc. To me, he personifies patience, resolution, and perseverance. I spent most of my time working with Anindya Das and Biswanath Chakraborty and developed a love for condensed matter experiments. It was this research experience that opened the doors of Caltech for me.

When I first arrived for a summer in 2008, Alex Champagne took me under his wings and taught me GaAs fabrication, using the wire bonder, etc. I also greatly enjoyed my interaction with the entire Eisenstein group. When I returned to Caltech for my PhD in 2009, I greatly benefitted from working closely with very talented and motivated group members. I would especially like to thank Aaron Finck for teaching me the bilayer fabrication and measurements. The time we collaborated were one of the most invigorating times of my life. I also collaborated with Trupti Khairi on bilayer tunneling experiments, and the tunneling data presented in this thesis is result of this collaborative effort. She initiated the microwave studies on interlayer tunneling in bilayers that I pursued later.

The MBE grown wafers for the experiments presented in this thesis were grown by Loren Pfeiffer, and Ken West. This thesis would not be possible without this

amazing collaboration. My understanding of the bilayer quantum Hall effect has richly benefitted from discussions with Inti Sodemann, Jung-Jung Su, and Allan MacDonald.

I am very thankful to Erik Henriksen for teaching me fabrication of graphene devices when I had just arrived. I also greatly enjoyed discussions with Bill Chickerling about thermal transport of electrons. I had a great time working on the machine shop and am especially grateful to machinist Mark Gonzales for teaching me how to operate the seemingly daunting machines. I benefitted much from discussions with Johannes Pollanen about dilution refrigerators and their cryo-free versions. My technical side as a low temperature physicist improved greatly in his company. It was fortunate that my friend Chandni U joined our group as a postdoc and we have had a great time together. She helped me learn Labview Programming that I had a long-standing desire to learn. I want to acknowledge her help in improving this thesis through several careful readings and suggestions. Special thanks to Loly Ekmekjian for being so loving to all of us around her. She always took care of all our needs.

My efforts to couple microwave radiation to the bilayer tunnel junction benefitted immensely from discussions with Prof. Keith Schwab and his group members Harish Ravi, Ari Weinstein, Laura De Lorenzo, and Chan U. I also learnt a lot about RF technicalities from discussing with R. Vijay and Mike Lilly.

It has been fun to work with two brilliant undergrads, Suhas Kumar at IISc, and Nina Budadev at Caltech, and help them with their summer projects. Both of them took off with flying colors to pursue their doctoral studies at Stanford and Caltech, respectively.

It was fortunate for me that Prof HRK was spending his sabbatical at Caltech from IISc. He has been a deeply inspiring teacher and researcher to me. He helped me improve my thesis through careful proof reading.

Our theory colleagues are always great to be with and I had a fun time hanging around with Jason Alicea, Olexei Motrunich, Shankar Iyer, Roger Mong, Scott Geraedts, Kun Woo Kim, Paraj Titum, Justin Song, and Karthik Seetharam. I am humbled by the warmth I received from Prof. Nai Cheng Yeh. Also, my days

at Caltech would not be as much fun without a whole bunch of friends I made, notably Ramathasan Thevamaran, Daniel Chao, Mattias Rydenfelt, Prabha Mandayam, Mansi M. Kasliwal, Uday Khankhoje, Mayank Bakshi, Sriharsh Tendulkar, Swetha Veeraraghavan, Srivatsan, Ramya Korlakai Vinayak, and several others, and we share fond memories of hikes and leisure times. Rebecca Rought, my roommate after I arrived in Pasadena, became a very endearing friend and always loved my cooking and we share fond memories of our Taiwan trip. I would like to thank Tejas Deshpande for cheerfully organizing the IQIM seminars that I have greatly enjoyed.

Finally, here I met my husband Shu-Ping Lee, who has shared with me the joys of life at Caltech. My parents Dilip and Kabita Nandi, close family members Jyoti Kar and Shanti Dutta, and friends, in particular Shreyasi Dutta, Anupama Ghosh, Priti Hansia, Paramita Kar Chowdhury, Munmun Kazi, Atrayi Roy, and Tania Paul Chowdhury have remained a great source of strength as their love transcends academic achievements.

# Abstract

The bilayer quantum Hall state at filling factor  $\nu_T = 1$  [1], where the total electron density matches the degeneracy of the lowest Landau level, is a prominent example of Bose-Einstein Condensation of excitons. A macroscopically ordered state is realized where an electron in one layer is tightly bound to a “hole” in the other layer. If exciton transport were the only bulk transport mechanism, a current driven in one layer would spontaneously generate a current of equal magnitude and opposite sign in the other layer. The Corbino Coulomb drag measurements presented in this thesis demonstrate precisely this phenomenon. Excitonic superfluidity has been long sought in the  $\nu_T = 1$  state. The tunneling between the two electron gas layers exhibits a *dc* Josephson-like effect [2]. A simple model of an overdamped voltage biased Josephson junction [3] is in good agreement with the observed tunneling  $I - V$ . At small tunneling biases, it exhibits a tunneling “supercurrent”. The dissipation is carefully studied in this tunneling “supercurrent” and found to remain small but finite.

# Publications

The work described in this thesis has resulted in the following publications:

1. Chapter 4 is based on: Nandi, D., Khaire, T., Finck, A. D. K., Eisenstein, J. P., Pfeiffer, L. N., and West, K. W. *Phys. Rev. B* 88 (16), 165308 (2013).
2. Chapter 5 is based on: Nandi, D., Finck, A. D. K., Eisenstein, J. P., Pfeiffer, L. N., and West, K. W. *Nature* 488 (7412), 481-484 (2012).

# Contents

<b>Acknowledgements</b>	<b>iii</b>
<b>Abstract</b>	<b>vi</b>
<b>Publications</b>	<b>vii</b>
<b>Introduction</b>	<b>xxii</b>
<b>1 Materials and Methods</b>	<b>1</b>
1.1 GaAs/AlGaAs single and double quantum wells . . . . .	1
1.1.1 Band structure engineering . . . . .	1
1.1.2 Growth by molecular beam epitaxy . . . . .	2
1.2 Device fabrication . . . . .	5
1.3 Preliminary device characterization . . . . .	5
1.3.1 Mobility . . . . .	6
1.3.2 Gate characteristics . . . . .	6
1.4 Conclusion . . . . .	8
<b>2 Quantum Hall Effect</b>	<b>9</b>
2.1 Landau level . . . . .	9
2.2 Integer Quantum Hall Effect . . . . .	11
2.3 Fractional Quantum Hall Effect . . . . .	14
2.3.1 Laughlin wavefunctions . . . . .	15
2.3.2 Composite Fermions . . . . .	15
2.4 Conclusion . . . . .	16

<b>3</b>	<b>Quantum Hall Exotica at <math>\nu_T = 1</math></b>	<b>18</b>
3.1	Quantum Hall effect at $\nu_T = 1$ . . . . .	19
3.1.1	111 state . . . . .	19
3.1.2	Pseudospin Ferromagnetism . . . . .	20
3.1.3	Exciton condensation . . . . .	21
3.2	Transport anomalies . . . . .	22
3.2.1	Phase transition at $\nu_T = 1$ . . . . .	22
3.2.2	Resonantly enhanced tunneling . . . . .	24
3.2.3	Goldstone mode . . . . .	25
3.2.4	Vanishing Hall resistance in counterflow . . . . .	26
3.3	Conclusion . . . . .	27
<b>4</b>	<b>Interlayer tunneling at <math>\nu_T = 1</math></b>	<b>29</b>
4.1	Corbino Device . . . . .	30
4.2	Interlayer tunneling at zero magnetic field . . . . .	31
4.3	Interlayer tunneling at $\nu_T = 1/2 + 1/2$ . . . . .	33
4.4	Interlayer coherent tunneling at $\nu_T = 1$ . . . . .	34
4.5	Josephson effect at $\nu_T = 1$ . . . . .	34
4.5.1	Two terminal tunneling . . . . .	35
4.5.2	Four terminal tunneling . . . . .	36
4.5.3	Temperature dependence of tunneling . . . . .	39
4.5.4	Resistance of “supercurrent” branch . . . . .	40
4.5.5	Effect of external resistors . . . . .	42
4.5.6	Overdamped Josephson junction . . . . .	46
4.5.7	Effective layer separation dependence of tunneling . . . . .	48
4.5.8	Contact independence . . . . .	50
4.5.9	Multiple source drain pairs . . . . .	51
4.6	Conclusion . . . . .	54
<b>5</b>	<b>Coulomb drag in Corbino geometry at <math>\nu_T = 1</math></b>	<b>55</b>
5.1	Zero magnetic field Coulomb drag . . . . .	55

5.2	Coulomb drag at $\nu_T = 1/2 + 1/2$ . . . . .	57
5.3	Coulomb drag at $\nu_T = 1$ in Hall bar geometry . . . . .	58
5.4	Voltage drag in Corbino geometry . . . . .	59
5.5	Corbino Counterflow at $\nu_T = 1$ . . . . .	60
5.6	Su-MacDonald Theory . . . . .	62
5.7	Corbino Coulomb drag at $\nu_T = 1$ . . . . .	63
5.7.1	Magnetic field dependence of Coulomb drag . . . . .	64
5.7.2	“Perfect” Coulomb drag at $\nu_T = 1$ . . . . .	65
5.7.3	Breakdown of “perfect” Coulomb drag . . . . .	66
5.7.4	Temperature and effective layer dependence of Coulomb drag . . . . .	67
5.8	Modeling Coulomb drag at $\nu_T = 1$ . . . . .	68
5.8.1	Voltage drag . . . . .	69
5.8.2	Measurement of arm resistances . . . . .	70
5.8.3	Measurement of $\sigma_{xx}$ . . . . .	71
5.9	Comparison of model vs experiment . . . . .	72
5.10	Conclusion . . . . .	73
<b>6</b>	<b>Effects of microwaves on interlayer tunneling at <math>\nu_T = 1</math></b> . . . . .	<b>74</b>
6.1	Photon Assisted Tunneling . . . . .	74
6.2	AC Josephson effect . . . . .	76
6.3	Theory of effects of microwaves on quantum Hall bilayers at $\nu_T = 1$ . . . . .	78
6.4	Experimental implementation . . . . .	80
6.4.1	Frequency range selection . . . . .	80
6.4.2	Sample design . . . . .	81
6.4.3	Cryostat modification . . . . .	86
6.4.4	Power dependence . . . . .	88
6.4.5	Frequency dependence . . . . .	90
6.4.6	Two terminal vs. four terminal . . . . .	91
6.4.7	Density dependence . . . . .	92
6.4.8	Area dependence . . . . .	94

6.5 Conclusion and future direction . . . . .	96
<b>Conclusion</b>	<b>98</b>
<b>A List of samples</b>	<b>104</b>
<b>B Fabrication of photon assisted tunneling device</b>	<b>106</b>
<b>C Fabrication and measuring insertion loss of coplanar waveguide</b>	<b>114</b>
<b>Bibliography</b>	<b>118</b>

# List of Figures

1.1	(a) Schematic of a GaAs/Al <sub>0.32</sub> Ga <sub>0.68</sub> As single quantum well [4]. (b) Schematic of a GaAs/Al <sub>0.90</sub> Ga <sub>0.10</sub> As/GaAs double quantum wells. . . . .	2
1.2	Schematic of a typical GaAs/Al <sub>x</sub> Ga <sub>1-x</sub> As bilayer wafer grown by MBE.	4
1.3	(a) Two terminal conductance vs arm top gate voltage at $T = 4.2$ K. (b) Two terminal conductance vs arm back gate voltage at $T = 4.2$ K [5].	8
2.1	(a) Energy vs. density of states of a two-dimensional electron gas, (b) Landau Level states upon application of magnetic field, and (c) Disorder broadened Landau levels. . . . .	10
2.2	A typical quantum Hall measurement configuration . . . . .	12
2.3	A plot of $R_{xx}$ and $R_{xy}$ in a single quantum well. Data is from Finck et al. [6] . . . . .	12
2.4	The Landau levels plotted against the sample width $x$ . . . . .	13
2.5	A plot of longitudinal and transverse Hall resistance in a ultra high mobility single quantum well [7]. . . . .	14
3.1	A plot of longitudinal and transverse Hall resistance in a high mobility bilayer quantum well after Eisenstein et al. [1] . . . . .	19
3.2	The resistivity $\rho_{xx}$ exhibits a QHE at $\nu_T = 1$ for total electron density = $1.26 \times 10^{11}$ and no QHE for total electron density = $1.45 \times 10^{11}$ . Inset: Map of the phase diagram of the $\nu_T = 1$ state as a function of tunneling strength. This data is due to Murphy et al. [8]. . . . .	23

3.3	The quantum Hall gap $\Delta$ vs. tilt angle $\theta$ in a weakly tunneling sample. The black dots are for $\nu_T = 1$ state. The triangles are for $\nu_T = 2/3$ state. This data is due to Murphy et al. [8]. . . . .	23
3.4	Tunneling conductance $dI/dV$ vs interlayer voltage $V$ . The total electron density is $N_T \times 10^{10} \text{cm}^{-2}$ . Results are due to Spielman et. al. [2] . . . . .	24
3.5	Evolution of tunneling conductance spectra with application of in-plane magnetic field. $B_{\parallel} = 0, 0.11, 0.24, 0.29, 0.35, 0.43, 0.49,$ and $0.59$ T. Results are from Spielman et al. [9]. . . . .	26
3.6	The solid and dotted traces represent the $R_{xy}$ and $R_{xx}$ in a bilayer, respectively. The temperature $T = 50$ mK and $d/l = 1.58$ . (a) Currents are in parallel. (b) Currents are anti-parallel in the two layers. Results are reproduced from Kellogg et al. [10] . . . . .	27
4.1	The front view of the Corbino device on which the tunneling measurements were performed. On the bottom side main back gates and back arm gates are lithographically patterned as well. Reproduced from Finck's Ph.D. thesis [6]. . . . .	31
4.2	Plot of $dI/dV_{dc}$ vs. $V_{dc}$ , $B = 0$ T and $T \approx 15$ mK [11]. . . . .	32
4.3	Plot of $dI/dV$ vs $V$ at $T \approx 15$ mK, total electron density $n_T = 0.85 \times 10^{11} \text{cm}^{-2}$ and $B = 3.6$ T. First studies were by Eisenstein et al. [12] . . . . .	33
4.4	Plot of $I$ vs $V_{dc}$ on outer rim at $T = 15$ mK, $d/l = 1.5$ . . . . .	36
4.5	Plot of $I$ vs $V$ on outer rim at $T = 15$ mK, $d/l = 1.5$ . . . . .	36
4.6	Plot of the load lines for resistance $R_L = 90$ KOhms and $V_{dc} = 120 \mu\text{V}, 140 \mu\text{V}, 160 \mu\text{V}$ for the blue, brown, and green lines. This is plotted against the intrinsic tunneling $I - V$ curve. . . . .	37
4.7	Plot of $V$ vs $V_{dc}$ on outer rim at $T = 15$ mK, $d/l = 1.5$ . . . . .	38
4.8	Plot of $V_{inner}$ vs. $V_{outer}$ on outer rim at $T = 15$ mK, $d/l = 1.5$ . . . . .	38

4.9	Temperature dependence of a voltage biased Josephson Junction. $T = 34, 98, 245, 400, 622$ mK, respectively, from top to bottom. This data is from Steinbach et al. [13]. . . . .	39
4.10	Temperature dependence of tunneling $I - V$ , $d/l = 1.5$ . . . . .	40
4.11	Plot of resistance $R_s$ vs inverse temperature at $d/l = 1.5$ for three different source drain configurations. . . . .	41
4.12	Plot of $I$ vs $V_{dc}$ on outer rim with different external resistors $R_{ext}$ on each arm at $T = 15$ mK, $d/l = 1.5$ . . . . .	42
4.13	Plot of $I$ vs $V$ on outer rim with different external resistors $R_{ext}$ on each arm at $T = 15$ mK, $d/l = 1.5$ . . . . .	42
4.14	(a) $RSJ$ Model for a current biased Josephson junction and (b) Circuit Model for a voltage biased Josephson junction. . . . .	43
4.15	Circuit model for a voltage biased Josephson junction with a resistor $R_{\parallel}$ in parallel to the Josephson junction. . . . .	44
4.16	The red trace is experimental tunneling $I - V$ in Fig. 4.5 and the blue curve is from model of a voltage biased Josephson junction shown in Fig. 4.15 with $R = 70$ KOhms and $R_{\parallel}(\text{fit parameter}) = 700$ KOhms. . . . .	45
4.17	Equivalent circuit model for bilayer tunneling . . . . .	47
4.18	Plot of $I_c$ vs $T$ at different $d/l$ . . . . .	48
4.19	Plot of $I_c/I_{c,max}$ vs $T$ at different $d/l$ . . . . .	49
4.20	Plot of $I_{c,max}$ vs $d/l$ . . . . .	49
4.21	Plot of $I_c$ vs $T$ at different source drain configuration for $d/l = 1.5$ . . . . .	51
4.22	Measurement setup. The voltages $V_1$ is held fixed. Voltage $V_2$ is swept. $I_1$ and $I_2$ are measured. . . . .	51
4.23	Tunneling currents $I_2$ vs $I_1$ obtained by varying $V_2$ and holding $V_1$ fixed at $-300 \mu\text{V}$ , $0 \mu\text{V}$ , $300 \mu\text{V}$ for the blue, red, and green traces, respectively. . . . .	52
4.24	Critical current values of $I_2$ plotted vs fixed values of $I_1$ . . . . .	52

5.1	Temperature dependence of drag resistivity $R_D$ vs $T$ . Temperature dependence is also plotted for the electron-electron scattering lifetime. Inset: A double quantum well structure for which the drag measurements were performed. Reproduced from Gramila et al. [14] . . . . .	56
5.2	Temperature dependence of drag at $\nu_T = 1/2 + 1/2$ for $I = 7.5$ nA and $I = 1.5$ nA. Figure is adopted from Lilly et al. [15]. . . . .	58
5.3	Evolution of Hall drag for $d/l = 1.60, 1.66, 1.72, 1.76,$ and $1.83$ , respectively. $R_{xy}^*$ and $R_{xy,D}$ are the Hall resistance of the current carrying layer and the drag layer, respectively. Results are due to Kellogg et al. [16]. . . . .	59
5.4	(a) Corbino device geometry (b) Plot of Corbino conductance at zero bias voltage with B-field sweep at $d/l = 1.5$ for source and drain voltages on opposite rims. Sample is tilted to magnetic field direction by 28 degrees. Data is due to Finck et al. [17]. . . . .	60
5.5	Red trace is counterflow $I - V$ in a Corbino device at $\nu_T = 1$ at $T = 25$ mK, $B_{\perp} = 1.88$ T, and $\theta = 28$ degrees. Blue trace is tunneling $I - V$ . Contacts 5 and 6 are on the inner rim and 2 is on the outer rim of the Corbino device. Reproduced from Finck et al. [17]. . . . .	61
5.6	Tunneling $I - V$ is measured for $d/l = 1.5$ and $T = 20$ mK. The purple trace is $\theta = 0$ degrees and the brown trace is $\theta = 26$ degrees. . . . .	61
5.7	$I_s$ is the blue trace and is the current flowing through the shunt resistor. $I_1$ is the current flowing through the bottom layer and marked in red. $I_2$ is the current flowing through the short. Data is taken at $B_{\perp} = 1.88$ T, and $\theta = 28$ degrees. This data demonstrates bulk exciton flow. Reproduced from Finck et al. [17]. . . . .	62

5.8	Schematic depiction of series counterflow and drag counterflow. According to Su-Macdonald theory, only drag counterflow sustains exciton superflow. $TL$ and $BL$ refer to the top and bottom contacts, respectively, of the condensate on one rim whereas $TR$ and $BR$ refer to the top and bottom contacts, respectively, of the condensate on the other rim of a Corbino device. Reproduced with permission from Su et al. [18].	63
5.9	Circuit for Coulomb drag measurement for a quantum Hall bilayer. . .	64
5.10	Temperature dependence of Coulomb drag conductance $\frac{dI_2}{dV_B}$ with magnetic field sweep. Tilt angle $\theta = 26$ degrees, and $d/l = 1.5$ . . . . .	65
5.11	The red and blue traces show the measured drive and drag currents, respectively. $T = 25$ mK, $d/l = 1.5$ , and $\theta = 26$ degrees. . . . .	65
5.12	The red and blue traces show the measured drive and drag currents, respectively. $T = 25$ mK, and $\theta = 26$ degrees. . . . .	66
5.13	(a) Temperature dependence of drag current to drive current ratio for $d/l = 1.5$ , and $\theta = 26$ degrees.(b) Effective layer separation $d/l$ dependence of drag current to drive current ratio for $T = 17$ mK, and $\theta = 26$ degrees. . . . .	67
5.14	A 1D-model in the current drag configuration. . . . .	68
5.15	A 1D-model in the voltage drag configuration. . . . .	70
5.16	The green trace is the two terminal tunneling whereas the black trace is the four-terminal tunneling at $T \approx 20$ mK, $d/l = 1.5$ , and $\theta = 0$ . . .	71
5.17	Plot of Corbino conductance vs applied bias voltage at $d/l = 1.5$ for source and drain voltages on opposite rims. Sample is tilted by $\theta = 26$ degrees. . . . .	71
5.18	The solid traces are Coulomb drag measurements for $d/l = 1.5$ and $T = 25$ mK. The red trace is drive current and the blue trace is drag current at $\theta = 26$ degrees. The black dashed curves are computed from the 1D model. . . . .	72

5.19	Comparison of experimental data to 1D-model for temperature dependence of drag current to drive current ratio for $d/l = 1.5$ and $\theta = 26$ degrees. The black dots are predictions from the 1D-model. . . . .	73
6.1	Voltage $V$ vs. tunneling current $I$ of a superconducting tunnel junction measured in the dark and in the presence of microwaves. Data is due to Dayem and Martin [19]. . . . .	75
6.2	Tunneling voltage vs current for a superconducting Josephson junction (a) in the absence of microwave photons and (b) in the presence of microwave photons. This effect was discovered by Sidney Shapiro. Data is from Johannes Kohlmann and Ralf Behr et al. [20] . . . . .	77
6.3	(a) Tunneling $I - V$ due to absorbed or emitted microwave photons at $eV_{dc} = \gamma\hbar\omega$ for different values of $\beta = eV_{dc}/\hbar\omega$ .(b) Dependence of the tunneling $I - V$ on the decoherence rate $\alpha$ . Reproduced from Hyart and Rosenow [21]. . . . .	79
6.4	The dashed curve is the calculated tunneling $I - V$ in the absence of microwaves and the solid trace is the modified $I - V$ in presence of microwaves of angular frequency $\omega$ . (a) $\hbar\omega = 0.1\mu_c$ and (b) $\hbar\omega = \mu_c$ . $I_c$ is the critical current and $\mu_c$ is the dc bias voltage at which the critical current $I_c$ is exhibited. Reproduced from Sodemann et al. [3]. . . . .	79
6.5	Plot of tunneling “supercurrent” branch showing that it has a finite resistance. The interlayer separation $d/l = 1.5$ and $T = 50$ mK . . . . .	81
6.6	(a) Schematic of $RF$ voltage applied $V_{RF}$ in addition to the dc applied bias $V_{dc}$ between the source drain contacts in a tunneling configuration. The current $I$ is measured. The blue dotted lines represent the bilayer two dimensional electron gas layers. (b) Top side image of a device made for $RF$ voltage applied across two of the ohmics. (c) Back side image of the same device. . . . .	82

- 6.7 (a) Schematic of  $RF$  voltage applied  $V_{RF}$  applied between the global top and bottom gates. The blue dotted lines represent the bilayer. Bias voltage  $V_{dc}$  is the voltage applied across the tunnel junction and  $I$  is the tunneling current. (b) Top view of device (A) to apply  $RF$  across the global top and bottom gates. (c) Backside view of device (A). . . . . 84
- 6.8 Image of a coplanar waveguide on pristine GaAs. The metal pattern is made of aluminium. The rectangle patterned in the middle is of polyimide. The  $RF$  is transmitted through the central conductor. The outer ground planes made of aluminium have a gap in the middle and aluminium patterned on top of the polyimide to make a capacitor geometry. . . . . 85
- 6.9 Image of the thinned bilayer sample after wire-up. The backgate is connected to the central conductor of the coplanar waveguide through which the  $RF$  voltage is applied. The topgate is connected to the ground planes of the coplanar waveguide also with indium soldered gold wires. The coplanar waveguide is connected to the  $RF$  connector at the sample mount with indium solder. . . . . 86
- 6.10 The measurement setup build in the dilution refrigerator for coupling the  $RF$  to the bilayer quantum Hall system is schematically represented. The device is represented as a parallel plate capacitor with top and back gates. The attenuators are represented as resistors. The attenuators are introduced for the purpose of reducing thermal Johnson noise. The five stages of the dilution refrigerator are represented as boxes. The temperatures go from room temperature 300 K to the mixing temperature 10 mK in stages.  $V_{TG}$  and  $V_{BG}$  are the gate voltages on the top and bottom gates, respectively.  $V_{\omega}$  is the  $RF$  voltage supplied by the signal generator. Adopted with modifications from Schuster's thesis [22] . . . 87

- 6.11 Image of the dilution refrigerator. The cryogenic attenuators, the coax cables and the bias tee are marked. The room temperature Johnson noise is attenuated as the signal travels through the coax cable. The 3 cryogenic attenuators of 20 db, 5 db, and 10 db are clamped to the 4.2 K plate, the 0.7 K still, and the 50 mK plates, respectively. . . . . 88
- 6.12 (a) Tunneling current  $I$  plotted vs. measured 4-terminal voltage  $V$  at  $T = 15$  mK ,  $d/l = 1.52$ , and  $\theta = 0$  degrees. The  $RF$  frequency is 5 GHz.  $P$  denotes the different RF powers outputted at the signal generator (b) Temperature dependence of tunneling  $I - V$  without  $RF$  power for  $d/l = 1.52$  and  $\theta = 0$  degrees. . . . . 89
- 6.13 Yellow trace is tunneling current  $I$  plotted vs. measured 4-terminal voltage  $V$  at  $T = 15$  mK,  $d/l = 1.52$ , and  $\theta = 0$  degrees. The  $RF$  frequency is 5 GHz and power is 5 dbm at the signal generator output. 90
- 6.14 The deduced temperature  $T^*$  is plotted vs  $RF$  power at the signal generator output  $P$ . First with the  $RF$  power OFF, the temperature dependence of the critical current is made. Then the magnitude of the critical current is used to deduce the temperature  $T^*$  for measurements at  $T \approx 15$  mK and different  $RF$  powers. This measurement is done at several fixed frequencies. . . . . 91
- 6.15 Two terminal  $I - V_{dc}$  is plotted. For the red trace, all four ohmics are connected to  $RF$  ground. For the purple trace, only two ohmics are connected to  $RF$  ground and the remaining arms are cutoff with depletion top gates . . . . . 92
- 6.16 (a) Evolution of four terminal tunneling  $I - V$  at  $\nu_T = 1$  with increase in  $RF$  power  $P$  outputted from the frequency generator at  $d/l = 1.73$ ,  $T = 15$  mK, and  $\theta = 0$  degrees. (b) Temperature dependence of the four terminal tunneling  $I - V$  at  $\nu_T = 1$  ,  $d/l = 1.73$ , and  $\theta = 0$  degrees with  $RF$  OFF. . . . . 93

- 6.17 The temperature  $T^*$  deduced from tunneling measurements is plotted against the  $RF$  power  $P$  at the signal generator output. The  $RF$  induced heating effect is studied for two different electron gas densities and thereby different effective layer separations, i.e.,  $d/l = 1.52$ , and  $d/l = 1.73$ . . . . . 94
- 6.18 (a) Topview of a replica of device (B). (b) Backside view of a replica of device (B). Device (B) is a bilayer tunnel junction with the area underneath the global top and backgate  $350 \mu\text{m} \times 350 \mu\text{m}$ . The white metallized regions in Fig. 6.18 (a) and Fig. 6.18 (b) represent aluminium top and back gates, respectively. The two-dimensional electron gas regions are defined by the mesa boundary. The nichrome interconnects are  $25 \mu\text{m}$  wide. Rectangular gold pads are deposited on the top and backside to indium solder the  $RF$  gold wires. The sample is thinned down to  $50 \mu\text{m}$ . One difference between the replica and the actual device is that the interconnects are of nichrome in the original device and gold in the device replica. A detailed description of the fabrication process is found in Appendix B. (c) Comparison of the  $RF$  induced heating effect between device (A) and device (B). Device (B) has  $\approx 10$  times smaller overlap area between the global top gate and the global back gate. . . . . 95
- 6.19 Top view of a eight-terminal Corbino device with four arms on the inner rim and four arms on the outer rim. The bilayer two-dimensional electron gas was removed by a solution etch from outside the mesa boundary. The Ni/AuGe ohmics were diffused in. The arm top gates and global top gates were made of evaporated aluminium. This device was fabricated as an initial step in this direction. . . . . 100

- 6.20 The barrier is marked by  $M$ . The electron density in each layer in this region is chosen such that each layer is in an incompressible fractional quantum Hall  $1/m$  state each but the two layers are independent of each other. The regions  $L$  and  $R$  are in the  $\nu_T = 1$  state. The tunneling current  $I$  flows antiparallel in the two layers. Reproduced from Wen and Zee [23]. . . . . 101
- 6.21 (a) Schematic diagram of a surface acoustic wave device. The bilayer two dimensional electron gas is confined to a square with evaporated ohmics marked in brown. The SAW transducers are marked in yellow and can be patterned by e-beam or photolithography. (b) Image of a bilayer SAW device courtesy of J Pollanen. . . . . 102

# Introduction

Bose-Einstein Condensation was first predicted in 1924-1925 by Satyendranath Bose and Albert Einstein [24, 25, 26]. For massive particles obeying Bose statistics, a peculiar effect happens at very low but finite temperature. In Einstein's words "A separation is effected; one part condenses, the rest remains a saturated ideal gas" [26]. By condensation, it is meant that the massive bosons all occupy the lowest energy quantum ground state. Phenomenon like superconductivity discovered in 1911 [27, 28] and superfluidity in Helium-4 discovered in 1937 [29] are deeply related to Bose-Einstein condensation. The BCS theory of superconductivity [30] in 1957 described electrons in the superconductors form Cooper pairs which are Bosons and hence can condense.

In the light of the BCS theory, it was predicted in 1962 that bound pairs of electrons and "holes" called excitons could also exhibit similar Bose-Einstein Condensation phenomenon [31]. But recombination of electron hole pairs in optically generated electron hole plasmas is a major bottleneck in realization of exciton condensation. It was realized in 1975 by Lozovik and Yudson [32, 33] that pairing between spatially separated electrons and holes would circumvent the problem of finite exciton lifetimes. It was realized by Lerner and Lozovik in 1981 that a strong magnetic field would help the formation of the electron hole bound pairs [34].

Meanwhile, the Integer [35] and Fractional Quantum Hall effect [36] were discovered in two-dimensional electron gas systems in strong perpendicular magnetic field. Aided by significant technological advances in molecular beam epitaxy, the study of the quantum Hall effect in double quantum well structures by Eisenstein et al. led to the discovery of the  $\nu_T = 1$  state.

The deep connection between the  $\nu_T = 1$  state and exciton condensation gained further experimental grounds with the discovery of a *dc* Josephson like phenomenon [2] due to Spielman et al. But finite tunneling conductance of the zero bias peak led to controversies as to why there was no true Josephson effect [37]. In this thesis, this tunneling phenomenon has been revisited in detail. The tunneling  $I - V$  is in good agreement with a simple model of an overdamped Josephson junction [3]. The dissipation in the tunneling “supercurrent” branch was found to have a roughly thermally activated behavior with the gap governed by the quantum Hall gap. The tunneling measurements demonstrate tunneling to be a bulk phenomenon.

Evidence of counterflow superfluidity in experiments of Kellogg et al. [16, 38, 10] provided further evidence of exciton condensation. However, these initial measurements were in Hall bar geometry and could not establish exciton transport as a bulk phenomenon. To address these questions, studies of the  $\nu_T = 1$  state were initiated in Corbino geometry by Teimann et al. [39, 40, 41, 42, 43]. A Corbino geometry is where the bilayer is etched in the shape of an annular disc with contacts to the inner and outer rim. Here transport properties through the bulk of the device can be explored unlike in Hall bars. Finck et al. demonstrated bulk transport of excitons in the Corbino geometry [17, 6] with tunneling between the layers suppressed by an in-plane magnetic field.

The experiments presented in this thesis demonstrate “perfect” Coulomb drag, where electron current driven in one layer spontaneously generates hole current in the other layer. This is evidence of bulk mode of transport of the exciton condensate in a Corbino device even in the absence of any electrical connections between the two layers. A simple 1D model of counterflow transport due to an excitonic superfluid and parallel transport due to charged excitations above the quantum Hall gap is found in good agreement with the experimental data.

## Thesis Layout

The initial chapters of this thesis give a brief overview introduction to the field. The subsequent chapters deal with specific experiments undertaken and new results. A brief description of the emphasis of each chapter is given here.

**Chapter 1** contains description of the molecular beam epitaxy process involved in the growth of GaAs/Al<sub>x</sub>Ga<sub>1-x</sub>As double quantum wells. The device fabrication process is explained briefly. Also, preliminary transport measurements like mobility determination, and magnetotransport are discussed. These steps help to identify the highest quality samples suitable for further studies.

**Chapter 2** gives a review of the Integer Quantum Hall Effect (IQHE) [35] and Fractional Quantum Hall Effect (FQHE) [36]. In the IQHE, precisely quantized plateaus in transverse Hall conductance in units of  $e^2/h$  are observed. This is understood in terms of ballistic edge channels with each channel contributing a conductance quanta of  $e^2/h$  within the Landau-Buttiker formalism [44, 45]. The dramatic discovery of quantized plateaus at  $1/3$  of  $e^2/h$  marked the discovery of the FQHE. A plethora of other odd denominator fractions were discovered. Laughlin's profound explanation of the FQHE at filling factor  $\nu = 1/3$  help understand several other odd denominator fractions. But there are other fractional states experimentally discovered that are not predicted by Laughlin's theory. The composite Fermion theory [46] of Jain gives a simple explanation for the odd denominator fractions unexplained by Laughlin's theory. Finally, the chapter concludes with the discovery of even denominator fractions [47, 48] that cannot be explained by Laughlin's wavefunctions or the composite Fermion theory.

**Chapter 3** gives an introduction into the physics of the bilayer quantum Hall state at filling factor  $\nu_T = 1$  [1]. It explains why the ground state wavefunction of this state is a Bose-Einstein condensate of excitons. Due to strong interlayer Coulomb interaction, an electron in one layer is strongly bound to a hole in the other layer. This leads to a spectacular phenomenon in tunneling that has resemblance to the *dc* Josephson effect [2] and is suggestive of excitonic superfluidity. Also, the

Hall resistance vanishes in counterflow [10], indicating counterflow currents carried by charge neutral excitons that do not experience Lorentz deflection. All the experiments discussed in this chapter are in simply connected Hall bar geometry.

Tunneling at  $\nu_T = 1$  state in a Corbino device is central to **Chapter 4**. Initially tunneling between two 2-dimensional electron gas systems in the absence of a magnetic field is described. This tunneling has a peak at zero bias [11] when the two layers have equal density because of conservation of energy and in-plane momentum. A strong perpendicular magnetic field is applied such that electron gas in each layer independently is at  $\nu = 1/2$  and has the lowest Landau level half filled, but interlayer coulomb interaction is negligible. The zero bias peak gets replaced by a strong suppression of tunneling at zero bias [12]. By lowering the electron density in each layer and thereby decreasing the effective layer separation, the bilayer  $\nu_T = 1$  state is established. This state is marked by a *dc* Josephson like tunneling anomaly discovered by Speilman et al. [2]. This tunneling phenomenon is studied in detail in this chapter [49]. The four terminal tunneling  $I - V$  is found to be rather independent of addition of external resistors and choice of source drain contacts both along the outer rim or both along the inner rim of the Corbino device. Thus an intrinsic tunneling  $I - V$  is established. The dissipation in the tunneling  $I - V$  close to zero bias is carefully measured and found to remain small but finite down to 30 mK. The four terminal tunneling  $I - V$  is found in good agreement with a simple model of voltage biased overdamped Josephson junction [3]. It is discussed as to why the junction is in the overdamped regime.

In **Chapter 5**, a current drag geometry is explored where a current is driven by an applied bias across the bulk of a Corbino device and the other layer is a closed loop. The two layers are electrically isolated. The drive and drag currents are measured. At the  $\nu_T = 1$  state, the ratio of drag to drive currents becomes close to unity and they are oppositely directed at the lowest  $T$  and  $d/l$ . This signifies most of the current being driven by electron hole bound pairs. At higher  $T$  and  $d/l$ , the drag current becomes lower than the drive current in magnitude. This can be captured in terms of a two fluid model of bulk counterflow transport due to excitons and parallel transport

due to charged quasiparticles thermally activated over the quantum Hall gap of the  $\nu_T = 1$  state.

The observation of a *dc* Josephson like phenomenon by Spielman et al. in tunneling at  $\nu_T = 1$  motivated the search for an *ac* Josephson like effect. **Chapter 6** starts with a discussion of photon assisted tunneling and Shapiro steps in a superconducting tunnel junction. Then two recent theory papers by Hyart and Rosenow [21] and Sodemann et al. [3] on microwave induced effects on tunneling at  $\nu_T = 1$  is described. Experimental realization of this idea required the marriage of quantum Hall phenomenon with microwave technology and extensive build-up. The *RF* voltage was designed to be applied across the global top and back gates. This had the advantage of applying a uniform *RF* voltage on the  $\nu_T = 1$  region. However, it also had a disadvantage that the bilayer was only 28 nm apart and embedded between the global top and back gates that were 50  $\mu\text{m}$  apart. A bilayer sample any thinner cannot be freely handled in the existing fabrication technique. This required applying  $1800^2$  times more *RF* power between the top and back gates. The experimental observation of coupling the tunnel junction to microwave was that of heating. Several future ways to circumvent the thermal effects are discussed. This experiment immensely enhanced the knowledge of cryogenic design and *RF* engineering and laid a foundation for further efforts in this direction.

The thesis ends on a discussion of several future directions.

# Chapter 1

## Materials and Methods

### 1.1 GaAs/AlGaAs single and double quantum wells

Confining electrons to two dimensions and applying a perpendicular magnetic field has given rise to a plethora of very intriguing physics, for example, the integer quantum Hall effect and the fractional quantum Hall effect. The GaAs/Al<sub>x</sub>Ga<sub>1-x</sub>As quantum wells were amongst the cleanest systems where glimpse of these phenomena were observed. This chapter discusses the growth of the GaAs double quantum well heterostructures by molecular beam epitaxy, the device fabrication, and preliminary characterization techniques.

#### 1.1.1 Band structure engineering

GaAs is a III-V direct band-gap semiconductor with a band gap of 1.42 eV at room temperature. It has a zinc blende crystal structure. It turns out that GaAs and AlAs have almost identical lattice constants. AlAs has an indirect band-gap of 2.12 eV. The bandgap  $E_g$  of Al<sub>x</sub>Ga<sub>1-x</sub>As can be tuned continuously between the two pristine band gaps.

Due to the confinement of the GaAs electrons in the  $z$ -direction as shown in Fig. 1.1 (a), the electrons are free to move in the  $x$  and  $y$  directions and have free electron wave-functions but have discrete quantized eigen-energies in  $z$  direction.

In the double quantum well structure explored in this thesis and shown in Fig.1.1

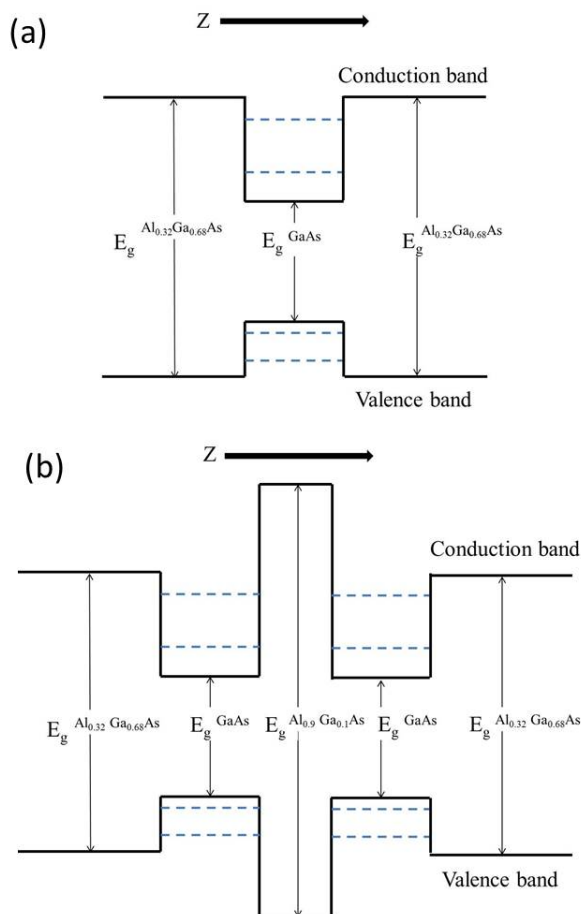


Figure 1.1: (a) Schematic of a GaAs/Al<sub>0.32</sub>Ga<sub>0.68</sub>As single quantum well [4]. (b) Schematic of a GaAs/Al<sub>0.90</sub>Ga<sub>0.10</sub>As/GaAs double quantum wells.

(b), two 18 nm GaAs quantum wells are separated by a barrier of 9.9 nm Al<sub>0.90</sub>Ga<sub>0.10</sub>As. Only the lowest subband is populated. For the studies relevant to this thesis, the bare tunnel coupling of the two quantum wells are very weak when measured at zero magnetic field.

### 1.1.2 Growth by molecular beam epitaxy

Molecular beam epitaxy (MBE) is a thermal evaporation technique [50, 51]. It has been extensively used in the growth of III-V compounds like gallium arsenide-aluminium gallium arsenide (GaAs/Al<sub>*x*</sub>Ga<sub>1-*x*</sub>As) heterostructures.

Deposition under ultra high vacuum (UHV) is a major consideration for growth

of high mobility two-dimensional electron gas (2DEG) systems. This is necessary so that the mean free path of the evaporated atoms is much larger than the distance between the source and the substrate [52]. The current state of the art MBE machines have closed-cycle helium cryopumps that maintain the main growth chamber pressure at  $10^{-12}$  torr [51]. The source materials of Ga, Al, and As are heated to a molten state to evaporate the elements. Shutters in front of the effusion cells allow controlled deposition of desired materials down to a single atomic layer. The GaAs substrate is also maintained at an elevated temperature. This provides sufficient energy for the deposited atoms to migrate to the proper crystal sites [52]. The effused Ga/Al atoms adsorb onto the substrate. But effused As atoms do not stick to the heated GaAs substrate unless another Ga/Al atom is present for bonding. As a result, precisely one As atom adheres to the surface for every Ga/Al atom. So the trick is to keep the As flux greater than the Ga/Al flux [52]. The substrates are also rotated to ensure a uniform deposition across the wafer [51]. The dopants are silicon (Si) and carbon (C) for n- and p- type doping. These filament sources are also loaded into the evaporation chamber. For *insitu* sample characterization, reflection high energy electron diffraction (RHEED) is used. The diffraction pattern of the reflected electron beam allows to study the crystalline structure of the growing sample surface.

Mobility of the 2DEG is a measure of its quality and is affected by various factors like impurities present in the source material and scattering due to the ionized dopant atoms, etc. In the bilayer quantum wells used in this thesis modulated doping is employed, where the dopant layer is embedded in the  $\text{Al}_x\text{Ga}_{1-x}\text{As}$  layer but not in the GaAs quantum well. This spatial distance of the scattering centers from the quantum well helps to significantly improve mobility [53, 52].

A typical double quantum well sample, as is used in this thesis, is grown on a GaAs substrate. Initially a layer GaAs is grown by MBE on top of the substrate to improve the crystalline order. Then a thick layer of  $\text{Al}_{0.32}\text{Ga}_{0.68}\text{As}$  is grown where the Si dopant layer is situated. After that 180 Å of GaAs quantum well is grown, followed by 99 Å of  $\text{Al}_{0.90}\text{Ga}_{0.10}\text{As}$  and another 180 Å of GaAs quantum well. A high concentration of Al is used to create a tall and thin tunnel barrier. However, it cannot be 100%

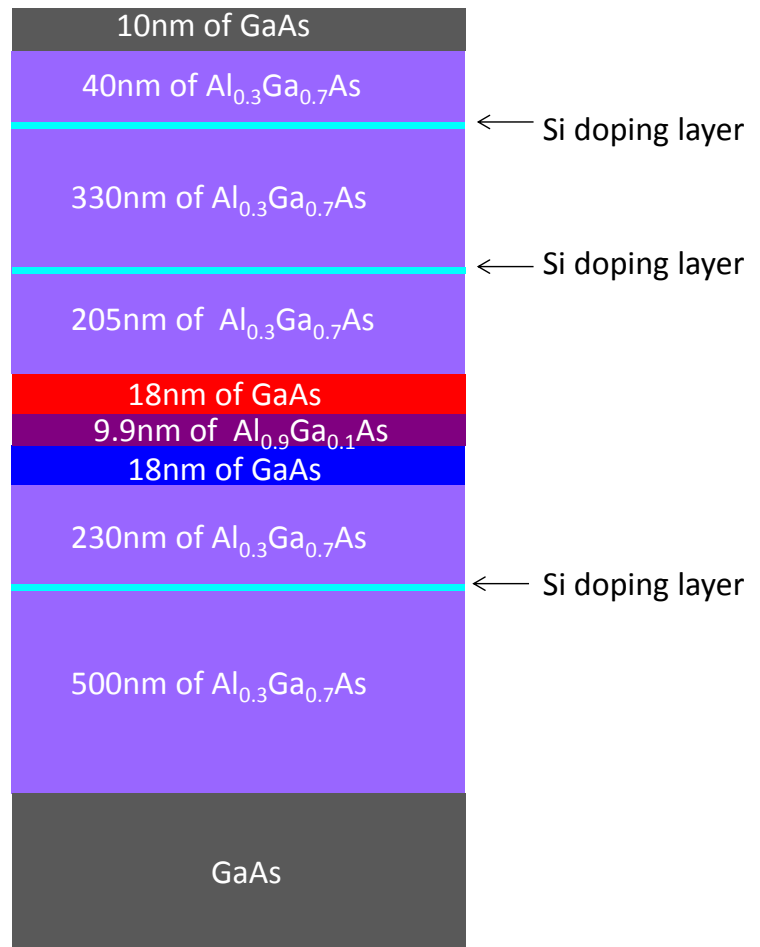


Figure 1.2: Schematic of a typical GaAs/ $\text{Al}_x\text{Ga}_{1-x}\text{As}$  bilayer wafer grown by MBE.

Al as aluminium oxidizes and becomes an insulator. This prevents the ohmics from contacting the bottom 2DEG. It was found through several optimization efforts that 10% of Ga in the tunnel barrier helps to prevent this oxidation. The Si dopants are again embedded in a thick layer of  $\text{Al}_{0.32}\text{Ga}_{0.68}\text{As}$ . Finally the sample is capped off by 100 Å of GaAs as the Al in the  $\text{Al}_{0.32}\text{Ga}_{0.68}\text{As}$  is too reactive and cannot remain exposed to air.

After the wafer is grown by MBE, preliminary characterizations have to be performed to determine its suitability for future experiments.

## 1.2 Device fabrication

Processing of the bilayer samples begin with cleaving a  $5 \text{ mm} \times 5 \text{ mm}$  sample. First a pattern is defined by etching away the GaAs from everywhere except the mesa pattern, which is protected by photoresist. The resist is then dissolved and the ohmics are lithographically placed along the mesa boundary. Then Ni/AuGe contacts are evaporated. As the last step of the topside fabrication, aluminium top gates are patterned on the topside of the sample also by photolithography.

It is then time for thinning down the sample and patterning backside gates. The sample is waxed down onto a quartz disc and thinned down by lapping against a clean room wipe wetted with bromine methanol solution. After the sample is thinned down to  $\approx (50 \pm 5) \mu\text{m}$ , the backside nichrome interconnects are patterned if required. This is followed by UV exposing the back gates pattern. The backside photolithography is helped by having an infrared camera attached to the microscope. GaAs is transparent to infrared radiation and the top side pattern can be viewed through it for alignment of the backside patterns. The aluminium backgates are then evaporated followed by dissolving the wax to detach the thinned sample from the quartz disc.

It can be wired up by attaching gold wires with indium blobs onto the Ni/AuGe bonding pads. The soldering is done under an optical microscope. Finally, the sample is made parallel to the sample mount. This is done by shining a laser onto the sample mount and marking the reflected laser spot. Then the sample is reoriented by the gold wires to match almost exactly the laser spot reflected off of the sample with the previous spot. This should allow for the device to be mounted perfectly horizontally.

A detailed procedure for device fabrication can be found in Appendix B.

## 1.3 Preliminary device characterization

After device fabrication, the suitability of the bilayer device for further studies is determined by preliminary characterization.

### 1.3.1 Mobility

The electron mobility  $\mu_e$  of the two dimensional electron gas (2DEG) at zero magnetic field and 300 mK is indicative of the quality of transport of the two dimensional electron GaAs at ultra low temperatures. The mobility is

$$\mu_e = \frac{e}{m^*}\tau, \quad (1.1)$$

where  $m^*$  is the effective mass of the electron and  $\tau$  is the scattering time of the electron. Hence a higher mobility sample would have longer electron mean free paths, implying the presence of fewer scatterers in the conduction channel. Hence the first step in the characterization process is to measure the device mobility.

$$\sigma_e = \frac{1}{\rho_e} = ne\mu_e, \quad (1.2)$$

$$\mu_e = \frac{1}{ne\rho_e}, \quad (1.3)$$

where  $\sigma_e$  is the conductivity,  $\rho_e$  is the resistivity and  $n$  is the electron density of the 2DEG.  $\rho_e$  is estimated using Van der Pauw's formula [54]. The electron density  $n$  is measured from the Hall resistance  $R_H$  where

$$R_H = \frac{B}{ne}. \quad (1.4)$$

For the bilayer samples, electron mobility is measured separately for the top and bottom layers. The typical as grown mobilities for our bilayer samples are  $1 \times 10^6$  cm<sup>2</sup>/Vs.

### 1.3.2 Gate characteristics

For the bilayer devices, the annealed ohmics end up diffusing into the GaAs and making contact to both the top and bottom layers in parallel. Unless each layer could be independently contacted [5], various transport studies done on quantum

Hall bilayers at  $\nu_T = 1$  like tunneling [2, 9], Hall drag [16], Coulomb drag [38], etc., were not possible. To circumvent this problem, the central region of the device extend into arms. The ohmic is placed on these protruding arms. On the top and back side of each arm are placed depletion gates, which are basically evaporated aluminium electrodes. The top gate is  $\approx 600$  nm away and the bottom gate is  $50 \mu\text{m}$  away from the 2DEGs.

The gates are basically parallel plate capacitors where one plate is the top/back gate. The other plate of the capacitor is the 2DEG. When a negative voltage is applied on the top gate, it pulls in holes in the 2DEG through the ohmic contacts. This changes the density in the 2DEG by

$$\delta n_{tg} = C_{tg} V_{tg}, \quad (1.5)$$

where  $V_{tg}$  is the voltage applied on the top gate electrode and  $C_{tg}$  is the capacitance per unit area of the top gate given by

$$C_{tg} = \frac{\epsilon_r \epsilon_0}{d_{tg}}, \quad (1.6)$$

where  $d_{tg}$  is the distance between the top gate and the upper quantum well and  $\epsilon_r = 13$ .

When  $\delta n_{tg}$  matches the as grown electron density of the top quantum well, it depletes that quantum well completely. Further applying a negative gate voltage begins to deplete the bottom quantum well also. In a two-terminal conductance measurement through both layers in parallel, this process appears as a two-step gate depletion characteristics. The reason for two clear steps is that the upper 2DEG effectively screens out the electric fields due to the top gate until it is close to depletion.

A typical top gate characteristic is shown in Fig. 1.3 (a). In the bilayer devices, the cut-off voltage for the top layer is  $\approx -0.5$  V and for both layers is  $\approx -1$  V.

The discussion applies almost identically to the bottom gates as well. A typical back gate characteristics is shown in Fig. 1.3 (b). The bottom gates are  $\approx 80$

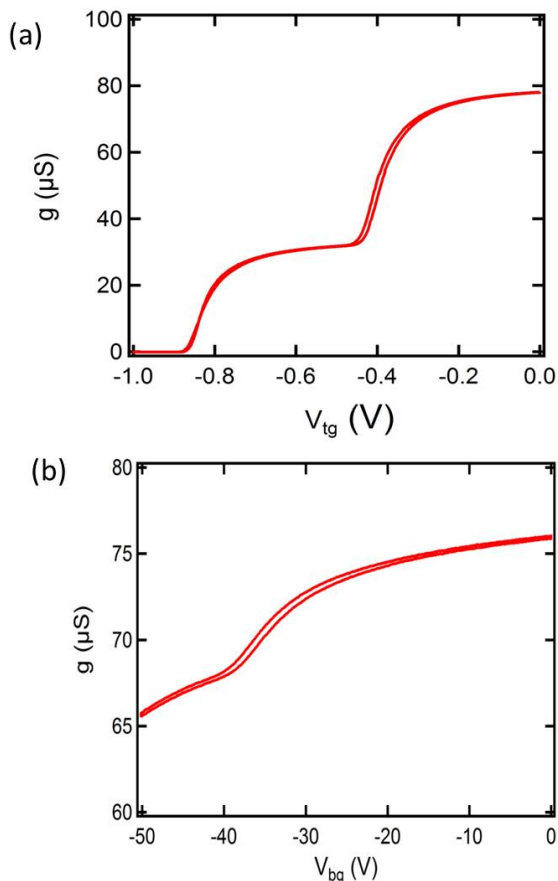


Figure 1.3: (a) Two terminal conductance vs arm top gate voltage at  $T = 4.2$  K. (b) Two terminal conductance vs arm back gate voltage at  $T = 4.2$  K [5].

times away from the 2DEG compared to the top gates and hence require much larger negative voltages to be applied. So it is not advisable to ramp up the back gate voltage much beyond the depletion of the bottom layer.

## 1.4 Conclusion

In conclusion, novel growth techniques like molecular beam epitaxy allow access to extremely clean single and double quantum well samples that can be fabricated using photo-lithography techniques. Simple device characterization allow for determining the transport quality of the sample. Once the highest quality sample are selected, phenomena related to bilayer quantum Hall effect can be investigated.

## Chapter 2

# Quantum Hall Effect

### 2.1 Landau level

First, the simplest case of an electron moving in a two-dimensional plane with a perpendicular magnetic field applied on it is considered. The Hamiltonian  $H$  is given by

$$H = \frac{1}{2m_e}(\vec{p} + q\vec{A})^2. \quad (2.1)$$

This problem can be reduced to the problem of a simple harmonic oscillator with eigen-energies [55]

$$E_n = \hbar\omega_c(j + \frac{1}{2}), \quad (2.2)$$

where  $j = 0, 1, 2, 3..$  corresponding to different Landau Levels and  $\hbar\omega_c$  is the cyclotron energy. The degeneracy  $D$  per unit area of each Landau level is given by

$$D = \rho^{DEG}\hbar\omega_c. \quad (2.3)$$

$\rho^{2DEG}$  is the density of states (DOS) of a two-dimensional electron gas is a constant [56].

$$\rho^{DEG} = \frac{m^*}{2\pi\hbar^2}. \quad (2.4)$$

Substituting,

$$D = \frac{m^*\hbar\omega_c}{2\pi\hbar^2}, \quad (2.5)$$

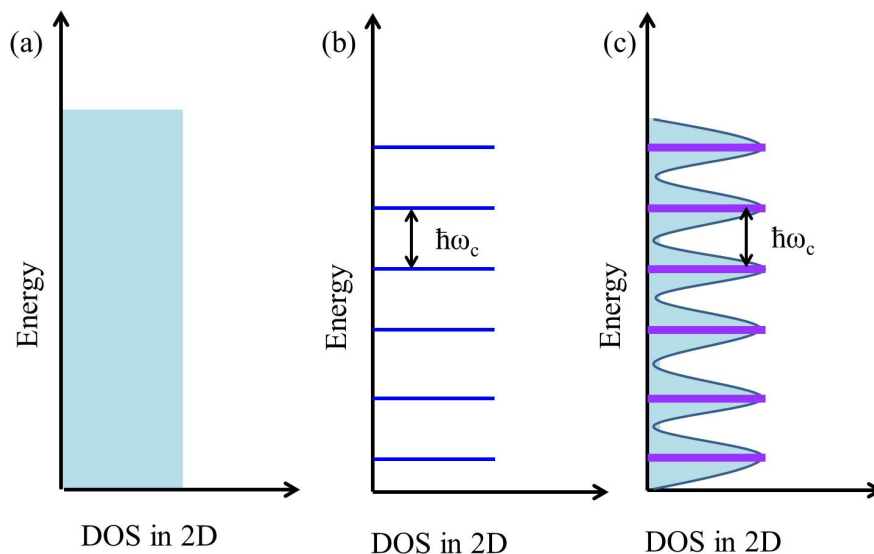


Figure 2.1: (a) Energy vs. density of states of a two-dimensional electron gas, (b) Landau Level states upon application of magnetic field, and (c) Disorder broadened Landau levels.

$$D = \frac{eB}{h}. \quad (2.6)$$

Interestingly, the Landau level degeneracy per unit area  $D$  is independent of Landau level index  $j$  and depends on fundamental constants  $e$  and  $h$  alone, other than the magnetic field. The Landau level degeneracy  $D$  does not depend on the exact details of the parabolic energy dispersion.

The density of states in two dimensions in the absence of a magnetic field is a constant as shown in Fig. 2.1 (a). When a perpendicular magnetic field is applied, discrete quantum states called Landau levels are formed which are equally spaced and the energy spacing is the cyclotron energy  $\hbar\omega_c$  as shown in Fig. 2.1 (b). The Landau levels are broadened by disorder in any realistic sample and is represented in Fig. 2.1 (c).

The un-normalized wavefunctions for the lowest  $j = 0$  Landau level in the symmetric gauge are [55]

$$\phi_{j=0,m}(z) = z^m e^{-\frac{|z|^2}{4}}. \quad (2.7)$$

Here  $z$  is  $x + iy$  where  $x, y$  are the physical coordinates of the electron. For a lowest

completely filled Landau level when the number of electrons  $N$  matches the Landau level degeneracy [55], the groundstate wavefunction  $\phi(z_1, z_2, \dots, z_N)$  is given by the Slater determinant for  $N$ -noninteracting electrons.

$$\phi(z_1, z_2, \dots, z_N) = \begin{vmatrix} 1 & 1 & 1 & \dots & 1 \\ z_1 & z_2 & z_3 & \dots & z_N \\ z_1^2 & z_2^2 & z_3^2 & \dots & z_N^2 \\ \dots & \dots & \dots & \dots & \dots \\ z_1^N & z_2^N & z_3^N & \dots & z_N^N \end{vmatrix} \quad (2.8)$$

$$\phi(z_1, z_2, \dots, z_N) = \prod_{j < k} (z_j - z_k) e^{-\frac{1}{4} \sum_i |z_i|^2}. \quad (2.9)$$

Here  $z_i$ 's denote coordinate of the electrons. Hence when the lowest Landau level is completely occupied, the electrons can avoid each other very effectively. The macroscopic wavefunction vanishes if two electrons coincide with each other in position. This will have profound implications for the bilayer  $\nu_T = 1$  quantum Hall state as will be elaborated on in Chapter 3.

## 2.2 Integer Quantum Hall Effect

The Hall effect is measured conventionally in a Hall bar geometry. A current  $I$  is passed through the center of the Hall bar in the direction  $x$ . The longitudinal and transverse Hall voltages  $V_{xx}$  and  $V_{xy}$  are measured. A schematic diagram for a Hall measurement is shown in Fig. 2.2. As discussed earlier,

$$R_{xy} = \frac{V_{xy}}{I} = \frac{B}{ne}. \quad (2.10)$$

Here  $n$  is the electron density. This is the classical Hall effect measured by Edwin Hall in 1879. In 1980, however Von Klitzing however noticed deviations in  $R_{xy}$  from this accepted formula [35]. It was the first observation of perfectly quantized Hall

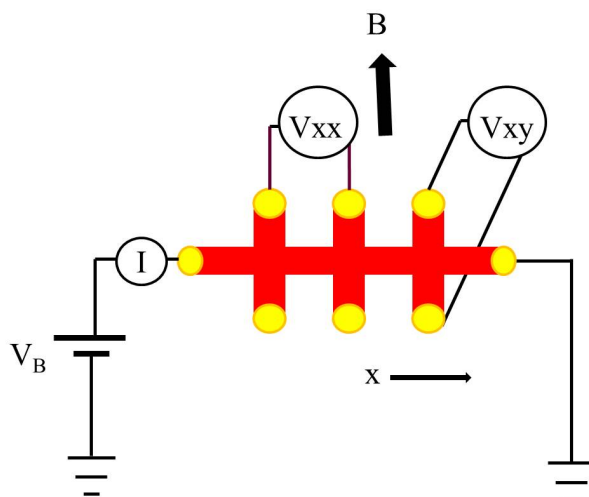


Figure 2.2: A typical quantum Hall measurement configuration

resistance plateaus, as shown in Fig. 2.3 [6].

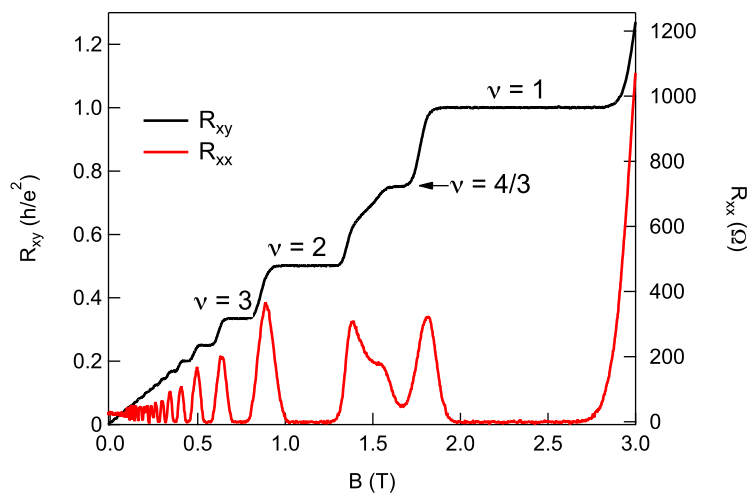


Figure 2.3: A plot of  $R_{xx}$  and  $R_{xy}$  in a single quantum well. Data is from Finck et al. [6]

$$R_{xy} = \frac{V_{xy}}{I} = \frac{h}{\nu e^2}, \quad (2.11)$$

where  $\nu = 1, 2, 3, 4\dots$ . Equating Eq. 2.10 to Eq. 2.15 gives

$$\frac{B}{ne} = \frac{h}{\nu e^2}, \quad (2.12)$$

$$n = \frac{\nu e B}{h} = \nu D. \quad (2.13)$$

In more physical terms,  $\nu$  completely filled Landau level contributes exactly  $h/\nu e^2$  to the Hall resistance.  $\nu$  is the filling factor defined as

$$\nu = \frac{N\phi_0}{\phi} = \frac{n}{D}, \quad (2.14)$$

where  $\phi$  is the flux divided by flux quanta  $\phi_0 = h/e$ . However,  $R_{xy}$  according to Eq. 2.10 is a straight line plotted versus  $B$ . So it cannot explain the existence of plateaus as in Fig. 2.3.

The role of disorder is crucial in understanding the perfectly quantized Hall plateaus. The disorder causes broadening of the Landau levels, as shown in Fig 2.1 (c). The purple bands are delocalized whereas the blue *DOS* are localized. When the magnetic field is increased, the spacing in energy between the Landau levels increases proportionally. This causes the Fermi energy to sweep through different Landau levels. When the Fermi energy is within the localized states (blue), it causes no change in the Hall resistance, whereas when the Fermi energy goes through the extended states (purple), the Hall resistance registers a sharp change.

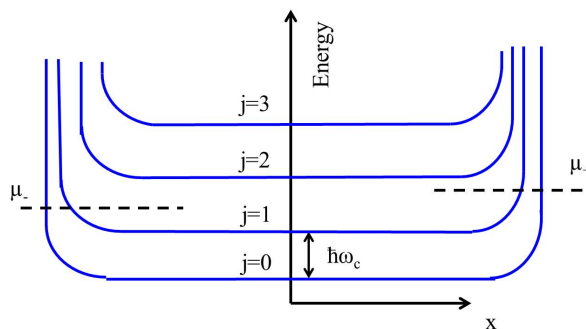


Figure 2.4: The Landau levels plotted against the sample width  $x$ .

The other interesting observation is that the contribution of each completely filled Landau level to the Hall resistance is  $h/e^2$ . It can be understood in the Landauer-Buttiker formalism [44, 45] that a single ballistic conduction channel has a four terminal resistance of  $h/e^2$ . In the case of integer quantum Hall effect, the ballistic conduction channels are extended “edge channels” present along the boundaries of the Hall bar device. The electrons in the bulk are localized/pinned due to disorder. The number of such ballistic “edge channels” is determined by the number of completely filled Landau levels. Fig. 2.4 depicts the chemical potential located between  $j = 1$  and  $j = 2$  Landau levels.

The discovery of integer quantum Hall effect had importance to metrology as well.  $h/e^2$  is known within a relative uncertainty of  $3 \times 10^{-10}$  and is also used in the measurement of the fine structure constant  $\alpha = e^2/\hbar c$ .

## 2.3 Fractional Quantum Hall Effect

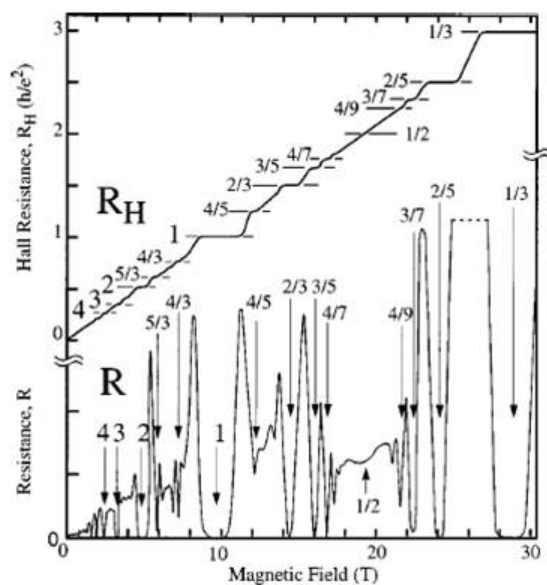


Figure 2.5: A plot of longitudinal and transverse Hall resistance in a ultra high mobility single quantum well [7].

With the invention of modulation doping, the quality of the two dimensional

electron gas improved sharply. On one such sample, Tsui and Stormer measured for the first time a quantized Hall plateau at [36]

$$R_{xy} = \frac{V_{xy}}{I} = \frac{3h}{e^2}. \quad (2.15)$$

This was the first observation of a fractional quantum Hall state, a plethora of which have been discovered since, as shown in Fig. 2.5.

### 2.3.1 Laughlin wavefunctions

Laughlin gave an elegant explanation to the emergence of a quantized Hall plateau when only a third of the lowest Landau level was full [57]. He assumed a variational approach. He found a generalization of Eq. 2.9

$$\phi_{\frac{1}{(2m+1)}}(z_1, z_2, \dots, z_N) = \prod_{j < k} (z_j - z_k)^{(2m+1)} e^{-\frac{1}{4} \sum_i |z_i|^2}, \quad (2.16)$$

where  $m$  is a positive integer and the wavefunction to be to be antisymmetric under exchange. These Laughlin wavefunctions enforce that electrons avoid sitting on top of each other by going to zero when this happens. By enforcing this with a higher power  $(2m + 1)$ , an electron is able to repel all other electrons even more strongly.

Thus the Laughlin wavefunctions provide a very intuitive understanding of the fractional Hall states at  $\nu = j + 1/(2m + 1)$ , where  $j = 0, 1, 2, 3, \dots$  like  $1/3, 1/5, 1/7$  etc. Also, the Laughlin wavefunctions are applicable to FQHE states at  $\nu = j + 1 - 1/(2m + 1)$  like  $2/3, 4/5, 6/7$  etc. by applying the same reasoning to holes. But there are others like the  $2/5, 3/5, 4/7$  in Fig. 2.5 etc. that are not captured by Laughlin's formalism.

### 2.3.2 Composite Fermions

The composite fermion theory [46] allow one to understand the IQHE and the FQHE within a unified framework. Composite fermion theory is a generalization of Laughlin

wavefunctions. The Laughlin wavefunctions  $\phi$  are essentially [57]

$$\phi_{\frac{1}{(2m+1)}} = \prod_{j < k} (z_j - z_k)^{2m} \phi_1, \quad (2.17)$$

where  $m$  is an integer and  $\phi_1$  is the wavefunction for the lowest  $LL$  completely occupied. The  $2m$  is a requirement of electrons being fermions. The intuition behind composite fermions is that [46]

$$\phi_{p^*} = \prod_{j < k} (z_j - z_k)^{2m} \phi_{\pm p}, \quad (2.18)$$

where  $m$  is an integer and  $\phi_{\pm p}$  is the wavefunction for the  $p$   $LL$  completely occupied. The  $\pm$  corresponds to the magnetic field in the  $+z$  or  $-z$  direction. So in the integer quantum Hall state,  $\pm 1/p$  flux quanta were available per electron. In the composite fermion state,  $\pm 1/p + 2m$  flux quanta are available per electron, explaining the fractional quantum Hall state at filling factor  $p^*$ :

$$p^* = \frac{p}{(2mp \pm 1)}. \quad (2.19)$$

It explains the origin of most observed FQHE states, for example  $2/5$ ,  $3/5$ ,  $4/7$ , etc., not captured by Laughlin's wavefunctions. Note that all the fractional quantum Hall states predicted by Laughlin's formalism and the composite fermion theory are odd denominator functions.

## 2.4 Conclusion

The study of IQHE and FQHE has enriched the understanding of correlated electrons. The Laughlin wavefunctions and composite fermion theory give an understanding of how even though electronic charge  $e$  is indivisible, the manifestations in transport can appear to be due to fractional charge. Finally, even while a lot of fractions were explained, newer ones kept emerging as the mobility of the samples improved;

for example, the FQHE at filling fractions  $\nu = 5/2$  [47] and  $\nu = 7/2$  [48] and the quantum Hall stripe phases at filling fractions  $\nu = 9/2, 11/2, 13/2$  etc. [58] that could not be understood within the folds of these theories.

## Chapter 3

# Quantum Hall Exotica at $\nu_T = 1$

In single layers at filling factor  $\nu = 1/2$  when the electron density equals half the lowest spin-resolved Landau level, there is no fractional quantum Hall effect (FQHE). In a double quantum well system the centre-to-centre separation  $d$  between the two quantum wells is fixed for a given sample but the density can be tuned using the global top and back gates. This allows one to tune the magnetic length  $l = \sqrt{\hbar/eB}$  for a particular quantum Hall state. In the limit of large effective layer separation  $d/l \gg 1$ , the two electron gas layers behave as independent of each other. The quantum Hall effect (QHE) exhibited corresponds to two individual composite Fermion seas at filling fraction  $\nu = 1/2$ .

A more interesting limit is when effective layer separation  $d/l \ll 1$ . In this limit, the strength of interlayer and intralayer Coulomb interaction is comparable. One can anticipate new bilayer quantum Hall states to develop as a result of interlayer Coulomb repulsion that does not exist in single layers. The  $\nu_T = 1/2 + 1/2 = 1$  and  $\nu_T = 1/4 + 1/4 = 1/2$  observed in bilayers are prominent examples of bilayer quantum Hall states [1].

The work presented in this thesis focuses on the  $\nu_T = 1$  state at intermediate layer separations where the two layers exhibit strong Coulomb correlations.

### 3.1 Quantum Hall effect at $\nu_T = 1$

The first observation of  $\nu_T = 1$  by Eisenstein et al. [1] was in MBE grown bilayer samples where the GaAs quantum wells were separated by a pure AlAs barrier. Two new bilayer quantum Hall states were observed, namely  $\nu_T = 1$  and  $\nu_T = 1/2$ . Each of these states exhibit a signature minima in  $\rho_{xx}$  and accurately quantized plateau in  $\rho_{xy}$  as presented in Fig. 3.1. The states were found to be robust to application of in-plane magnetic fields, which is known to suppress tunneling between the two layers. This indicated that tunneling was not crucial to the origin of the states [1].

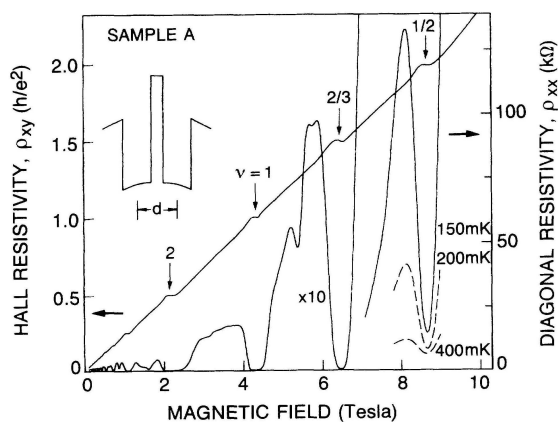


Figure 3.1: A plot of longitudinal and transverse Hall resistance in a high mobility bilayer quantum well after Eisenstein et al. [1]

The  $\nu_T = 1$  state in the limit of effective layer separation  $d/l \ll 1$  is captured in essence by the Halperin “111 state”. A pseudospin ferromagnet and an exciton condensate are also exactly equivalent theoretical descriptions of the  $\nu_T = 1$  state. Each of these will be discussed in further detail below.

#### 3.1.1 111 state

Halperin generalized the Laughlin wavefunction to a two-component system [59].

$$|\phi_m\rangle = \prod_{j < k} (z_j - z_k)^{m_1} \prod_{r < s} (w_r - w_s)^{m_2} \prod_{j,r} (z_j - w_r)^{m_3} e^{-\frac{1}{4} \sum_j |z_j|^2 + \sum_r |w_r|^2}, \quad (3.1)$$

where  $z_j$  and  $w_r$  denote the (x,y) coordinates of the electrons in the top and bottom layers, respectively. In Halperin's initial consideration, a two-component internal degree of freedom like electron spin was considered. However, it applies equally well to layer indices in a bilayer 2DEG [60]. The Landau level filling factors  $\nu_1$  and  $\nu_2$  corresponding to the two components are given by

$$\nu_1 = \frac{m_2 - m_3}{m_1 m_2 - m_3^2}, \quad (3.2)$$

and

$$\nu_2 = \frac{m_1 - m_3}{m_1 m_2 - m_3^2}. \quad (3.3)$$

The bilayer wavefunctions are denoted as  $(m_1, m_2, m_3)$ . Prominent bilayer states are [55].

$$\nu_T = 1 : (111), \quad (3.4)$$

$$\nu_T = \frac{1}{2} : (331), \quad (3.5)$$

The “111 state” is the one we are interested in. In this state, an electron in one layer is bound to a vortex or a hole in the other layer. Strictly speaking, this wavefunction describes the system when effective layer separation  $d/l = 0$ .

### 3.1.2 Pseudospin Ferromagnetism

Another exactly equivalent language to describe the “111 state” is that of pseudospin ferromagnetism. An electron occupying the top layer is denoted as  $|\uparrow\rangle$  and an electron occupying the bottom layer is denoted as  $|\downarrow\rangle$  [61, 62, 63, 64]. Each electron is in a coherent superposition of being in the top and the bottom layers. It is represented by the following wavefunction:

$$|\Psi\rangle = \prod_k \frac{1}{\sqrt{2}} (|\uparrow\rangle + e^{i\phi} |\downarrow\rangle) \otimes |k\rangle. \quad (3.6)$$

Here  $k$  runs over all the momentum eigenvectors for the lowest Landau level. The important thing is that the phase  $\phi$  is the same for all the electrons. Thus the system

has macroscopic interlayer phase coherence. The system spontaneously breaks  $U(1)$  rotational symmetry in the interlayer phase [65]. This phase  $\phi$  plays the same role as the superconducting order parameter and gradients in the pseudospin phase cause supercurrents.

$$J = \rho_s \nabla \phi, \quad (3.7)$$

where  $\rho_s$  is the pseudospin stiffness. The system is governed by the Hamiltonian [65, 3]

$$H = \int d^2r (\rho_s (\nabla \phi)^2 + \frac{e^2}{2C} M_z^2 - \Delta \cos \phi). \quad (3.8)$$

This is a long-wavelength approximation. The first term is the energy cost to create gradients in  $\phi$ . The second term is basically capacitive energy cost for charge imbalance in the two layers. Here  $C$  = capacitance between the two layers per unit area and  $M_z = \nu_1 - \nu_2$ , which is the difference in layer filling factor. The last term is a Josephson potential energy term.  $\Delta = \Delta_{SAS} \frac{n}{2}$ , where  $n$  is the electron density and  $\Delta_{SAS}$  is the splitting between the symmetric and antisymmetric states.

### 3.1.3 Exciton condensation

The pseudospin ferromagnet wavefunction in Eq. (3.6) can be written down in second-quantized notation as

$$|\Psi\rangle = \prod_k \frac{1}{\sqrt{2}} (C_{\uparrow,k}^\dagger + e^{i\phi} C_{\downarrow,k}^\dagger) |0\rangle, \quad (3.9)$$

$$|\Psi\rangle = \prod_k \frac{1}{\sqrt{2}} (1 + e^{i\phi} C_{\downarrow,k}^\dagger C_{\uparrow,k}) (C_{\uparrow,k}^\dagger |0\rangle). \quad (3.10)$$

$C_{\uparrow,k}^\dagger$  and  $C_{\downarrow,k}^\dagger$  are the electron creation and annihilation operators of wavevector  $k$  in the top and bottom layers, respectively. This we can simplify as

$$|\Psi\rangle = \prod_k \frac{1}{\sqrt{2}} (1 + e^{i\phi} C_{\downarrow,k}^\dagger C_{\uparrow,k}) |0'\rangle. \quad (3.11)$$

$|0'\rangle$  represents the lowest Landau level for the top layer when completely filled and lowest Landau level for the bottom layer when completely empty. The resemblance of Eq. 3.11 to BCS ground state of a superconductor is clear. Each exciton has the same macroscopic phase  $\phi$ . The one noticeable difference is that the system has charge neutral excitons instead of charge  $2e$  Cooper pairs [65]. We will discuss various experiments that have borne out several aspects of this ground state wavefunction of the  $\nu_T = 1$  state to be true.

## 3.2 Transport anomalies

Exciton condensation was predicted [66, 67] back in 1962. However, efforts to realize exciton condensation in optically generated excitons suffered from short recombination times. Lozovik and Yudson realized back in 1975 that it was possible to circumvent this problem of electron-hole recombination in spatially separated electron hole systems [32, 33]. Lerner and Lozovik proposed that an electron-hole system in a strong enough magnetic field to have only the lowest Landau level occupied is an ideal Bose gas [34]. However, the test of these ideas was only possible after the technological advance of separately contacting bilayer quantum Hall systems due to Eisenstein et al. [5]. With the discovery of the  $\nu_T = 1$  state [1], which was a strong candidate for being an exciton condensate, it offered an opportunity to investigate these ideas through tunneling and counterflow transport in Hall bar devices.

### 3.2.1 Phase transition at $\nu_T = 1$

The phase transition between two compressible  $\nu = 1/2$  Fermi liquids to an incompressible quantum Hall state at  $\nu_T = 1$  was carefully mapped out by Murphy et al. [8]. This was done on several samples with varying the single particle tunneling gap  $\Delta_{SAS}$  by putting different Al concentrations in the  $\text{Al}_x\text{Ga}_{1-x}\text{As}$  barrier layer. Interestingly, the phase transition in the limit of no tunneling happens for  $d/l \approx 2$ . This is evidence that interlayer coulomb repulsion alone can drive the phase transition to  $\nu_T = 1$  even in the absence of tunneling. This is also corroborated by measurements

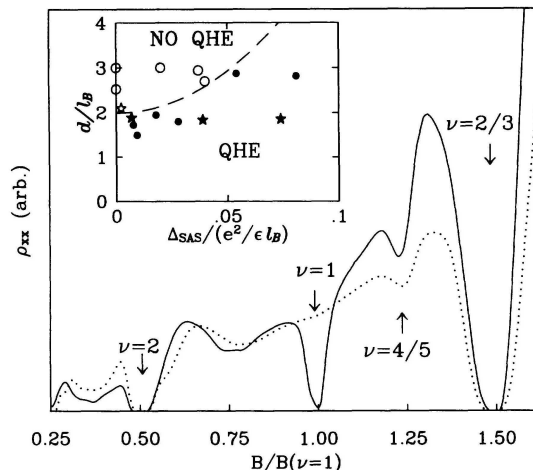


Figure 3.2: The resistivity  $\rho_{xx}$  exhibits a QHE at  $\nu_T = 1$  for total electron density =  $1.26 \times 10^{11}$  and no QHE for total electron density =  $1.45 \times 10^{11}$ . Inset: Map of the phase diagram of the  $\nu_T = 1$  state as a function of tunneling strength. This data is due to Murphy et al. [8].

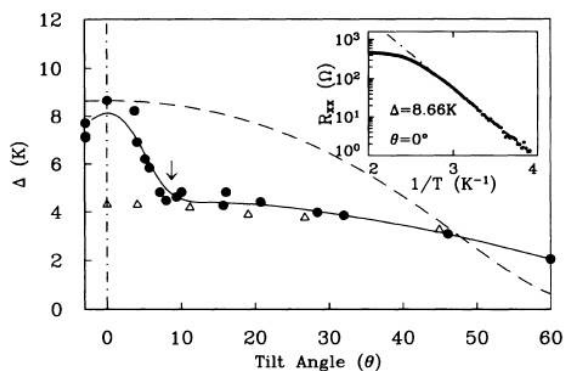


Figure 3.3: The quantum Hall gap  $\Delta$  vs. tilt angle  $\theta$  in a weakly tunneling sample. The black dots are for  $\nu_T = 1$  state. The triangles are for  $\nu_T = 2/3$  state. This data is due to Murphy et al. [8].

of the quantum Hall gap at  $\nu_T = 1$  as a function of tilt angle shown in Fig. 3.3 in a sample of symmetric-antisymmetric gap  $\Delta_{SAS} = 0.8$  K. The tilting allows one to apply an in-plane magnetic field  $B_{\parallel}$  while holding the magnetic field perpendicular to the sample  $B_{\perp}$  fixed. In Fig. 3.3, it is observed that there is an initial suppression of tunneling to about  $\theta = 8$  degrees. Above  $\theta \approx 8$  degrees, the quantum Hall gap has a much weaker tilt angle dependence. Also, the quantum Hall gap at  $\nu_T = 1$  survives

for tilt angles even as large as  $\theta = 60$  degrees. This indicates that the initial quantum Hall state close to  $\theta = 0$  degrees which is highly sensitive to in-plane magnetic field is stabilized due to single particle tunneling. However at  $\theta > 8$  degrees, a different quantum Hall ground state is preferred which is rather insensitive to in-plane magnetic field. This state is stabilized due to interlayer Coulomb correlations and can exist even when tunneling is completely suppressed [8].

### 3.2.2 Resonantly enhanced tunneling

Tunneling spectroscopy is a powerful tool to study Coulomb correlations. It has been of singular importance in studies of the bilayer quantum Hall effect. When the effective layer separation  $d/l$  is large and Coulomb interactions between the two layers is negligible, it takes finite voltage to tunnel an electron into the other layer. This is because this tunneling process disrupts the interlayer correlation of electrons in a strong magnetic field for the layer from which the electron leaves and also in the layer where the electron enters. This energy penalty is marked by a Coulomb gap in the tunneling conductance at zero bias [12]. In Fig. 3.4 (A) and Fig. 3.4 (B), this is the

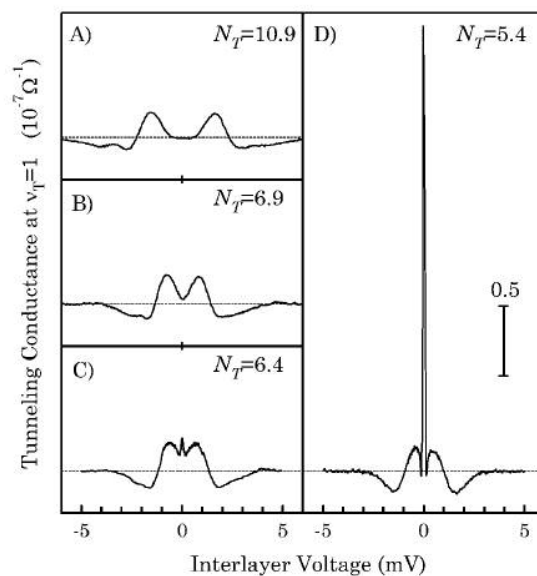


Figure 3.4: Tunneling conductance  $dI/dV$  vs interlayer voltage  $V$ . The total electron density is  $N_T \times 10^{10} \text{cm}^{-2}$ . Results are due to Spielman et. al. [2]

case. However, with lowering of electron density, a small peak appears in the middle of the Coulomb gap as shown in Fig. 3.4 (C). The onset of the tiny peak marks a phase transition from the two electron layers having negligible interlayer Coulomb interactions to having an interlayer correlated state at  $\nu_T = 1$ . On further decrease in electron density, a pronounce peak appears at zero bias, as was first discovered by Spielman et. al. [2]. This peak evidences spontaneously broken  $U(1)$  rotational symmetry in the  $\nu_T = 1$  state. It bears resemblance to the *dc* Josephson effect, as will be discussed in greater depth in Chapter 4. Such a signature of *dc* Josephson effect in tunneling in bilayers at  $\nu_T = 1$  was first predicted by Wen and Zee. [68, 69]

### 3.2.3 Goldstone mode

The order parameter  $\phi$  has a  $U(1)$  rotational symmetry that the system breaks spontaneously. This broken symmetry should be associated with a Goldstone mode [70]. On application of in-plane magnetic field to the tunneling spectrum, just such a collective mode was discovered by Spielman et al. [9].

It was observed that two split-off peaks appeared at finite voltages  $\pm V^*$  with the application of an in-plane field and moved further apart as the strength of the in-plane magnetic field was increased. This mode was found to have a linear dispersion relation with the magnetic wavevector  $q = eB_{\parallel}d/\hbar$ . An intriguing observation was that the zero bias peak survived and only got suppressed by  $B_{\parallel}$  [9]. Ideally, one expects to observe a Fraunhofer diffraction pattern just as in the *dc* Josephson effect [71].

$$I = J_c \int_{-L/2}^{L/2} \sin(\phi + qx) dx, \quad (3.12)$$

$$I = \frac{2J_c \sin(qL/2)}{q} \sin \phi. \quad (3.13)$$

Here  $J_c$  is the critical current density. Instead, if phase coherence decays with distance  $x$  exponentially as  $P(x) = \frac{e^{-|x|}}{2\xi}$ , then the current density decays as a Lorentzian with  $B_{\parallel}$  in agreement with experimental findings by Spielman et al. [71]. Here  $\xi$  is the

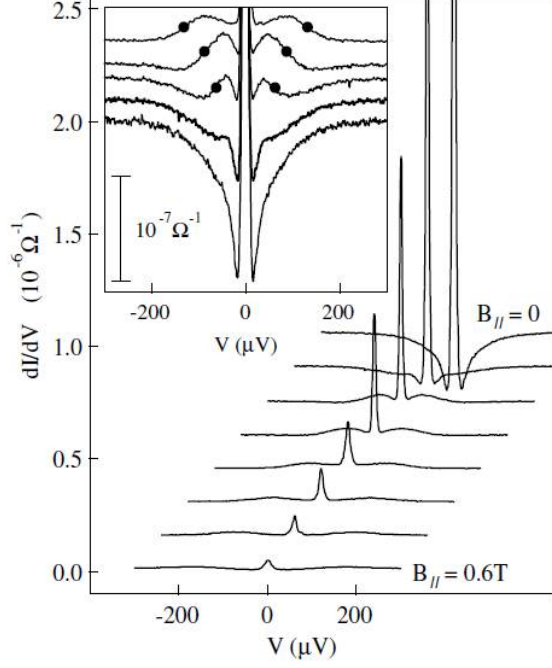


Figure 3.5: Evolution of tunneling conductance spectra with application of in-plane magnetic field.  $B_{\parallel} = 0, 0.11, 0.24, 0.29, 0.35, 0.43, 0.49,$  and  $0.59$  T. Results are from Spielman et al. [9].

exciton correlation length [71].

$$I = J_c \int_{-\infty}^{\infty} \sin(\phi + qx)P(x)dx, \quad (3.14)$$

$$I = \frac{J_c}{1 + q^2\xi^2} \sin \phi. \quad (3.15)$$

### 3.2.4 Vanishing Hall resistance in counterflow

The transverse Hall resistance was measured by Kellogg et al. and Wiersma et al. in electron bilayers and Tutuc et al. in hole bilayers at  $\nu_T = 1$  [10, 72, 73]. For Hall resistance measurements made with both layers in parallel, a quantized Hall plateau was observed in  $R_{xy}$  at  $\nu_T = 1$  and coincided with a deep minima in  $R_{xx}$ . This measurement is similar to that of a conventional Hall effect.

When current was injected into one layer and withdrawn and re-injected into the

other layer in order to set up a counterflow configuration, a vanishing Hall voltage was observed [10, 72, 73]. Kellogg et al.'s counterflow measurements were done with

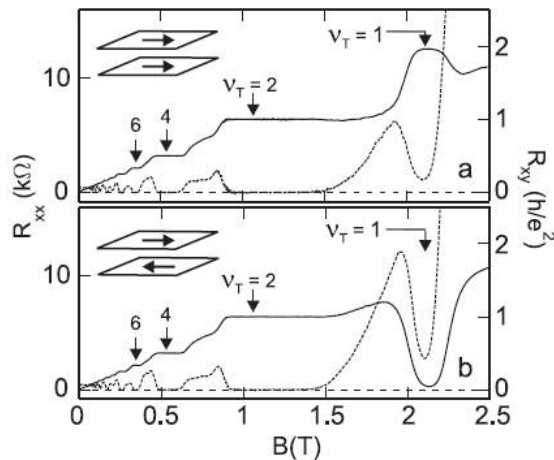


Figure 3.6: The solid and dotted traces represent the  $R_{xy}$  and  $R_{xx}$  in a bilayer, respectively. The temperature  $T = 50$  mK and  $d/l = 1.58$ . (a) Currents are in parallel. (b) Currents are anti-parallel in the two layers. Results are reproduced from Kellogg et al. [10]

the tunneling between the layers less than 1% of the counterflow current. Otherwise, the interpretation of the vanishing Hall voltage as due to bound electron-hole pairs not experiencing Lorentz's deflection would be harder. Counterflow measurements in Hall bar geometry in the presence of Josephson-like tunneling has been explored by Yoon et al. [74].

Thus the quantized Hall drag experiment [16] and the vanishing Hall resistance in counterflow configuration [10, 72, 73] complement each other. Both these observations are consistent with counterflow superfluidity due to transport being mediated by charge neutral excitons.

### 3.3 Conclusion

The first signatures of Bose Einstein condensation of excitons in the bilayer  $\nu_T = 1$  state [1] came through transport measurements with the observation of  $dc$ -Josephson-

like phenomenon in tunneling [2] and counterflow superfluidity [10, 72, 73]. However, these Hall bar measurement were inconclusive about the exciton transport being an edge or a bulk phenomenon. Furthermore, the presence of a dissipationless edge channel complicated the interpretation of the Hall bar measurements. The studies presented in this thesis are in a Corbino geometry precisely to address these issues.

## Chapter 4

# Interlayer tunneling at $\nu_T = 1$

A spectacular tunneling phenomenon in bilayers happens at  $\nu_T = 1$  when the two electron gas layers develop interlayer phase coherence. This is marked by a tunneling  $I - V$  that is reminiscent of the *dc* Josephson effect. The first experimental observation of such a phenomenon came in two terminal conductance measurements at  $\nu_T = 1$  by Spielman et. al. [2] as discussed in Chapter 3. But the zero bias tunneling conductance was finite and about  $10^{-6} \Omega^{-1}$ . This observation led to several theoretical papers to develop an understanding of why the peak conductance was finite and small and also whether this resonantly enhanced tunneling peak actually had to do with the *dc* Josephson effect or not [37, 75, 76, 77, 78]. Stern et al. attributed the lack of a true *dc* Josephson effect to density inhomogeneities in the bilayer [37].

In superconducting Josephson junctions, subjecting the tunnel junction to an in-plane magnetic field leads to the Fraunhofer diffraction pattern. This motivated studies of the effect of in-plane magnetic field on the resonant tunneling at zero bias [71]. A suppression of the zero bias peak was observed with increasing  $B_{\parallel}$  [9] as shown in Chapter 3. However, no Fraunhofer diffraction pattern has been observed. The role of disorder in washing away the Fraunhofer diffraction pattern has been investigated by several theoretical works. They consider the exciton Josephson junctions have correlation length  $\xi$ . In this case, the applied in-plane magnetic field is found to reduce the zero bias tunneling conductance by a Lorentzian in agreement with the experiment [37, 71, 79, 3]. But new tunneling peaks were observed at finite biases in the presence of  $B_{\parallel}$  and proved the existence of a low energy Goldstone mode being

present [37, 9]. For a more in-depth discussion, refer to Chapter 3.

Experiments by Tiemann et al. revealed that the four terminal tunneling indeed had a “supercurrent” branch with vanishingly small interlayer voltage until a critical current  $I_c$  and then abruptly transitioned into a resistive branch much like in superconducting Josephson junctions [39]. Finck et al. and Tiemann et al. established that the tunneling peak height as well as the critical current  $I_c$  scaled with area and the tunneling was a bulk phenomenon [80, 42].

Even after being a subject of vigorous research for more than a decade, the Josephson-like tunneling presents several intriguing questions. The dissipation in the “supercurrent” branch was unknown. Even though the tunneling  $I - V$  resembled an overdamped Josephson junction, the reason behind this wasn’t clear. The magnitude of the critical current  $I_c$  is  $10^5$  times smaller than expected for a clean exciton superfluid. Two recent theoretical works have attempted to explain what causes this suppression [79, 3]. All these unresolved questions motivated us to investigate deeply the tunneling at  $\nu_T = 1$  and the findings are presented in this chapter. The tunneling measurements were done in a Corbino geometry.

## 4.1 Corbino Device

We study tunneling between two 18 nm GaAs quantum wells separated by a 10 nm  $\text{Al}_{0.9}\text{Ga}_{0.1}\text{As}$  tunnel barrier. The as-grown mobility of each quantum well is  $\approx 1 \times 10^6 \text{ cm}^2\text{V}^{-1}\text{s}^{-1}$  and as-grown electron density in each layer is  $5.5 \times 10^{10} \text{ cm}^{-2}$ . The sample is patterned into an annular ring with an outer diameter of 1.4 mm and inner diameter of 1.0 mm. This device geometry is called a Corbino geometry. A device image is shown in Fig. 4.1. The device has global top and back gates for independently controlling the electron density in each quantum well. This allows one to change the Fermi-energy  $E_1$  and  $E_2$  in each quantum well.

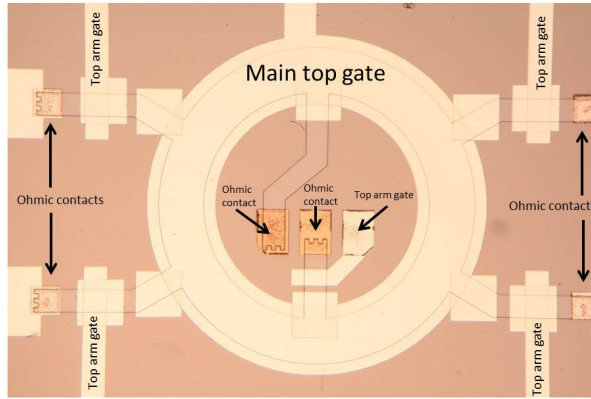


Figure 4.1: The front view of the Corbino device on which the tunneling measurements were performed. On the bottom side main back gates and back arm gates are lithographically patterned as well. Reproduced from Finck's Ph.D. thesis [6].

## 4.2 Interlayer tunneling at zero magnetic field

Interlayer tunneling is very effective in probing the quantum lifetimes of electrons. This is difficult to measure in resistance measurements. A bias voltage is applied across the two layers and the tunneling current is measured. In Fig. 4.2  $n$  refers to the total electron density in both quantum wells. The zero field tunneling measurements are done at equal electron densities in the top and bottom layers. This is done by adjusting the voltages on the main top and bottom gates. The 2D-2D tunneling process conserves in-plane momentum. This is such a stringent requirement that for tunneling between two identical quantum wells it implies that

$$\vec{k}_T = \vec{k}_B, \quad (4.1)$$

where  $\vec{k}_T$  and  $\vec{k}_B$  are the initial and final wavevectors of the tunneling electron. Also,

$$\frac{\hbar |\vec{k}_T|^2}{2m^*} + E_{T,0} = \frac{\hbar |\vec{k}_B|^2}{2m^*} + E_{B,0}, \quad (4.2)$$

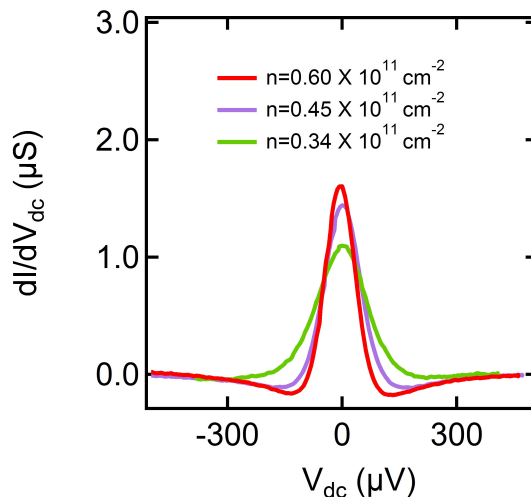


Figure 4.2: Plot of  $dI/dV_{dc}$  vs.  $V_{dc}$ ,  $B = 0$  T and  $T \approx 15$  mK [11].

where  $E_{T,0}$  and  $E_{B,0}$  are the bottoms of the Fermi sea for the top and bottom quantum wells. Eq. 4.1 and Eq. 4.2 have a solution only if

$$E_{T,0} = E_{B,0}. \quad (4.3)$$

Thus, tunneling can happen only if the bottoms of the two Fermi seas coincide. So for the case of both layers being at equal electron density, the  $dI/dV$  vs  $V$  should be a Dirac delta function centered at zero bias. However, in real experiments one measures a symmetric zero bias peak when the two quantum wells have equal electron density. The width of the tunneling peak is a measure of the electron electron scattering lifetime  $\tau_{ee}$  of electrons. Below about 2 K, the width of the tunnel spectra remains independent of temperature. However, it has a strong dependence on the electron density in each layer. This indicates that as the electron density is lowered,  $\tau_{ee}$  decreases due to changes in screening and scattering off static disorder [81].

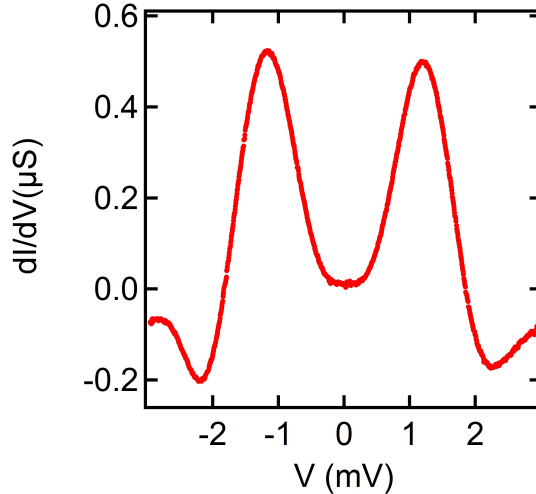


Figure 4.3: Plot of  $dI/dV$  vs  $V$  at  $T \approx 15$  mK, total electron density  $n_T = 0.85 \times 10^{11} \text{ cm}^{-2}$  and  $B = 3.6$  T. First studies were by Eisenstein et al. [12]

### 4.3 Interlayer tunneling at $\nu_T = 1/2 + 1/2$

Application of a strong magnetic field with the two layers held at equal electron density modifies the tunnel spectra as described above. The special case considered here is that of  $\nu_T = 1/2 + 1/2$ , where the electron density in each layer is half the degeneracy of the lowest Landau level. Also, we are at high  $d/l$  when the two layers behave as independent of each other. Strong Coulomb correlations are present within the layers but the Coulomb correlations between the two layers are negligible.

For the tunneling spectra in Fig 4.3, the total electron density in both layers is  $0.85 \times 10^{11} \text{ cm}^{-2}$ . Note that the peak at zero bias in tunneling conductance has been replaced by a minima at zero-bias in the presence of a magnetic field of 3.6 T. Early observations of such a Coulomb gap in tunneling spectra in the quantum Hall regime was by Ashoori et al. [82, 83] using a capacitive coupling technique and Eisenstein et al. [12] using the selective depletion of top and bottom arms, which has been extensively used in this thesis.

The single particle physics that explains the zero magnetic field data in Fig. 4.2 cannot explain the appearance of a broad gap. In a strong magnetic field, the electron liquid in each quantum well is highly correlated and an extraction of an electron out of

it is accompanied by a Coulomb energy penalty  $E_c \approx \frac{e^2}{\epsilon_r \epsilon_0 \langle a \rangle}$  where the interelectron spacing  $\langle a \rangle = 2\sqrt{\pi n}$ . Similarly, the addition of an electron into a strongly correlated electron gas is also accompanied by the same energy penalty. This is because the defect thus created is difficult to relax in the presence of a strong magnetic field [12].

## 4.4 Interlayer coherent tunneling at $\nu_T = 1$

As discussed in Chapter 3, Eisenstein et al. and Murphy et al. demonstrated that the bilayer quantum hall system at  $\nu = 1/2 + 1/2$  undergoes a phase transition from a compressible composite Fermion liquid in each layer to an incompressible quantum Hall state at  $\nu = 1$  [12, 8]. The system goes from negligible interlayer Coulomb correlations to strong Coulomb correlations as it is tuned across the phase boundary by reducing the electron density in each layer. The  $\nu_T = 1$  state exhibits a tunneling anomaly [2] resembling the *dc* Josephson effect in superconducting tunnel junctions discussed in depth in subsection 3.2.2.

## 4.5 Josephson effect at $\nu_T = 1$

One might be intrigued by this comparison to the *dc* Josephson effect in the context of quantum Hall bilayers. Reviewing a simple quantum mechanical problem will help develop an intuitive understanding as to why a Josephson effect is expected for the bilayer quantum Hall state at  $\nu_T = 1$ . Consider an electron of charge  $e$  in a double quantum well where a voltage  $V$  is applied to one of the wells w.r.t to the other. The two quantum wells are separated by a potential barrier with bare tunneling matrix element  $\Delta_{SAS}$ .

$$|\Psi\rangle = A_1 |1\rangle + A_2 |2\rangle, \quad (4.4)$$

$$i\hbar \frac{dA_1}{dt} = \frac{eV}{2} A_1 + \Delta_{SAS} A_2, \quad (4.5)$$

$$i\hbar \frac{dA_2}{dt} = -\frac{eV}{2} A_2 + \Delta_{SAS} A_1, \quad (4.6)$$

$$A_1 = |A_1| e^{i\theta_1}; A_2 = |A_2| e^{i\theta_2}. \quad (4.7)$$

Here  $|\Psi\rangle$  is the wavefunction of the electron.  $A_1$  and  $A_2$  are complex numbers. Basic quantum mechanics leads to:

$$\frac{d\theta}{dt} = \frac{eV}{\hbar}. \quad (4.8)$$

The tunneling current density  $J$  is given by

$$J = e \frac{d}{dt} |A_1|^2 = \frac{e\Delta_{SAS}}{\hbar} |A_1| |A_2| \sin \theta. \quad (4.9)$$

Now these results are generalized to the pseudospin ferromagnet description of  $\nu_T = 1$  as discussed in Chapter 3. The macroscopic wavefunction of the system given by Eq. 3.6 gives

$$|A_1| \rightarrow \sqrt{\frac{n}{2}}; |A_2| \rightarrow \sqrt{\frac{n}{2}}; \quad (4.10)$$

$$J = \frac{ne\Delta_{SAS}}{2\hbar} \sin \theta, \quad (4.11)$$

$$J = \frac{e\Delta_{SAS}}{4\pi l^2 \hbar} \sin \theta. \quad (4.12)$$

Here  $n$  is the total density of electrons per unit area and  $l$  is the magnetic length. Thus from very simple considerations, a Josephson effect is expected at  $\nu_T = 1$ .

### 4.5.1 Two terminal tunneling

In the tunneling measurements, source and drain contacts are each placed on opposite layers and on the same rim. A voltage  $V_{dc}$  is applied and the tunneling current  $I$  is measured in response to this excitation. In Fig. 4.4, the two terminal tunneling  $I$  vs.  $V_{dc}$  is plotted for contacts on the outer rim. The data exhibits a sharp change in resistance at critical current  $I_c$ . This is considered to mark a transition from a static interlayer phase to a time dependent interlayer phase in analogy to the  $dc$ -Josephson effect. Another observation is that the two terminal  $I$  vs.  $V_{dc}$  has a non-linearity at small biases. This is understood to be an effect external to the exciton condensate and is attributed to non-linearities present in the arm resistances [6].

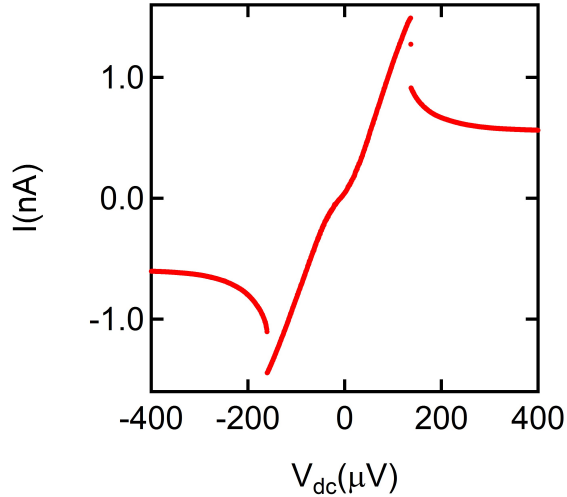


Figure 4.4: Plot of  $I$  vs  $V_{dc}$  on outer rim at  $T = 15$  mK,  $d/l = 1.5$ .

#### 4.5.2 Four terminal tunneling

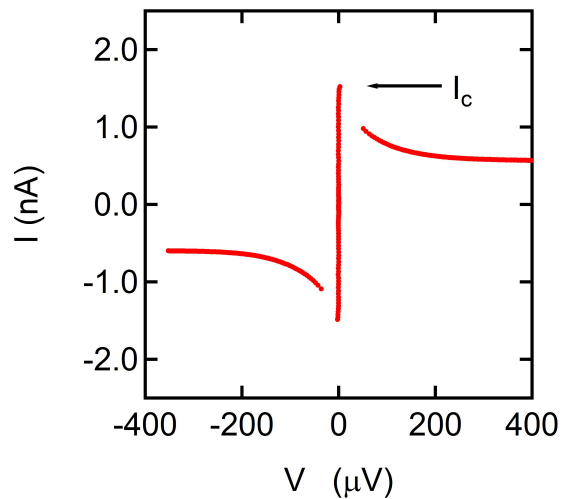


Figure 4.5: Plot of  $I$  vs  $V$  on outer rim at  $T = 15$  mK,  $d/l = 1.5$ .

The intrinsic tunneling  $I - V$  is obtained by measuring the four terminal voltage drop  $V$  across the tunnel junction while simultaneously measuring the tunneling current  $I$ . This tunneling  $I - V$  removes effects of series resistances,  $h/e^2$  resistance for tunneling into the  $\nu_T = 1$  quantum Hall state etc.

At zero bias, tunneling current flows with  $V$  remaining negligible until a critical

current  $I_c = 1.5$  nA in Fig. 4.5. This we will refer to as the “supercurrent” branch. Then abruptly the voltage across the tunnel junction jumps to a finite value. This is captured in Fig. 4.5 and Fig. 4.7. Also, there is a data gap near the transition between the “supercurrent” branch and the resistive branch. This can be understood in simple terms. According to Kirchoff’s law,

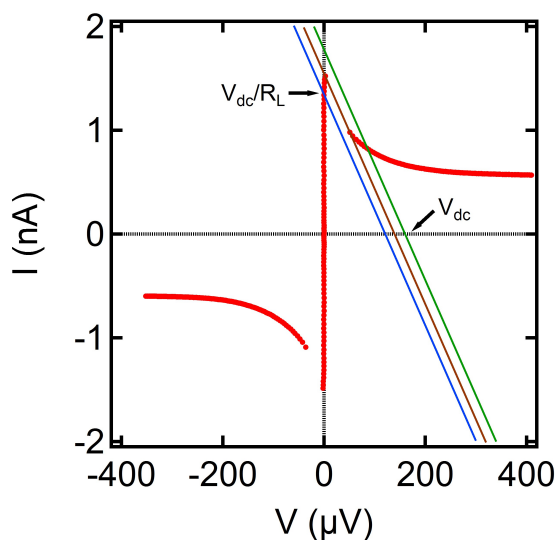


Figure 4.6: Plot of the load lines for resistance  $R_L = 90$  KOhms and  $V_{dc} = 120$   $\mu$ V,  $140$   $\mu$ V,  $160$   $\mu$ V for the blue, brown, and green lines. This is plotted against the intrinsic tunneling  $I - V$  curve.

$$V_{dc} = V + IR_L, \quad (4.13)$$

where  $R_L$  is the load resistor and Eq. 4.13 is the load line. Here  $R_L$  is the total resistance in series to the  $\nu_T = 1$  tunnel junction. This includes arms resistances,  $h/e^2$  from IQHE and any other external resistors  $R_{ext}$ . From the two terminal data, we determine  $R_L \approx 90$  KOhms when  $R_{ext} = 0$ . In Fig. 4.6, the loadline is plotted for  $V_{dc} = 120$   $\mu$ V,  $140$   $\mu$ V,  $160$   $\mu$ V. The intersection of the intrinsic  $I - V$  to the load lines determine the operating point. For  $V_{dc} = 120$   $\mu$ V and  $160$   $\mu$ V, the load line only has 1 operating point. Whereas for  $V_{dc} = 140$   $\mu$ V, the operating point is not unique. This is the reason for the data gap and instability. Such instability is characteristic

of  $I - V$  curves with negative differential resistance.

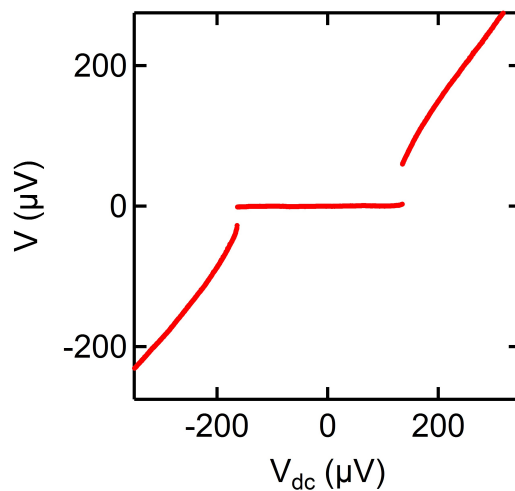


Figure 4.7: Plot of  $V$  vs  $V_{dc}$  on outer rim at  $T = 15$  mK,  $d/l = 1.5$ .

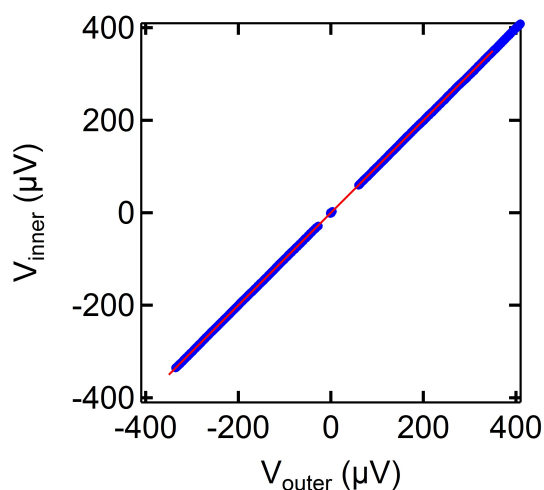


Figure 4.8: Plot of  $V_{inner}$  vs.  $V_{outer}$  on outer rim at  $T = 15$  mK,  $d/l = 1.5$ .

Interestingly, in the entire tunneling  $I - V$ , the measured four-point voltage on the inner and outer rims remains equal in both the “supercurrent” branch and the dissipative branch as shown in Fig. 4.8

It may be intriguing that the shape of the four-terminal tunneling  $I - V$  is at variance to one observed in a normal superconducting Josephson junction. These

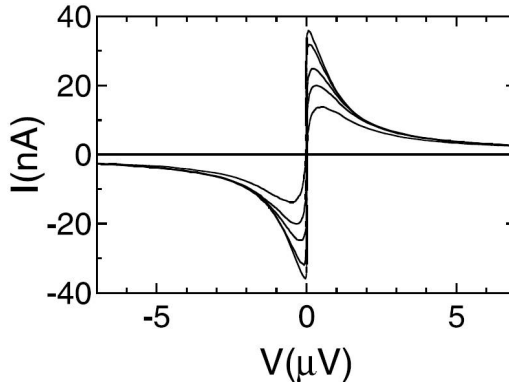


Figure 4.9: Temperature dependence of a voltage biased Josephson Junction.  $T = 34, 98, 245, 400, 622$  mK, respectively, from top to bottom. This data is from Steinbach et al. [13].

junctions are well described by a RSJ model and are current biased. But our bilayer tunneling  $I - V$  are recorded while sweeping the bias voltage. Therefore, these junctions are closer to voltage biased Josephson junction [71, 3]. A voltage biased overdamped Josephson junction as shown in Fig. 4.14 was measured by Steinbach et al. [13]. Their Josephson tunneling  $I - V$  is presented in Fig. 4.9.

### 4.5.3 Temperature dependence of tunneling

In Fig. 4.10 the evolution of the four-terminal tunneling  $I - V$  is studied with temperature. It is found that the “supercurrent” branch becomes non-vertical at elevated temperatures. Also, the data gap near  $I_c$  at  $T = 15$  mK is not present in the higher temperature curves at  $T = 100$  mK and above. This is because at higher temperatures, the resistive branch no longer has a pronounced negative differential resistance.

The resemblance between the voltage biased Josephson junction in Fig. 4.9 and Fig. 4.10 is striking. Also, the bilayer tunneling  $I - V$  data at all temperatures have contributions from incoherent tunneling processes as well at large biases. This might explain why the tunneling current does not go to zero at large voltages. Note that the tunneling critical current  $I_c$  diminishes monotonically with increasing temperature. Also, the tunneling “supercurrent” branch becomes less vertical at higher

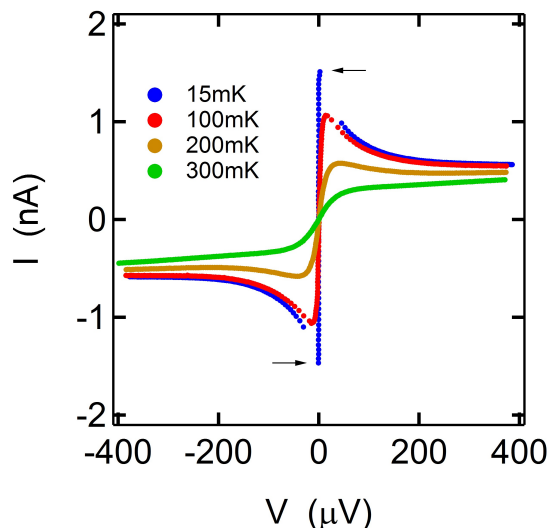


Figure 4.10: Temperature dependence of tunneling  $I - V$ ,  $d/l = 1.5$

temperatures.

#### 4.5.4 Resistance of “supercurrent” branch

Whether the resistance of the four terminal tunneling  $I - V$  in Fig. 4.10 remains finite at measurable temperatures has been a prominent question since the discovery of this resonant tunneling feature [37, 84, 75, 76, 77, 85, 86, 78, 87]. This is subjected to careful study here. Firstly, in the usual four terminal tunneling configuration, the voltage probes are spatially separated along the rim. Ideally, the voltage drop we are most interested is at the same location, vertically between the two layers. So one needs to subtract the intralayer contributions. This is exactly what is done. So the resistance  $R_s$  is the vertical voltage drop divided by the tunneling current. The tunneling current here is a small fixed ac excitation of  $I = 0.2$  nA at 13 Hz.

This resistance remains finite at the lowest possible temperatures. At  $T = 30$  mK, the resistance  $R_s$  is about 100 Ohms. This is 6000 times smaller than the tunneling resistance at zero magnetic field. Thus, correlations result in a huge enhancement in tunneling at  $\nu_T = 1$ . The black dashed line in Fig. 4.11 is for thermally activated behavior with gap = 450 mK. This value is close to the measured quantum Hall gap

for  $\nu_T = 1$ . In conclusion, the resistance in the “supercurrent” branch shows a roughly thermally activated behavior.

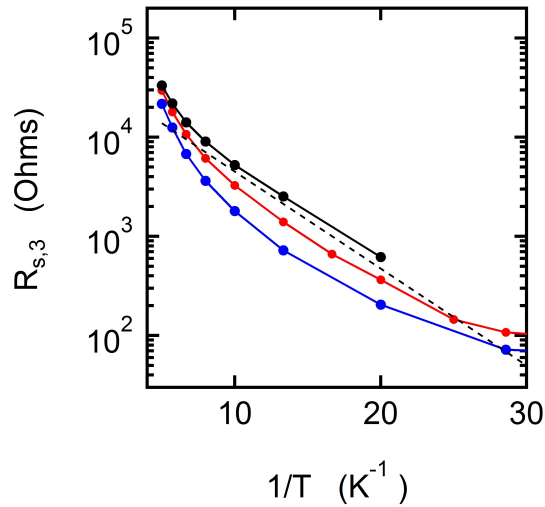


Figure 4.11: Plot of resistance  $R_s$  vs inverse temperature at  $d/l = 1.5$  for three different source drain configurations.

Interestingly, the supercurrent branch in a superconducting tunnel junction also has finite non-zero resistance at any finite temperature [88]. The zero-bias resistance of an overdamped superconducting tunnel junction also follows an Arrhenius behavior  $\approx e^{-2E_J/K_B T}$  where  $E_J$  is the Josephson energy [89].

A possible mechanism leading to this dissipation is that the system has topological defects or merons. The merons come in flavours of charge  $\pm e/2$  and clockwise and anticlockwise vorticity [61, 62, 63, 37, 84, 75, 77, 85, 90, 87, 91, 92, 93, 94, 95, 96, 79]. The merons are nucleated by charge disorder. At any finite temperature, there is thermally activated motion of un-paired merons through the counterflow superfluid and this causes dissipation [90]. This can explain why the dissipation in the tunneling “supercurrent” branch of a quantum Hall bilayer appears similar to  $R_{xx}$  as they share the same origin. This effect possibly masks the Kosterlitz-Thouless transition expected for a 2D-superfluid and predicted for this state [97, 62, 98, 99, 100, 101]. Any amount of charge disorder may be sufficient to destroy the Kosterlitz-Thouless transition. So ideal superfluidity may be attainable only at zero temperature limit.

### 4.5.5 Effect of external resistors

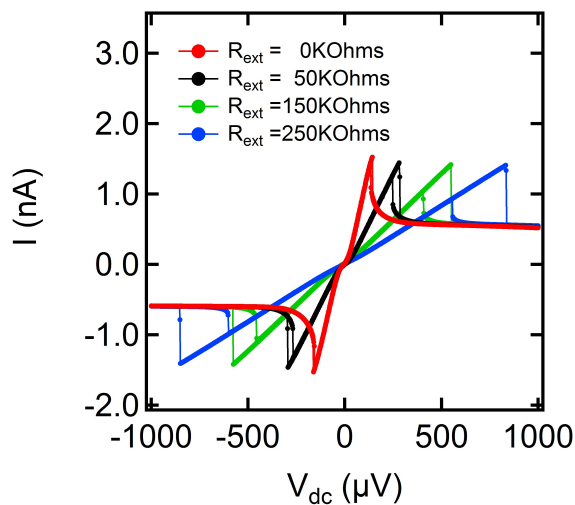


Figure 4.12: Plot of  $I$  vs  $V_{dc}$  on outer rim with different external resistors  $R_{ext}$  on each arm at  $T = 15$  mK,  $d/l = 1.5$ .

The effect of inserting an additional resistor  $R_{ext}$  in each arm makes the instability more pronounced. Increasing  $R_{ext}$  also increases the hysteresis in the tunneling  $I - V$  as seen in Fig. 4.12.

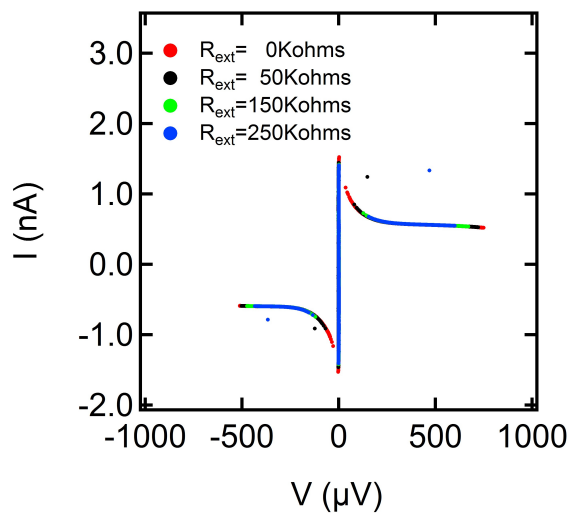


Figure 4.13: Plot of  $I$  vs  $V$  on outer rim with different external resistors  $R_{ext}$  on each arm at  $T = 15$  mK,  $d/l = 1.5$

Interestingly, all the tunneling traces for different  $R_{ext}$  values collapse onto each other when plotted as four terminal  $I - V$  as shown in Fig. 4.13. This observation is apparently simple. But it has profound implications in whether one can theoretically obtain such curves assuming a simple Josephson relation [3].

For a voltage biased Josephson junction in Fig. 4.14 (b),

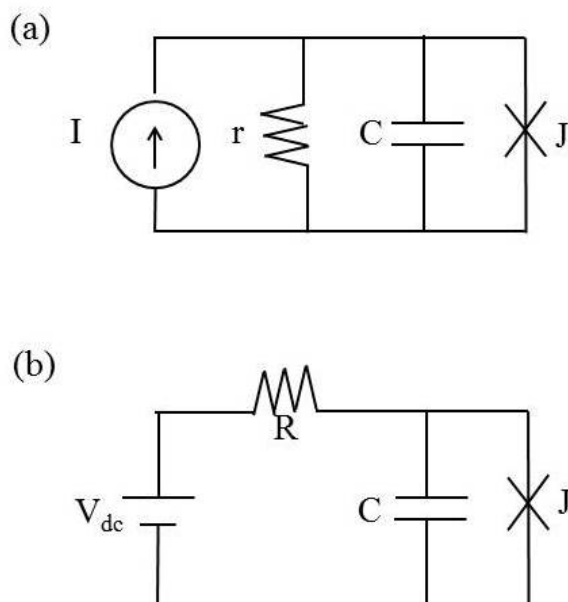


Figure 4.14: (a)  $RSJ$  Model for a current biased Josephson junction and (b) Circuit Model for a voltage biased Josephson junction.

$$I_J = I_c \sin \phi, \quad (4.14)$$

$$\frac{d\phi}{dt} = \frac{eV}{\hbar}, \quad (4.15)$$

$$V_{dc} = V + IR, \quad (4.16)$$

$$I_c \sin \phi + C \frac{dV}{dT} = I. \quad (4.17)$$

Substituting for  $V$  and combining the above equations we get,

$$\frac{\hbar C}{e} \frac{d^2 \phi}{dt^2} + \frac{\hbar}{eR} \frac{d\phi}{dt} + I_c \sin \phi = \frac{V_{dc}}{R}. \quad (4.18)$$

For an overdamped Josephson junction, we can neglect the capacitive contribution. This simplifies the above Eq. 4.18 as follows:

$$\frac{\hbar}{eR} \frac{d\phi}{dt} + I_c \sin \phi = \frac{V_{dc}}{R}. \quad (4.19)$$

For  $I < I_c$ , the phase is stationary. So the measured  $dc$  value of 4-terminal voltage  $V$  is

$$\bar{V} = 0. \quad (4.20)$$

For  $I > I_c$ ,

$$\frac{e}{\hbar} \bar{V} = \frac{2\pi}{T}, \quad (4.21)$$

$$T = \frac{\hbar}{eR} \int_0^{2\pi} \frac{d\phi}{\frac{V_{dc}}{R} - I_c \sin \phi}, \quad (4.22)$$

$$T = \frac{\hbar}{eR} \frac{2\pi}{\sqrt{(\frac{V_{dc}}{R})^2 - I_c^2}}. \quad (4.23)$$

This gives

$$\bar{V} = \sqrt{(\frac{V_{dc}}{R})^2 - I_c^2}, \quad (4.24)$$

$$I = \frac{\sqrt{\bar{V}^2 + (I_c R)^2} - \bar{V}}{R}. \quad (4.25)$$

The voltage biased model captures surprisingly well the shapes of the tunneling  $I-V$ .

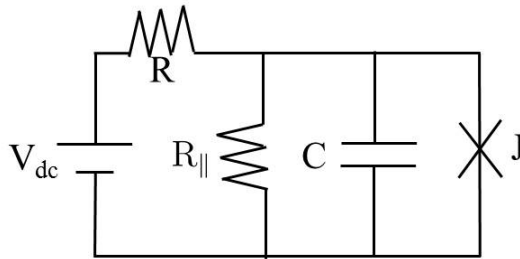


Figure 4.15: Circuit model for a voltage biased Josephson junction with a resistor  $R_{\parallel}$  in parallel to the Josephson junction.

A more realistic model must also take into account that there is incoherent tunneling processes happening in parallel to the Josephson-like tunneling [3]. This calls for a minor modification to the circuit in Fig. 4.14 (b) and is shown in Fig. 4.15. Taking into account the current through  $R_{\parallel}$  gives

$$I = \frac{\sqrt{\bar{V}^2 + (I_c R)^2} - \bar{V}}{R} + \frac{\bar{V}}{R_{\parallel}}. \quad (4.26)$$

This is modeled in Matlab to get a  $I$  vs  $\bar{V}$  curve.  $R = 70$  KOhms is the two terminal resistance in the “supercurrent” branch near  $I_c$  in Fig. 4.4 that is intrinsic to the sample. The incoherent tunneling resistance  $R_{\parallel}$  is treated as a free parameter and the blue curve in Fig. 4.16 is plotted for  $R/R_{\parallel} = 0.1$  and compared to the experimental data.

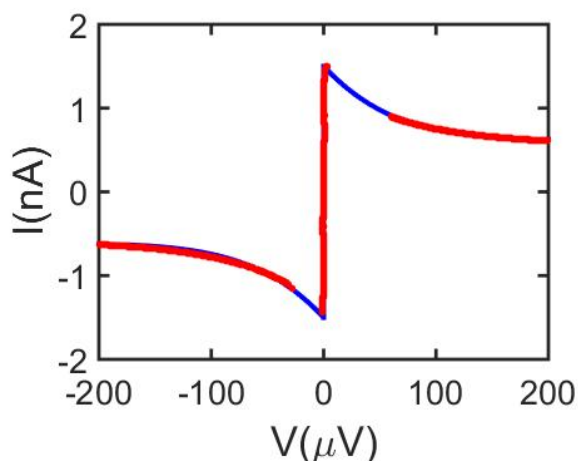


Figure 4.16: The red trace is experimental tunneling  $I - V$  in Fig. 4.5 and the blue curve is from model of a voltage biased Josephson junction shown in Fig. 4.15 with  $R = 70$  KOhms and  $R_{\parallel}$ (fit parameter) = 700 KOhms.

The good agreement between the model and experimental data indicates that the four terminal tunneling  $I - V$ s are consistent with the  $dc$  Josephson effect. However, a drawback in this model is that the four terminal  $I - V$  changes if the external resistors are added or subtracted from the circuit. This is inconsistent with our results that the intrinsic tunneling  $I - V$  is unaffected by addition of external resistors as in Fig.

4.13 and is not so well understood. Another puzzle is that even though our tunneling data bears remarkable resemblance to an overdamped Josephson junction, it is not at all obvious why it is in the overdamped regime. Eq. 4.18 can be rewritten as

$$\frac{1}{\omega_p^2} \frac{d^2\phi}{dt^2} + \frac{1}{Q\omega_p} \frac{d\phi}{dt} + \sin\phi = \frac{V_{dc}}{RI_c}. \quad (4.27)$$

where  $Q$  is the quality factor and  $\omega_p$  is the plasma resonance frequency given by

$$\omega_p = \sqrt{\frac{eI_C}{\hbar C}}, \quad (4.28)$$

$$Q = \omega_p RC = \sqrt{\frac{eI_C R^2 C}{\hbar}}. \quad (4.29)$$

The geometric capacitance between the two layers is  $C = 3.1$  nF where distance between the two layers  $d = 28$  nm, outer and inner diameter of Corbino device = 1.4 mm and 1.0 mm, respectively, and dielectric constant of GaAs =  $13 \epsilon_r$ . The total resistance  $R \approx 10^5$  Ohms and  $I_c = 1.5$  nA. This gives quality factor  $Q = 8200$ . This should make it a highly underdamped junction. Given the striking resemblance to overdamped Josephson junction, this must not be the whole story. We need a circuit model that can explain why the junction is overdamped and also incorporates dissipation.

### 4.5.6 Overdamped Josephson junction

The *RSJ* model of superconducting Josephson junctions does not account for dissipation in the “supercurrent” branch. However, it is well established that dissipation is present even in superconducting Josephson junctions [88]. Here an attempt is made to present an *RSJ*-type model for the bilayer tunnel junction that accounts for both parallel transport channel  $R_{||}$  due to quasiparticles in addition to Josephson-like tunneling and a small dissipative resistor  $r_s$  in series with the Josephson junction. The model is represented in Fig. 4.17. Analysis of this circuit gives:

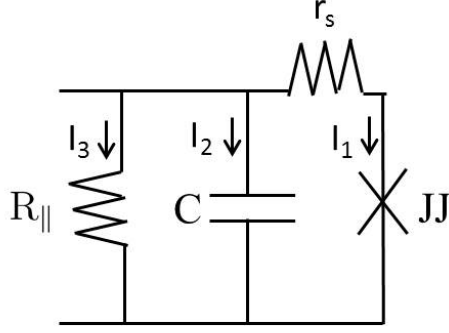


Figure 4.17: Equivalent circuit model for bilayer tunneling

$$I_1 = I_{JJ} = I_c \sin \phi, \quad (4.30)$$

$$\frac{d\phi}{dt} = \frac{eV}{\hbar}, \quad (4.31)$$

$$V_T = V + I_c \sin \phi r_s, \quad (4.32)$$

$$I_2 = \frac{V_T}{R_{\parallel}}, \quad (4.33)$$

$$I_3 = C \frac{dV_T}{dt}, \quad (4.34)$$

$$I = I_1 + I_2 + I_3 = I_c \sin \phi \left(1 + \frac{r_s}{R_{\parallel}}\right) + \left(\frac{\hbar}{eR_{\parallel}} + Cr_s I_c \cos \phi\right) \frac{d\phi}{dt} + \frac{C\hbar}{e} \frac{d^2\phi}{dt^2}. \quad (4.35)$$

Here  $V$  is the voltage across the Josephson junction and  $V_T$  is the measured 4-terminal voltage drop across the capacitor  $C$ . The model is able to explain the finite dissipation observed in the “supercurrent” branch. In the limit of no incoherent tunneling, i.e.,  $R_{\parallel} \rightarrow \infty$  the model is identical to that of Rossi, Nunez, and MacDonald [78] and becomes

$$I = I_c \sin \phi + Cr_s I_c \cos \phi \frac{d\phi}{dt} + \frac{C\hbar}{e} \frac{d^2\phi}{dt^2}, \quad (4.36)$$

$$\frac{I}{I_c} = \sin \phi + \frac{\cos \phi}{Q' \omega_p} \frac{d\phi}{dt} + \frac{1}{\omega_p^2} \frac{d^2\phi}{dt^2}. \quad (4.37)$$

Here  $Q'$  is the quality factor given by

$$Q' = \sqrt{\frac{\hbar}{eI_c C r_s^2}}. \quad (4.38)$$

For geometric capacitance  $C = 3.1$  nF, typical critical current  $I_c = 1.5$  nA and dissipation  $r_s \approx 100 \Omega$ ,  $Q' = 0.1$  and the device is overdamped. The critical damping of  $Q' = 1$  happens for  $r_s \approx 12 \Omega$ .

#### 4.5.7 Effective layer separation dependence of tunneling

Fig. 4.18 summarizes the temperature and effective layer separation dependence of the critical current  $I_c$  [49]. To analyze this data, first the lowest temperature critical current  $I_{c,max}$  is plotted versus  $d/l$  in Fig. 4.20. A linear dependence on  $d/l$  is observed. On renormalizing the curves in Fig. 4.18 by their lowest temperature value  $I_{c,max}$ , one observes reasonably good data collapse. It is remarkable that this happens without any normalization of temperature unlike the case of Josephson junctions, where a similar effect is observed but only if temperature is normalized by superconducting transition temperature  $T_c$  as explained by Ambegaokar and Baratoff [102]. Estimate

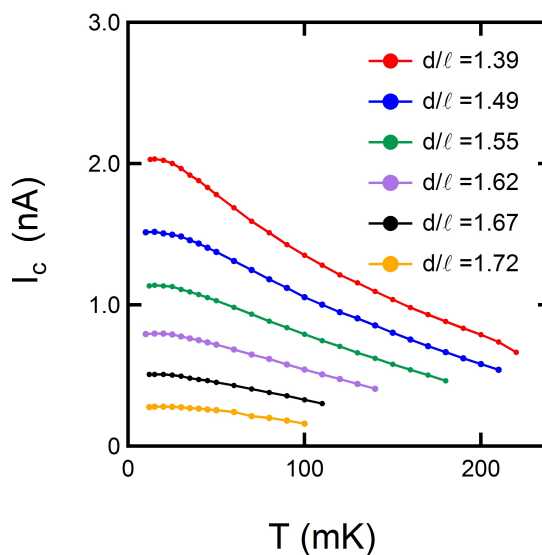


Figure 4.18: Plot of  $I_c$  vs  $T$  at different  $d/l$ .

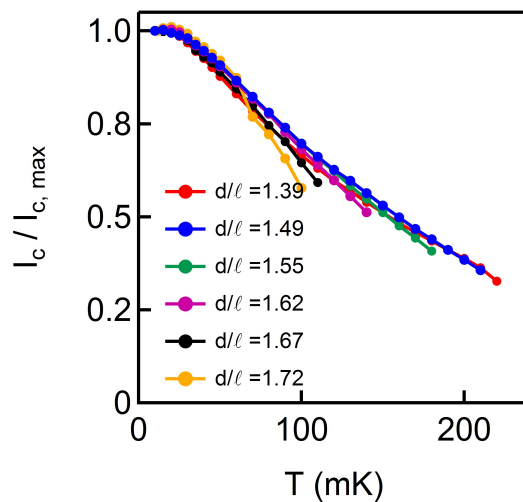


Figure 4.19: Plot of  $I_c/I_{c,max}$  vs  $T$  at different  $d/l$ .

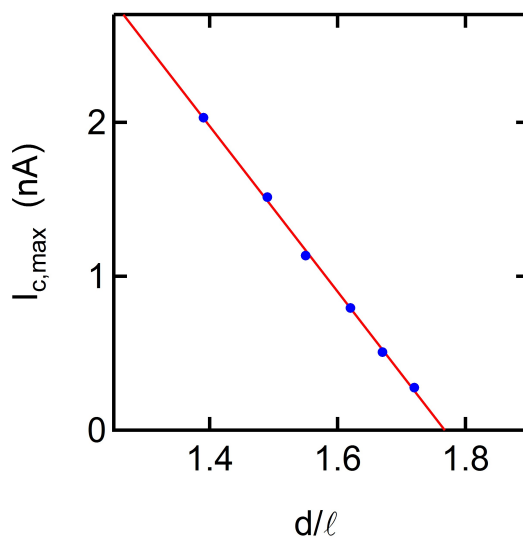


Figure 4.20: Plot of  $I_{c,max}$  vs  $d/l$ .

of the critical current density  $J_c$  in accordance to the Josephson effect derived in Eq. 4.12 is as follows:

$$J_c = \frac{e\Delta_{SAS}}{4\pi l^2 \hbar}. \quad (4.39)$$

$\Delta_{SAS} = 10^{-9}$  eV,  $l = 19$  nm gives  $I_c \approx 400$   $\mu$ A which is  $2.7 \times 10^5$  times larger than the measured values of  $\approx 1.5$  nA. This huge reduction in  $I_c$  is largely attributed to

effects of disorder. Further, various experiments over the past decade suggest that  $I_c \propto \Delta_{SAS}^2$  and not  $\Delta_{SAS}$ . This also is considered to be an effect of disorder.

The coherence network model of a disordered excitonic superfluid considers that puddles of compressible electron liquids are separated by narrow channels of incompressible superfluid. Hence the actual superfluid fraction is reduced resulting in smaller critical currents and deviations from ideal Josephson effect. The cause of the puddles is most likely due to the presence of dopant layer  $\approx 200$  nm away on both side of the quantum wells.

Hyart et al. and Sodemann et al. propose that the exciton superfluid has a disorder correlation length of  $\xi$ . Disorder results in domains of  $\approx n\xi^2/2$  of correlated fluid. This would renormalize the bare  $\Delta_{SAS}$  as follows [79, 3]:

$$\Delta_{SAS} \rightarrow \frac{n\xi^2}{2} \frac{\Delta_{SAS}^2}{\rho_S}. \quad (4.40)$$

$\Delta_{SAS} = 10^{-9}$  eV,  $n\xi^2 \approx 10$ , and  $\rho_s = 10^{-4}$  eV [3]. This could explain a  $10^4$  reduction in  $I_c$ . Several theoretical works have studied the effect of disorder in renormalizing the  $I_c$  [85, 93, 95, 79, 3].

#### 4.5.8 Contact independence

In Fig. 4.21, the source and drain contacts are in different contact configurations including both on the outer rim and both on the inner rim. No matter which pair of source drain contacts are used, as long as they are placed along the same rim,  $I_c$  vs  $T$  is almost identical. This observation is consistent with two possibilities of tunneling current distribution pattern. Either all the tunneling is happening only at hot spots close to the source and drain or tunneling is uniformly distributed throughout the bulk of the sample. Both these scenarios are consistent with contact independence of tunneling critical current. This observation does eliminate the tunneling happening along the edge on which the source drain contacts are placed. In this case the critical current would scale with the perimeter, which would be very different for the inner and outer rims.

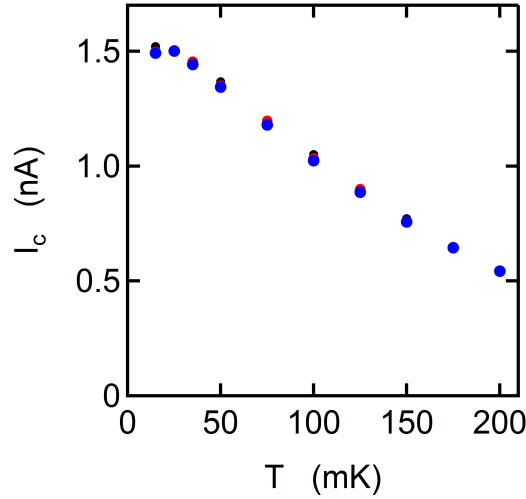


Figure 4.21: Plot of  $I_c$  vs  $T$  at different source drain configuration for  $d/l = 1.5$ .

#### 4.5.9 Multiple source drain pairs

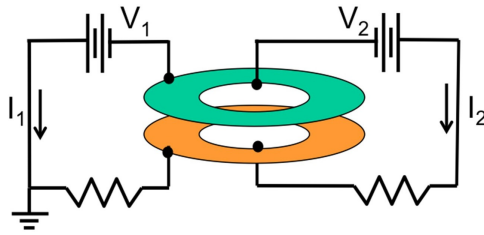


Figure 4.22: Measurement setup. The voltages  $V_1$  is held fixed. Voltage  $V_2$  is swept.  $I_1$  and  $I_2$  are measured.

Huang et al. injected tunneling currents simultaneously on the outer rim  $I_1$  and the inner rim  $I_2$  of a Corbino device and observed that the maximum critical current observed at one edge can be controlled by passing a fixed tunneling current on the other edge [103]. The experiment was reproduced in this Corbino device.

The bias  $V_1$  on the outer rim is held fixed. This allows one to inject a fixed tunneling current  $I_1$  on the outer rim. The two terminal tunneling current  $I_2$  on the inner rim is recorded by sweeping  $V_2$ . In Fig. 4.23,  $I_2$  is plotted vs  $I_1$ . For  $I_1 = 0$ ,  $I_2 = \pm 1.5$  nA. On injecting  $I_1 = 1$  nA,  $I_{2,c}$  decreases by exactly 1 nA. As shown in Fig. 4.24, this is verified to hold for several other values of  $I_1$ . This implies the system

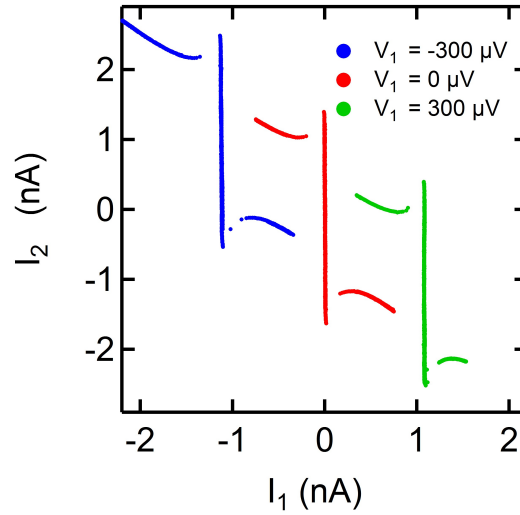


Figure 4.23: Tunneling currents  $I_2$  vs  $I_1$  obtained by varying  $V_2$  and holding  $V_1$  fixed at  $-300 \mu\text{V}$ ,  $0 \mu\text{V}$ ,  $300 \mu\text{V}$  for the blue, red, and green traces, respectively.

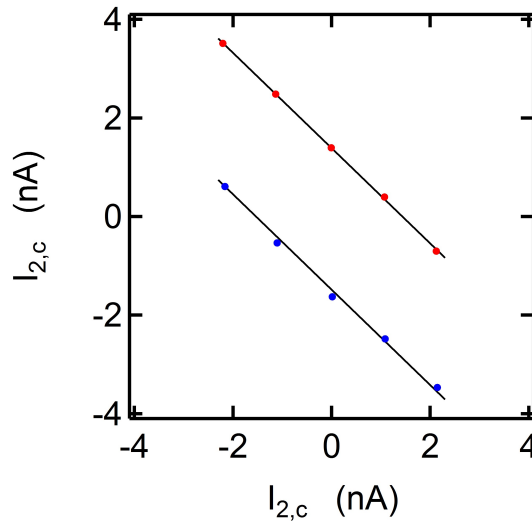


Figure 4.24: Critical current values of  $I_2$  plotted vs fixed values of  $I_1$ .

exhibits a single critical current which is determined by  $I_1 + I_2$ .

In view of this result, it is clear that tunneling is a bulk phenomenon happening throughout the annular ring. It rules out the scenario of tunneling happening in hot spots close to source drain contacts because the tunneling current on the inner rim would be independent of tunneling current on the outer rim. This conclusion is

consistent with other experiments that showed the tunneling critical current and the tunneling conductance peak height to scales with area [80, 42].

Even though tunneling scaling with area seems intuitive, it turns out that it is not expected in a disorder free superfluid exhibiting Josephson effect. The time-independent solution of a Josephson junction obeys the sine-Gordon equation [75, 3, 104].

$$\lambda_J^2 \Delta^2 \phi - \sin \phi = 0, \quad (4.41)$$

$\lambda_J$  is the Josephson penetration length given by

$$\lambda_J = 2l \sqrt{\frac{\pi \rho_s}{\Delta_{SAS}}}, \quad (4.42)$$

and estimated  $\approx$  few  $\mu\text{m}$ . In the limit of small  $\phi$ , the phase decays off exponentially within a wavelength  $\lambda_J$ . So the tunneling is expected to be spatially non-uniform and not to depend on the dimensions of the sample, which are 1.4 mm on the outer diameter and 1 mm on the inner diameter. However, the experimental results are unequivocal in terms of tunneling happening uniformly throughout the tunnel junction [80, 39, 42, 49]. Several theoretical works have tried to understand the area scaling of tunneling [95, 79, 3]. The same theoretical model also overestimated  $I_c$  by  $> 10^5$  times. If we use the disorder renormalized  $\Delta_{SAS}$ ,

$$\lambda_J \rightarrow 4\pi l^2 \frac{\rho_s}{\xi \Delta_{SAS}}. \quad (4.43)$$

This would estimate  $\lambda_J$  about 2 orders of magnitude larger. Even though it would still not explain the observed area scaling of tunneling, it does emphasize the crucial role that disorder plays in modifying the nature of tunneling at  $\nu_T = 1$ .

Eastham et al. have tried to explain why the critical current scales with area [93, 95]. Their model is analogous to the coherent network model by Fertig et al. discussed earlier [77, 85, 87]. The reason for this charge puddles is the presence of the dopant layer which is imperfectly screened. For this model of disordered superfluid, the tunneling currents are found to decay linearly with distance from the contacts

and not exponentially. As more tunneling current is injected into the sample, the tunneling current penetrates further into the sample in order to keep the superfluid phase static. Finally, as the entire sample is penetrated by the tunneling current, it hits the critical current value  $I_c$  and beyond that, no static solution can be found. This results in a finite voltage drop across the junction. This picture gives an intuitive understanding of the area scaling of  $I_c$ .

## 4.6 Conclusion

The tunneling in quantum Hall bilayers at  $\nu_T = 1$  has been studied extensively. The dependence of normalized critical current on  $T$  shows an unexpected scaling behavior that is independent of effective layer separation  $d/l$ . The resistance of the “super-current” branch shows a roughly activated behavior and remains finite. Reasonable agreement is found between the experimental four terminal tunneling  $I - V$  and model of a voltage biased Josephson junction. Observation of an *ac* Josephson-like [69, 37, 21, 3] phenomenon would put the comparison to the *dc* Josephson effect on a more firm footing.

## Chapter 5

# Coulomb drag in Corbino geometry at $\nu_T = 1$

Coulomb drag is a transport probe where current is driven in one conductor and a voltage develops in another conductor in close proximity [105, 106, 107]. This drag voltage can also be measured as a drag current if the two voltage ends are connected through a shunt resistor. Coulomb drag measurements are effective in probing Coulomb correlations between conductors. It gives a measure of electron-electron momentum transfer rates. It has been employed to study Luttinger liquid physics in 1D-1D systems [108, 109, 110, 111, 112, 113, 114, 115, 116] and in 2D-2D systems like electron-electron bilayer [14, 117, 118, 119, 120, 15, 38] as well as electron-hole bilayers [121, 122, 123]. In the double quantum wells, it has proven to be an important probe in unraveling the exciton condensate nature of the  $\nu_T = 1$  state. Kellogg et al. [16] discovered Hall drag quantized at  $h/e^2$  supporting the exciton condensate picture. In this chapter, we present “perfect” Coulomb drag at  $\nu_T = 1$  where an electron current driven in one layer generates a hole current in an adjacent layer separated by an insulator. The drag and drive currents are equal in magnitude and opposite in sign at the lowest temperature and effective layer separation .

### 5.1 Zero magnetic field Coulomb drag

One of the prominent Coulomb drag measurements in GaAs/AlGaAs double quantum wells was by Gramila et al. [14, 124, 125, 126]. The two GaAs quantum wells

were separated by insulating AlGaAs barrier. The measurements were done in zero magnetic field. A constant low frequency *ac* current was applied on the drive layer. Due to momentum transfer mediated by long range Coulomb scattering between carriers in the two quantum wells, electrons get dragged in the passive layer [14]. The sign of the drag voltage is opposite of the voltage drop in the drive layer for electron-electron bilayers as it nullifies the drag current generated by virtue of momentum transfer [14]. The drag resistance is deduced as the ratio of the drag voltage to the drive current. From the drag resistivity, the electron-electron scattering lifetime  $\tau_D$  can be calculated. For two identical quantum wells, the drag resistivity  $R_D$  is given by

$$\frac{1}{R_D} = \frac{ne^2\tau_D}{m^*}. \quad (5.1)$$

Here,  $n$  is the electron density in the drive well and  $m^*$  is the effective electron mass. In Fig. 5.1, the temperature dependence of the drag resistivity  $R_D$  as well

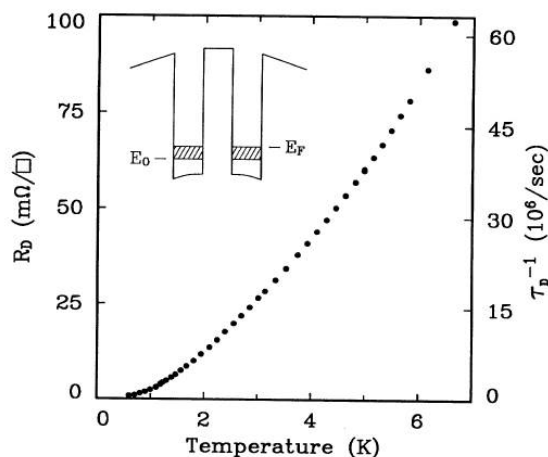


Figure 5.1: Temperature dependence of drag resistivity  $R_D$  vs  $T$ . Temperature dependence is also plotted for the electron-electron scattering lifetime. Inset: A double quantum well structure for which the drag measurements were performed. Reproduced from Gramila et al. [14]

as the electron-electron scattering lifetime  $\tau_D^{-1}$  is plotted. According to Fermi-liquid theory, the temperature dependence of momentum transfer lifetime  $\tau_D^{-1}$  should be  $T^2$ . This is because the electron-electron scattering process between two Fermi liquids is

confined to the Fermi surfaces and the phase space is  $T^2$ , considering each Fermi surface is thermally broadened by  $K_B T$ . This  $T^2$  dependence only applies to the low temperature limit. The observed  $\tau_D^{-1}$  had the correct magnitude as predicted by Boltzmann transport theory. However, deviations from  $T^2$  dependence were also observed. Jauho and Smith [117] showed that on numerically evaluating  $\tau_D^{-1}$  for higher temperatures, they could qualitatively explain the temperature dependence solely based on Coulomb drag mechanism. Contributions from other momentum transfer mechanisms due to exchange of phonons have also been considered [125, 127, 128, 129].

The sheet resistivity is  $\approx 10 \text{ } \Omega/\square$ . This means that at temperatures  $< 1 \text{ K}$ , the drag resistivity  $R_D$  is less than 1000 times the sheet resistivity. Thus the zero magnetic field Coulomb drag is a very subtle effect, requiring careful detection.

## 5.2 Coulomb drag at $\nu_T = 1/2 + 1/2$

The Coulomb drag in double layers was then explored by Lilly et al. [15] when each layer is in  $\nu_T = 1/2$  compressible Fermi liquid state. In the presence of a strong magnetic field, the granularity of the electrons is enhanced. This manifests as an enhanced Coulomb drag that is larger than the zero magnetic field case by  $\approx 1000$  times [15]. The sign of the drag voltage at higher temperatures was consistent with momentum transfer to electrons in the drag layer by scattering with electrons in the drive layer. Interestingly, it was observed that in the zero temperature limit, the drag resistivity  $\rho_D$  did not vanish in accordance with the  $T^2$  dependence as shown in Fig. 5.2 for drive current  $I = 1.5 \text{ nA}$ . In contrast for  $I = 7.5 \text{ nA}$ , the joule heating of the electron gas did not allow exploration of the zero temperature limit. Lilly et al. [15] reported that the residual drag  $\rho_D$  at the lowest temperatures could even be of opposite sign inconsistent with momentum-transfer drag. This was the initial evidence for a different drag mechanism than momentum transfer between electrons in the two layers. In some regions in the sample, possibly  $\nu_T = 1/2 + 1/2 \rightarrow \nu_T = 1$  and there was pairing of electrons and holes. The sign of this lowest temperature drag can be understood as driven electrons in one layer dragging along holes in the

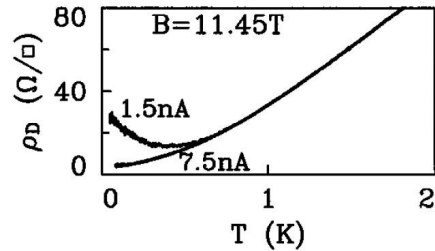


Figure 5.2: Temperature dependence of drag at  $\nu_T = 1/2 + 1/2$  for  $I = 7.5$  nA and  $I = 1.5$  nA. Figure is adopted from Lilly et al. [15].

opposite layer. The residual drag became much more prominent in later drag studies deep inside the  $\nu_T = 1$  quantum Hall phase.

### 5.3 Coulomb drag at $\nu_T = 1$ in Hall bar geometry

Drag was investigated by Kellogg et al. [16] in a Hall configuration where a low frequency *ac* current was injected in one layer and the voltage was measured transverse to the current direction in the other layer. As the effective layer separation was lowered by reducing the density equally in each layer, an accurately quantized Hall plateau at  $h/e^2$  appeared in the layer with no current [16]. This assertion of there being no current in the drag layer is possible when tunneling is negligible. The quantized Hall drag was robust to imposing large interlayer voltage as well as application of large in-plane magnetic field, both of which are known to dramatically suppress tunneling. This Hall drag plateau is evidence for strong interlayer Coulomb correlations being present in the  $\nu_T = 1$  state. An intuitive picture to explain the Hall drag resistance quantization at  $h/e^2$  is that the injected drive current  $I$  divides equally in each layer  $I/2$  and the measured Hall drag voltage is same as the conventional Hall voltage at  $\nu_T = 1$  state [16]. However, to satisfy the boundary conditions, an anti-parallel current  $I/2$  mediated by charge neutral excitons flows to make the current in the drag layer zero [16]. This being a superfluid-like current does not contribute to Hall voltage [16].

However, since the measurements were done in a Hall bar geometry, it cannot

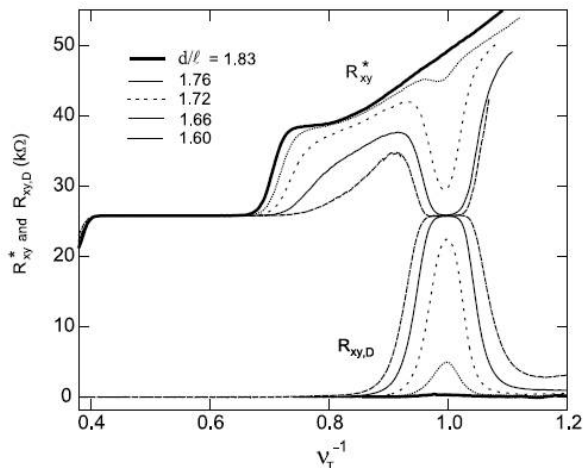


Figure 5.3: Evolution of Hall drag for  $d/l = 1.60, 1.66, 1.72, 1.76,$  and  $1.83,$  respectively.  $R_{xy}^*$  and  $R_{xy,D}$  are the Hall resistance of the current carrying layer and the drag layer, respectively. Results are due to Kellogg et al. [16].

distinguish exciton transport as an edge or a bulk phenomenon. Subsequent experiments by Tiemann et al. [39, 40, 41, 43] and Finck et al. [17, 6] studied the Corbino geometry precisely to answer these questions. The Corbino Coulomb drag experiment [130] presented in this chapter was also motivated to demonstrate “Perfect” Coulomb drag as a consequence of bulk transport of excitons.

## 5.4 Voltage drag in Corbino geometry

Coulomb drag measurements by Tiemann et al. were done in a Corbino device similar to the one described in section 4.1 by imposing a bias voltage across the inner and outer rim of the lower layer while simultaneously measuring the four terminal voltage across the lower layer and the upper layer [40]. The drag voltage was found to be negligible for all values of magnetic field except when the  $\nu_T = 1$  state was established. Here, the measured drag voltage was found to equal the measured drive voltage [40]. The sign of the drag is inconsistent with momentum transfer drag. This is because in the zero-magnetic field drag measurements of Gramilla et al. [14, 124], an electron in the passive layer gets weakly dragged by another electron in the active layer through momentum exchange, whereas in the exciton condensate phase, a tightly bound hole

in the passive layer gets dragged by an electron in the active layer. It gets deposited due to the boundary conditions, thereby giving rise to the drag voltage. The equality of the drag and drive voltage is consistent with exciton superfluidity. The opposite sign is due to holes rather than electrons being dragged. The equality of drag and drive voltage is consistent with excitonic superfluidity. However, at the lowest temperatures where the quasi-particle transport is suppressed by the quantum Hall gap, no bulk exciton current can flow as the top layer is open circuited.

## 5.5 Corbino Counterflow at $\nu_T = 1$

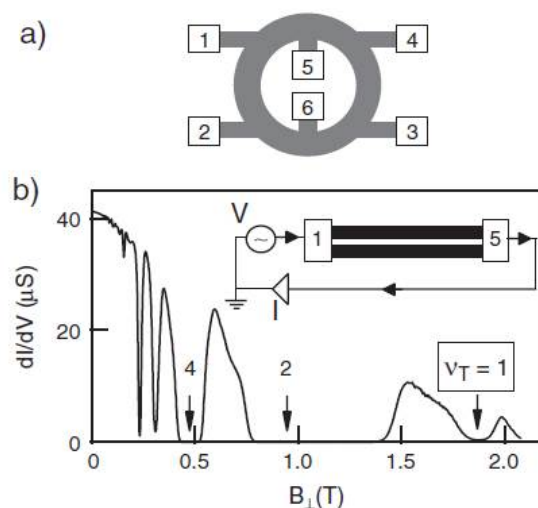


Figure 5.4: (a) Corbino device geometry (b) Plot of Corbino conductance at zero bias voltage with B-field sweep at  $d/l = 1.5$  for source and drain voltages on opposite rims. Sample is tilted to magnetic field direction by 28 degrees. Data is due to Finck et al. [17].

Finck et al. investigated whether bulk exciton currents could propagate in the  $\nu_T = 1$  state. The measurements were done in the Corbino device shown in Fig. 5.4 and also described in detail in section 4.1. Fig 5.4 shows the two terminal Corbino conductance  $\sigma_{xx}^{\parallel}$  at  $T = 25$  mK. The ac drive is applied to both the layers in parallel and the perpendicular magnetic field  $B_{\perp}$  is swept. The bulk of the Corbino device is an insulator at  $\nu_T = 1$  and charge transport mediated by quasi-particles is suppressed

by the quantum Hall gap. The two layers were then configured for bulk counterflow

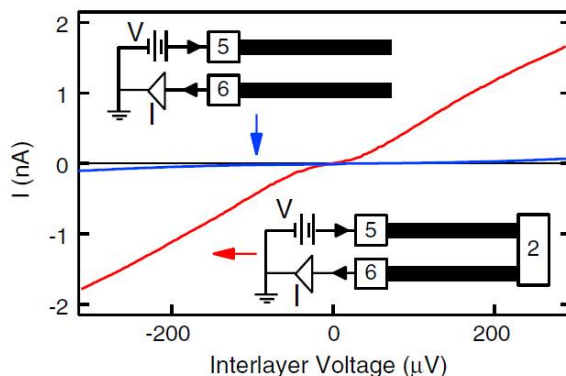


Figure 5.5: Red trace is counterflow  $I - V$  in a Corbino device at  $\nu_T = 1$  at  $T = 25$  mK,  $B_{\perp} = 1.88$  T, and  $\theta = 28$  degrees. Blue trace is tunneling  $I - V$ . Contacts 5 and 6 are on the inner rim and 2 is on the outer rim of the Corbino device. Reproduced from Finck et al. [17].

by Finck et al. [17]. This is depicted schematically in Fig. 5.5 at the right hand bottom corner. This is achieved by shorting the ohmic 2 to contact both layers. This results in the red trace in Fig. 5.5 and current is found to flow easily in the counterflow configuration in contrast to parallel configuration. Since the  $\nu_T = 1$  state

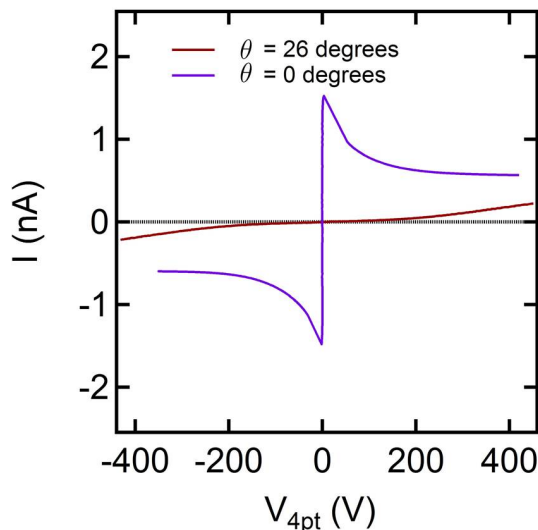


Figure 5.6: Tunneling  $I - V$  is measured for  $d/l = 1.5$  and  $T = 20$  mK. The purple trace is  $\theta = 0$  degrees and the brown trace is  $\theta = 26$  degrees.

exhibits a *dc*-Josephson-like tunneling as discussed in section 3.2.2 [2], the counterflow cannot be distinguished from a tunneling current. To eliminate this possibility, Finck et al. tilted the sample in order to apply an in-plane magnetic field  $B_{\parallel} \approx 1$  T. This enormously suppressed the zero bias tunneling anomaly as shown in Fig. 5.6. In section 3.2.3, we discussed in greater detail the evolution of the zero bias anomaly with in-plane magnetic field as shown by Spielman et al. [9].

A comparison of the tunneling contribution to counterflow is shown by the blue trace in Fig. 5.5. The fascinating nature of interlayer correlations present in the  $\nu_T =$

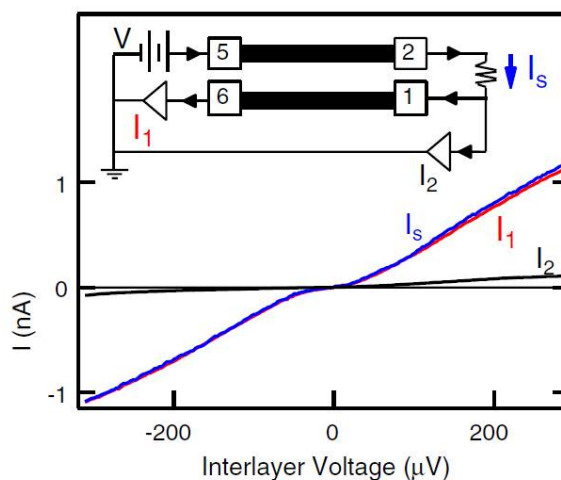


Figure 5.7:  $I_s$  is the blue trace and is the current flowing through the shunt resistor.  $I_1$  is the current flowing through the bottom layer and marked in red.  $I_2$  is the current flowing through the short. Data is taken at  $B_{\perp} = 1.88$  T, and  $\theta = 28$  degrees. This data demonstrates bulk exciton flow. Reproduced from Finck et al. [17].

1 exciton condensate was further elucidated by the fact that when in the counterflow configuration, the bottom layer was short circuited, as shown in Fig. 5.7, little current returned through the short, producing the black trace. This proved that the bulk counterflow currents were mediated by interlayer excitons.

## 5.6 Su-MacDonald Theory

Su and MacDonald [18] observed that contrary to previous ideas, an exciton supercurrent cannot be launched by applying a voltage bias between the two layers at one end

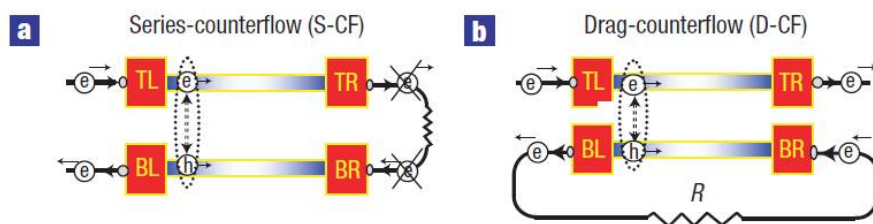


Figure 5.8: Schematic depiction of series counterflow and drag counterflow. According to Su-Macdonald theory, only drag counterflow sustains exciton superflow.  $TL$  and  $BL$  refer to the top and bottom contacts, respectively, of the condensate on one rim whereas  $TR$  and  $BR$  refer to the top and bottom contacts, respectively, of the condensate on the other rim of a Corbino device. Reproduced with permission from Su et al. [18].

and a shunt resistor between the two layers at the other end as shown in Fig. 5.8 (a). The reason is in the underlying mechanism for exciton flow. In the series counterflow of Fig. 5.8 (a) the applied bias would cause a hole to launch an exciton at  $TL$  and  $BL$  in the condensate and a hole to return to the applied bias via Andreev reflection. This launched exciton crosses the bulk and needs to get absorbed by inverse Andreev reflection at the other end. But here is where the problem lies. The hole generated at  $TR$  needs to get absorbed at  $BR$  instantaneously, which would violate causality. This was also concluded by Fil and Shevchenko [131]. Su and MacDonald proposed that if instead one sets up a current drag configuration as shown in Fig. 5.8 (b), bulk exciton supercurrents can flow.

## 5.7 Corbino Coulomb drag at $\nu_T = 1$

The measurement circuit for a Corbino current drag configuration as proposed by Su and Macdonald [18] is shown in Fig. 5.9. Current is injected into the inner rim of the top layer and extracted out of the outer rim of the same layer. The bottom layer is part of a closed loop. The drive current  $I_1$  and drag current  $I_2$  are measured as voltage drops across two identical shunt resistors. The direction of drive and drag currents is denoted by the arrows in Fig 5.9. The sample is tilted to  $\theta = 26$

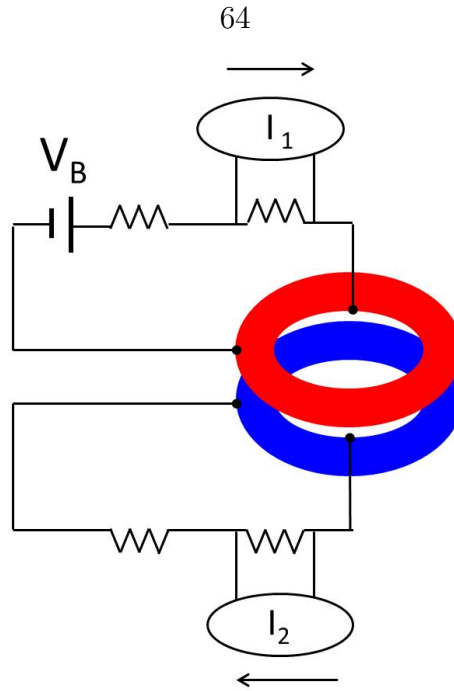


Figure 5.9: Circuit for Coulomb drag measurement for a quantum Hall bilayer.

degrees in order to apply  $B_{\parallel} \approx 1$  T to make the interlayer tunneling negligible and all the measurements are performed in this tilted configuration. Other than the shunt resistor used to measure current, the drive and drag circuits each have additional resistances due to arms contacting the  $\nu_T = 1$  state, additional external resistors and also  $h/e^2$  resistance due to injecting currents in and out of a quantum Hall state at  $\nu_T = 1$ . Using global top and back gates, the effective layer separation can be tuned from  $d/l = 2.3$  to  $d/l = 1.5$ . The two layers are gated to maintain equal density in each layer.

### 5.7.1 Magnetic field dependence of Coulomb drag

In Fig. 5.10, the perpendicular magnetic field  $B_{\perp}$  is swept and the Corbino drag conductance  $\frac{dI_2}{dV_B}$  is measured at various temperatures  $T$ . The effective layer separation is  $d/l = 1.5$  where the bilayer quantum Hall state at  $\nu_T = 1$  is well established. The drag current is recorded. It is found to exhibit a peak that coincides with the  $\nu_T = 1$  state. As the temperature is increased, the drag current peak gets reduced in magnitude. This decrease in Coulomb drag conductance will be revisited in subsection

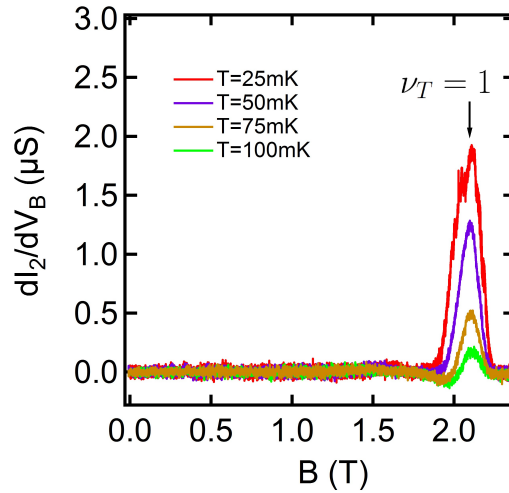


Figure 5.10: Temperature dependence of Coulomb drag conductance  $\frac{dI_2}{dV_B}$  with magnetic field sweep. Tilt angle  $\theta = 26$  degrees, and  $d/l = 1.5$ .

5.7.3 and again in section 5.9 for a quantitative understanding.

### 5.7.2 “Perfect” Coulomb drag at $\nu_T = 1$

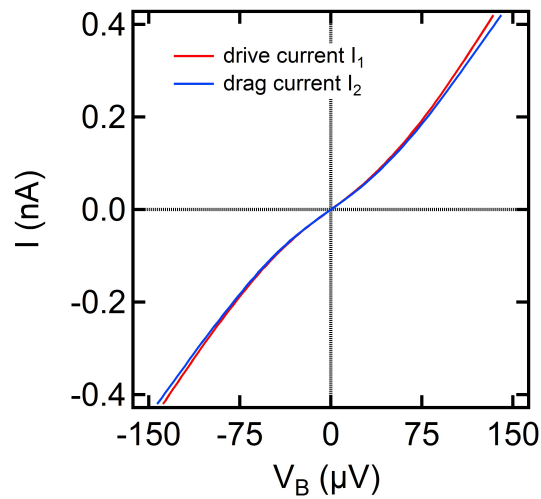


Figure 5.11: The red and blue traces show the measured drive and drag currents, respectively.  $T = 25$  mK,  $d/l = 1.5$ , and  $\theta = 26$  degrees.

In order to study the origin of the peak at  $\nu_T = 1$ , the magnetic field is held fixed and the applied bias is swept while recording the drive and drag currents simulta-

neously. At low biases, the drag to drive current ratio is close to unity (as high as 0.97) at the lowest  $T$  and effective layer separation  $d/l$ . The drive and drag currents are always oppositely directed. The currents exhibit a non-ohmic behavior. This is attributed to the arm resistances which also have resistance that is function of voltage  $V_B$  [6].

The underlying mechanism is that a charge from the applied bias impinges upon the exciton condensate at  $\nu_T = 1$  causing an interlayer exciton to cross the bulk of the Corbino device. Due to Andreev reflection, a charge flows in the drag circuit. At the other end, the reverse recombination process takes place. The exciton annihilates with the absorption of charge in the bottom drag circuit and leaves behind a charge in the top drive circuit which gets collected at the applied bias.

### 5.7.3 Breakdown of “perfect” Coulomb drag

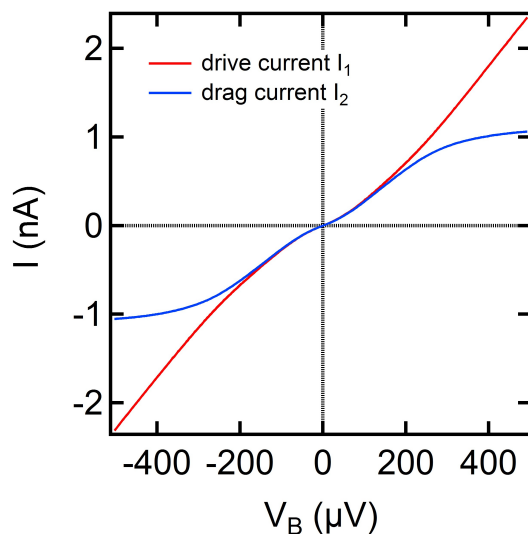


Figure 5.12: The red and blue traces show the measured drive and drag currents, respectively.  $T = 25$  mK, and  $\theta = 26$  degrees.

At large applied bias  $V_B$ , the drive current  $I_1$  and drag current  $I_2$  separate out and the ratio of drag current to drive current falls below unity. This signifies that the drive and drag currents are no longer mediated purely by excitons. Parallel currents

can flow at large bias voltages mediated by charged quasiparticles. This signifies a breakdown of the quantum Hall state with bias and finite  $\sigma_{xx}$ . This is similar to the two fluid model in superfluidity [132]. The dissipative normal fluid and the dissipationless superfluid coexists.

#### 5.7.4 Temperature and effective layer dependence of Coulomb drag

Upon increasing the temperature  $T$  and effective layer separation  $d/l$ , the drag to drive ratio  $I_2/I_1$  falls below unity. At the lowest biases,  $I_2/I_1$  goes from 0.97 to nearly 0 as the temperature is raised from 15 mK to 100 mK as shown in Fig. 5.13 (a). Similarly  $I_2/I_1$  goes from 0.97 to nearly 0 as the effective layer separation  $d/l$  is increased from 1.50 to 2.34 as shown in Fig. 5.13 (b). This we attribute to an increase in quasiparticle conductance  $\sigma_{xx}$ . This results in simultaneous parallel transport through the bulk of the Corbino in addition to counterflow transport mediated by charge neutral excitons.

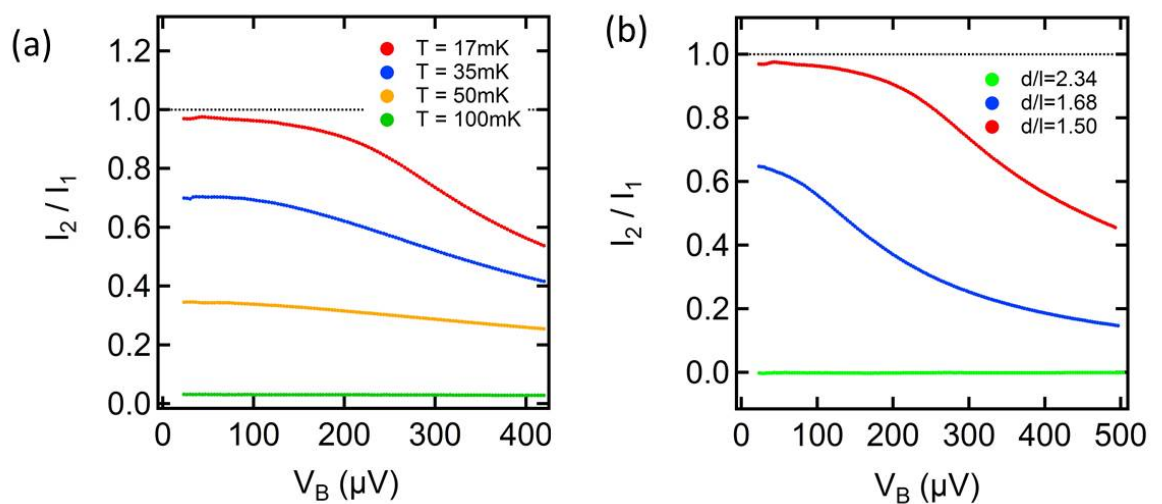


Figure 5.13: (a) Temperature dependence of drag current to drive current ratio for  $d/l = 1.5$ , and  $\theta = 26$  degrees. (b) Effective layer separation  $d/l$  dependence of drag current to drive current ratio for  $T = 17$  mK, and  $\theta = 26$  degrees.

## 5.8 Modeling Coulomb drag at $\nu_T = 1$

In accordance with Su and MacDonald theory, the Coulomb drag data is captured by a simple 1D-circuit model using Kirchoff's law and the assumption is made that counterflow transport mediated by charge neutral excitons is dissipationless. Fig. 5.14 is a circuit diagram of the Coulomb drag circuit. Indices 1 and 2 refer to the drive and the drag circuits, respectively. Assumption of exciton superfluidity gives:

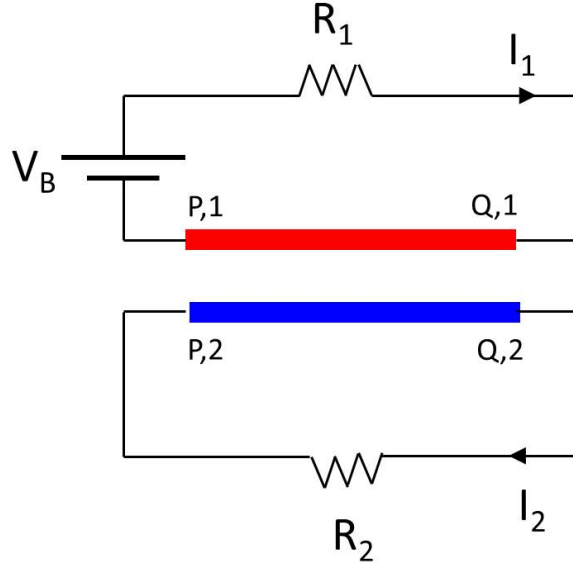


Figure 5.14: A 1D-model in the current drag configuration.

$$V_{P,1} - V_{Q,1} = V_{P,2} - V_{Q,2} = V_{PQ}, \quad (5.2)$$

$$V_{PQ} = V_B - I_1 R_1 = I_2 R_2. \quad (5.3)$$

Here  $R_1$  and  $R_2$  includes all resistances external to the condensate in the drive and drag circuits, respectively. These include the standard resistors added to the circuit, the ohmic resistances, the arm resistance leading to the 2DEG and the quantum Hall resistance of  $h/e^2$ . Next let us assume

$$R_1 = R_2 = R_0, \quad (5.4)$$

which simplifies to

$$V_{PQ} = V_B - I_1 R_0 = I_2 R_0, \quad (5.5)$$

$$V_{PQ} = V_B - I_1 R_0 = I_2 R_0, \quad (5.6)$$

$$I_1 + I_2 = V_B / R_0. \quad (5.7)$$

$R_0$  is, however, a function of the applied bias and the functional form can be determined based on four terminal tunneling measurements.

$$I_1 - I_2 = V_{PQ} \sigma_{xx}(V_{PQ}), \quad (5.8)$$

where the exact functional form of  $\sigma_{xx}(V_{PQ})$  can be determined based on 4-terminal Corbino parallel conductance measurements. Each of these measurements will be discussed in detail later. Thus,  $I_1$  and  $I_2$  can be uniquely determined. The drive current  $I_1$  is given by

$$I_1 = \frac{1}{2} \left( \frac{V_B}{R_0} + V_{PQ} \sigma_{xx}(V_{PQ}) \right), \quad (5.9)$$

and the drag current  $I_2$  is given by

$$I_2 = \frac{1}{2} \left( \frac{V_B}{R_0} - V_{PQ} \sigma_{xx}(V_{PQ}) \right). \quad (5.10)$$

### 5.8.1 Voltage drag

Let us also analyze the voltage drag circuit shown in Fig. 5.15 using the same line of argument. In this case, the bottom layer is open circuited and the drag voltage is measured across its two ends. The superfluidity condition would impose

$$V_{S,1} - V_{T,1} = V_{S,2} - V_{T,2} = V_{S,T}. \quad (5.11)$$

The validity of this assumption was tested and verified by Tiemann et al. in their Corbino voltage drag experiment [40]. For a closed loop,

$$V_B = IR + V_{ST}. \quad (5.12)$$

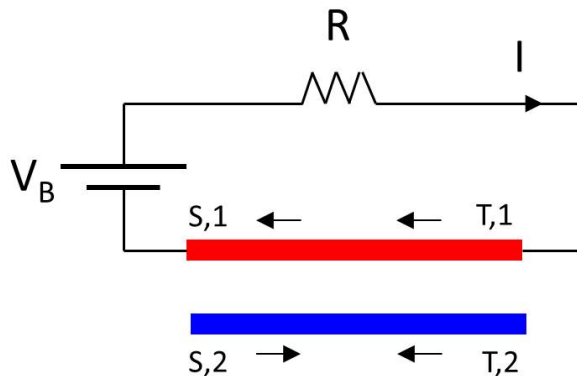


Figure 5.15: A 1D-model in the voltage drag configuration.

Now the boundary conditions of the problem imply  $I/2$  parallel current in the two layers and  $I/2$  anti-parallel current in the two layers as shown in Fig. 5.15. By definition of  $\sigma_{xx}^{\parallel}$ ,

$$\sigma_{xx}^{\parallel}(V_{ST})V_{ST} = I_{\parallel} = I/2. \quad (5.13)$$

Note that this implies that at the lowest temperature  $T$  and effective layer separation  $d/l$ , since  $\sigma_{xx}^{\parallel} \rightarrow 0$ , no current  $I$  is able to flow. For finite  $\sigma_{xx}^{\parallel}$ ,  $I$  is given by solving the Eq. 5.12 and Eq. 5.13 self-consistently.

### 5.8.2 Measurement of arm resistances

Combining two terminal and four terminal tunneling measurements at  $\theta = 0$ , the resistance  $R_0$  in the above model can be determined. This is because for tunneling current  $I < I_c$ , the four terminal tunneling voltage remains  $\approx 0$  and all the voltage drop in the tunneling circuit happens across the arms contacting the condensate and known external resistors. Only the “supercurrent” branch of the tunneling  $I - V$  is used to extract  $R_0$ . Fig. 5.16 shows the 2-terminal and 4-terminal  $I - V$  used to estimate  $R_0$ .

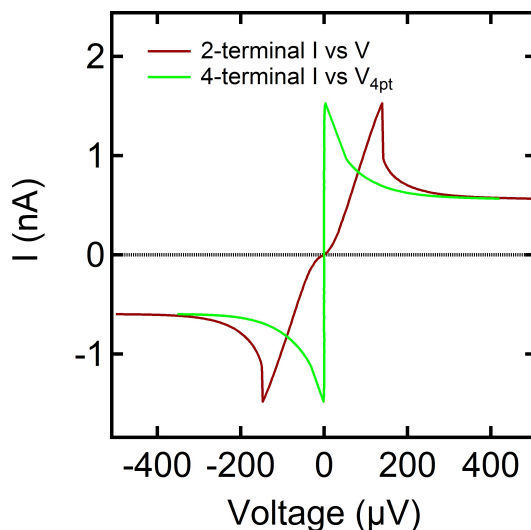


Figure 5.16: The green trace is the two terminal tunneling whereas the black trace is the four-terminal tunneling at  $T \approx 20$  mK,  $d/l = 1.5$ , and  $\theta = 0$

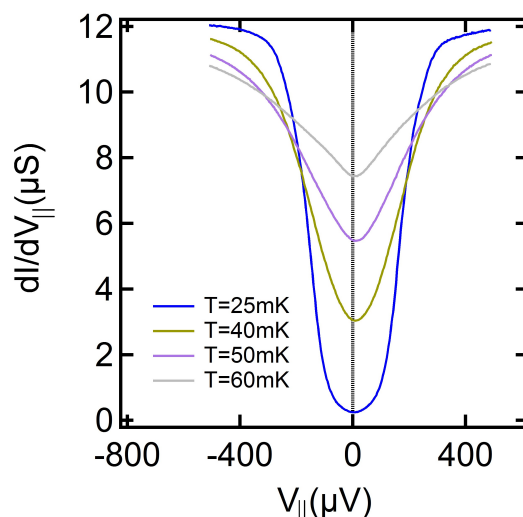


Figure 5.17: Plot of Corbino conductance vs applied bias voltage at  $d/l = 1.5$  for source and drain voltages on opposite rims. Sample is tilted by  $\theta = 26$  degrees.

### 5.8.3 Measurement of $\sigma_{xx}$

In Fig. 5.17 the Corbino conductance  $dI/dV_{||}$  is plotted vs.  $V_{||}$  where  $V_{||}$  is the bias voltage applied across the outer and inner rim with both layers in parallel. The minima in  $dI/dV_{||}$  at zero bias for the lowest temperatures of 25 mK implies the

insulating behavior of the quantum Hall state. The minimum conductance increases as the temperature is increased. This increase in conductance minima is due to enhanced quasi-particle transport. Also,  $dI/dV_{\parallel}$  increases for large applied dc voltages indicative of breakdown of the quantum Hall effect. The Corbino conductance has a thermally activated behavior governed by the quantum Hall gap  $\Delta = 360$  mK for effective layer separation  $d/l = 1.5$ .

## 5.9 Comparison of model vs experiment

The drive current  $I_1$  and drag current  $I_2$  are computed according to Eq. 5.9 and Eq. 5.10, respectively. In Fig. 5.18, the solid curves are the experimental drive and drag data whereas the dashed curves are based on the theoretical model. Interestingly,

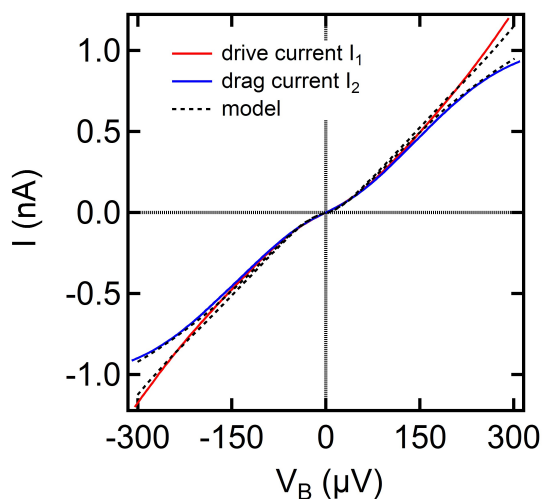


Figure 5.18: The solid traces are Coulomb drag measurements for  $d/l = 1.5$  and  $T = 25$  mK. The red trace is drive current and the blue trace is drag current at  $\theta = 26$  degrees. The black dashes curves are computed from the 1D model.

the 1D-model that assumes dissipation-less transport of excitons can capture the resistance of the drive and drag currents at small biases almost accurately. Even the origin of the non-linearity in series resistances to the condensate is justified from a comparison of the experimental data to the 1D-model. Also, at larger biases  $\approx 150$   $\mu\text{V}$  the drag and drive currents separate out and the model captures this effect as

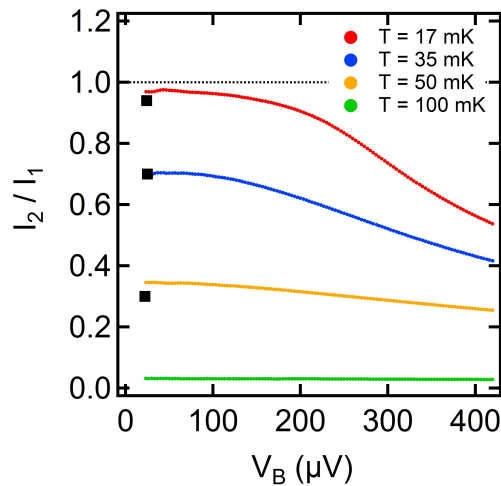


Figure 5.19: Comparison of experimental data to 1D-model for temperature dependence of drag current to drive current ratio for  $d/l = 1.5$  and  $\theta = 26$  degrees. The black dots are predictions from the 1D-model.

coming from the finite  $\sigma_{xx}$  at higher bias voltages. The ratio of the drag to drive currents is also computed in the 1D-model and is represented by the black dots in Fig. 5.19. The model attributes the lowering of drag/drive ratio to an increase in  $\sigma_{xx}$  at elevated temperatures.

## 5.10 Conclusion

Coulomb drag in two spatially separated conductors can cause current to flow through the passive layer in response to current driven in the active layer. In most scenarios, this is a small effect. However, in the exciton condensate state at  $\nu_T = 1$ , the drag current can be of equal magnitude and opposite to the drive current. In this chapter, we have demonstrated precisely this phenomenon. It is consistent with the bulk transport of excitons and also consistent with a simple model of exciton superfluidity.

## Chapter 6

# Effects of microwaves on interlayer tunneling at $\nu_T = 1$

Coupling microwave radiation to electron systems have led to prominent phenomenon like the photon assisted tunneling through quantum dots [133, 134, 135]. When superconducting tunnel junctions are subject to microwave radiation, an *ac* Josephson-effect [136, 137, 138, 139, 140] is observed as described in section 6.2. This phenomenon has also been observed in superfluid helium [141, 142, 143, 144] and in Bose-Einstein condensates [145, 146, 147, 148, 149]. The observation by Spielman et al. [2] of a tunneling anomaly bearing resemblance to the *dc* Josephson effect motivated the search for an *ac* Josephson effect in the exciton condensate state at total filling factor  $\nu_T = 1$ . In this chapter, the microwave engineering involved in studying such an effect at cryogenic temperatures and sample design considerations are discussed. The major challenge faced in realization of the experimental goal is microwave induced thermal effects. Possible ways to tackle these heating effects in order to observe the *ac* Josephson effect are also discussed.

### 6.1 Photon Assisted Tunneling

The phenomenon of photon assisted tunneling was first observed by Dayem and Martin [150]. It was observed that the tunneling  $I - V$  gets modified at  $eV = \gamma\hbar\omega$  where  $\hbar\omega$  is the photon energy and  $\gamma$  is the number of photons absorbed or emitted as shown in Fig. 6.1. The superconducting tunnel junction itself was used as a microwave strip

line through which the electromagnetic wave propagates [19]. This phenomenon was

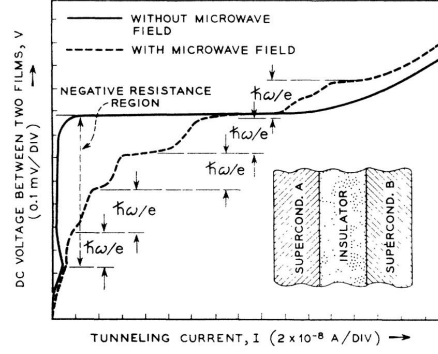


Figure 6.1: Voltage  $V$  vs. tunneling current  $I$  of a superconducting tunnel junction measured in the dark and in the presence of microwaves. Data is due to Dayem and Martin [19].

qualitatively explained by Tien and Gordon [19]. The tunneling  $I - V$  in the dark is governed by

$$I(V) = const \times \int \rho_1(E)\rho_2(E - eV)[f(E - eV) - f(E)]dE. \quad (6.1)$$

Here  $\rho_1(E)$  and  $\rho_2(E)$  are the density of states of two conductor of the tunnel junction at energy  $E$ .  $f(E)$  is the Fermi Dirac distribution of electrons. In the presence of microwave photons, the Hamiltonian  $\tilde{H}(t)$  becomes time dependent and gets modified as

$$\tilde{H}(t) = H_0 + eV_\omega \sin \omega t. \quad (6.2)$$

The wavefunction  $\tilde{\psi}$  also changes accordingly

$$\tilde{\psi} = \psi_0 e^{-i\frac{eV_\omega}{\hbar} \int \sin \omega t dt}, \quad (6.3)$$

$$\tilde{\psi} = \psi_0 e^{+i\frac{eV_\omega}{\hbar} \cos \omega t}. \quad (6.4)$$

Expanding in terms of Bessel functions gives

$$\tilde{\psi} = \psi_0 \sum_{\gamma=-\infty}^{\gamma=+\infty} i^\gamma J_\gamma\left(\frac{eV_\omega}{\hbar\omega}\right) e^{i\gamma\omega t}. \quad (6.5)$$

From the orthogonality of Bessel functions, the modified density of states  $\tilde{\rho}(E)$  is given by

$$\tilde{\rho}(E) = \sum_{\gamma=-\infty}^{+\infty} \rho(E + \gamma\hbar\omega) J_{\gamma}^2(eV_{\omega}/\hbar\omega), \quad (6.6)$$

where  $J_{\gamma}$  is the Bessel function of order  $\gamma$ . This results in a modified  $dc$  tunneling  $I - V$  in the presence of microwave photons given by

$$\tilde{I}(V) = const \times \sum_{\gamma=-\infty}^{+\infty} J_{\gamma}^2(eV_{\omega}/\hbar\omega) \int [\rho_1(E + \gamma\hbar\omega)] \rho_2(E - eV) [f(E - eV) - f(E)] dE, \quad (6.7)$$

$$\tilde{I}(V) = \sum_{\gamma=-\infty}^{+\infty} J_{\gamma}^2(eV_{\omega}/\hbar\omega) I(V + p\hbar\omega/e). \quad (6.8)$$

This simple mathematical formulation was able to qualitatively explain the quantized steps in  $dc$  voltage of the tunneling  $I - V$  for a superconducting tunnel junction.

## 6.2 AC Josephson effect

Other than photon assisted tunneling, an even more spectacular effect can occur in superconducting tunnel junctions as was first realized by Josephson [136, 139, 140]. Each superconductor has a macroscopic phase, say  $\phi_1$  and  $\phi_2$ . The tunneling current through the junction obeys the Josephson relation [136, 151]

$$I_J = I_C \sin(\phi_1 - \phi_2), \quad (6.9)$$

$$\frac{\partial(\phi_1 - \phi_2)}{\partial t} = \frac{2eV}{\hbar}. \quad (6.10)$$

Now across the Josephson junction, an  $ac$  voltage  $V_{\omega} \cos \omega t$  is applied in addition to the  $dc$  bias voltage  $V$ . This modifies the above equations as follows:

$$I_J = I_C \sin(\phi_1 - \phi_2), \quad (6.11)$$

$$\frac{\partial(\phi_1 - \phi_2)}{\partial t} = \frac{2e}{\hbar} (V + V_{\omega} \cos \omega t). \quad (6.12)$$

This can be integrated to obtain

$$I_J = I_C \sin\left(\frac{2e}{\hbar}\left(V + \frac{V_\omega}{\omega} \sin \omega t\right)\right). \quad (6.13)$$

Now using standard expansions the above equation can be expanded as

$$I_J = I_C \sum_{\gamma=-\infty}^{+\infty} \left| J_\gamma\left(\frac{2eV_\omega}{\hbar\omega}\right) \right| \sin\left[\left(\frac{2eV}{\hbar} - \gamma\omega\right)t\right]. \quad (6.14)$$

This effect was first observed by Shapiro in Al/Al<sub>2</sub>O<sub>3</sub>/Sn superconducting tunnel

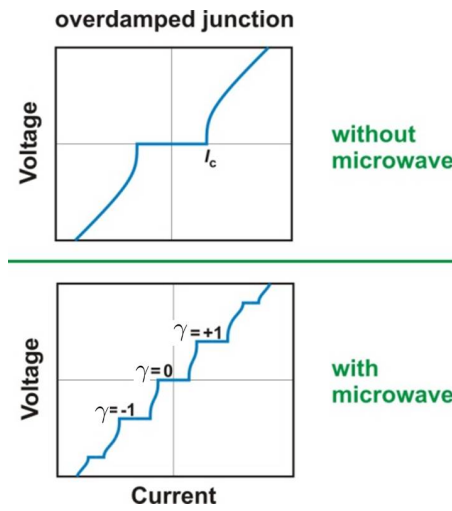


Figure 6.2: Tunneling voltage vs current for a superconducting Josephson junction (a) in the absence of microwave photons and (b) in the presence of microwave photons. This effect was discovered by Sidney Shapiro. Data is from Johannes Kohlmann and Ralf Behr et al. [20]

junctions [137]. In Fig. 6.2, the time averaged *dc* tunneling  $I - V$  had replicas of the zero voltage supercurrent branch at voltages  $\gamma\hbar\omega/2e$ . For superconducting Josephson junctions, the key differentiation between Shapiro steps and photon assisted tunneling of quasi-particles is that the voltage steps are quantized in units of  $\gamma\hbar\omega/2e$  and  $\gamma\hbar\omega/e$ , respectively.

### 6.3 Theory of effects of microwaves on quantum Hall bilayers at $\nu_T = 1$

The important distinction between the Shapiro effect expected in the exciton condensate state at  $\nu_T = 1$  and in a superconducting tunnel junction is that there are no charge  $2e$  Cooper pairs. Instead the tunneling particle is a charge  $e$  electron first predicted by Wen and Zee [69]. Hyart and Rosenow [21] theoretically studied the Shapiro effect in bilayers in the presence of disorder induced topological defects called merons. A similar model was also studied earlier by Stern et al. [37]. According to Hyart and Rosenow's calculations, if a time dependent voltage is imposed across the bilayer

$$V(t) = V_{dc} + V_{\omega} \cos \omega t. \quad (6.15)$$

The tunneling current  $I_{dc}$  gets modified as

$$I_{dc}(V_{dc}) = \sum_{\gamma=-\infty}^{+\infty} J_{\gamma}^2(\beta) I(V_{dc} + \gamma \hbar \omega / e). \quad (6.16)$$

Here the argument  $\beta = eV_{\omega}/\hbar\omega$ . Note that this is exactly what happens for photon assisted tunneling according to Tein and Gordon [19] given by Eq. 6.8. The effect of disorder is understood to introduce a spatial correlation length  $\xi$  that washes away the Fraunhofer pattern as found by Spielman et al. [9] and discussed in section 3.2.3. The fluctuations in the vortex field also introduces a correlation time  $\tau_{\phi}$ . A parameter  $\alpha = \xi/c\tau_{\phi}$  is introduced to characterize the decoherence rate where  $c$  is the pseudospin wave velocity [21]. In Fig. 6.3 (a) the tunneling  $I - V$  is shown for  $\beta = 1, 2, 3$ . As is clear from Eq. 6.16, for large  $\beta$  multi-photon processes are easier to observe. The strength of the photon assisted tunneling processes are governed by  $\beta$ . Fig. 6.3 (b) shows that with increased decoherence rate, the photon assisted tunneling processes become much difficult to discern and get washed away for  $\alpha = 0.2$ . However for smaller values of  $\alpha$ , the photon assisted tunneling steps survive the effect of disorder.

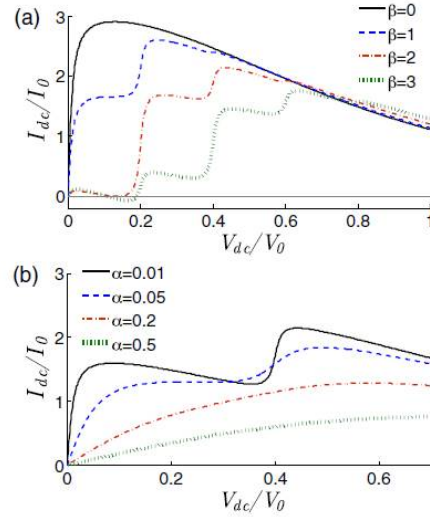


Figure 6.3: (a) Tunneling  $I - V$  due to absorbed or emitted microwave photons at  $eV_{dc} = \gamma\hbar\omega$  for different values of  $\beta = eV_{\omega}/\hbar\omega$ . (b) Dependence of the tunneling  $I - V$  on the decoherence rate  $\alpha$ . Reproduced from Hyart and Rosenow [21].

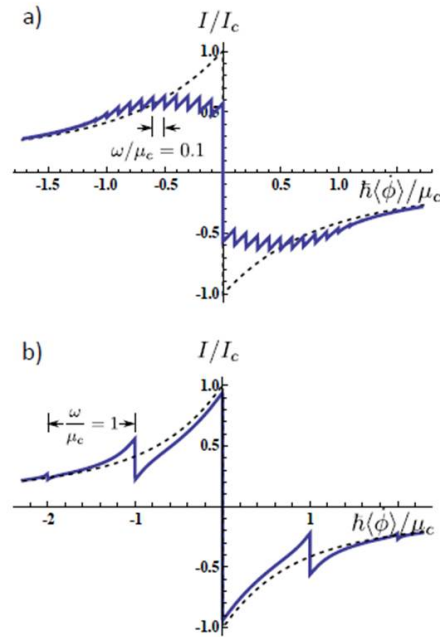


Figure 6.4: The dashed curve is the calculated tunneling  $I - V$  in the absence of microwaves and the solid trace is the modified  $I - V$  in presence of microwaves of angular frequency  $\omega$ . (a)  $\hbar\omega = 0.1\mu_c$  and (b)  $\hbar\omega = \mu_c$ .  $I_c$  is the critical current and  $\mu_c$  is the dc bias voltage at which the critical current  $I_c$  is exhibited. Reproduced from Sodemann et al. [3].

In contrast to the Hyart and Rosenow [21] findings, Sodemann et al. [3] observe that the exciton condensate would exhibit Shapiro steps similar to the superconducting Josephson junctions where the order parameter  $\phi$  becomes time independent for integer values of  $\omega$  and therefore exhibits a supercurrent branch at finite interlayer voltage. In Fig. 6.4 (a) and Fig. 6.4 (b) the modifications of the tunneling  $I - V$  as calculated by Sodemann et al. is shown for  $\hbar\omega = 0.1\mu_c$  and  $\hbar\omega = \mu_c$ , respectively. Here  $\mu_c$  is the applied *dc* bias voltage at which the tunneling current  $I$  goes from supercurrent branch to resistive branch when no *RF* is applied. Experimentally distinguishing the two scenarios presented here is challenging because for the case of bilayer  $\nu_T = 1$ , both photon assisted tunneling and Shapiro steps occur at discrete interlayer voltage  $V = \gamma\hbar\omega/e$ , where  $\gamma = 1, 2, 3$ .

## 6.4 Experimental implementation

An experiment was built with the motivation to observe the *ac* Josephson effect. Each step required several careful considerations as discussed below.

### 6.4.1 Frequency range selection

The modification of the tunneling  $I - V$  for both photon assisted tunneling and Shapiro steps is governed by  $eV_\omega/\hbar\omega$ , where  $V_\omega$  is the *RF* voltage applied across the two layers of two-dimensional electron gas embedded in the bilayer GaAs / AlGaAs heterostructure. When  $eV_\omega/\hbar\omega$  is close to 1, one is likely to see features pertaining to the photon energy quanta  $\hbar\omega$ . Greater the factor  $eV_\omega/\hbar\omega$ , higher the modifications due to electromagnetic radiation. Given this consideration alone, a lower angular frequency  $\omega$  should be preferred. However, there are competing considerations. The spacing between the replicas of the “supercurrent” branch in interlayer voltage  $\Delta V$  is given by  $\Delta V = \hbar\omega/e$ . The features would be more spaced out in interlayer voltage for higher angular frequency  $\omega$  and therefore easier to resolve. Thermal broadening would impose limitation on how much closely spaced features can be resolved. The lowest temperature attainable in the dilution fridge is  $\approx 10$  mK, so the photon energy

should be greater than 0.2 GHz. Also, the tunneling “supercurrent” branch in the

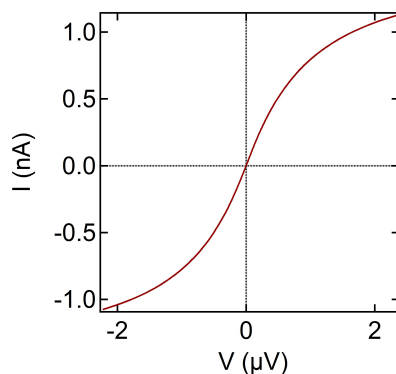


Figure 6.5: Plot of tunneling “supercurrent” branch showing that it has a finite resistance. The interlayer separation  $d/l = 1.5$  and  $T = 50$  mK

four-terminal  $I - V$  in Fig. 4.5 is not absolutely vertical but has a small resistance as pointed out in Fig. 4.5.4. The “supercurrent” branch also has a curvature as shown in Fig 6.5. This would make features less than  $4 \mu\text{V}$  apart in interlayer voltage hard to resolve. Thus the photon frequency should be at least 1 GHz. Taking into account the above considerations, it was determined that an experiment can be designed for photon frequency centered around  $f = 5$  GHz. This would space out the photon induced features by  $21 \mu\text{V}$ . The  $RF$  components were chosen such that one could explore frequencies in the range of 1 GHz to 10 GHz. The  $RF$  engineering involved for microwaves gets incrementally challenging with higher frequencies.

### 6.4.2 Sample design

The next design issue was how to apply the  $RF$  voltage  $V_\omega$  across the double quantum well. In the case of superconducting tunnel junctions, the  $ac$  component of the voltage is commonly imposed on the two superconductors separated by an insulator. An analogous idea of imposing the  $RF$  between the source and drain in addition to the applied  $dc$  bias was initially explored. This idea is schematically depicted in Fig. 6.6 (a).

Fig. 6.6 (b) shows the top view of a device designed to apply the  $RF$  voltage

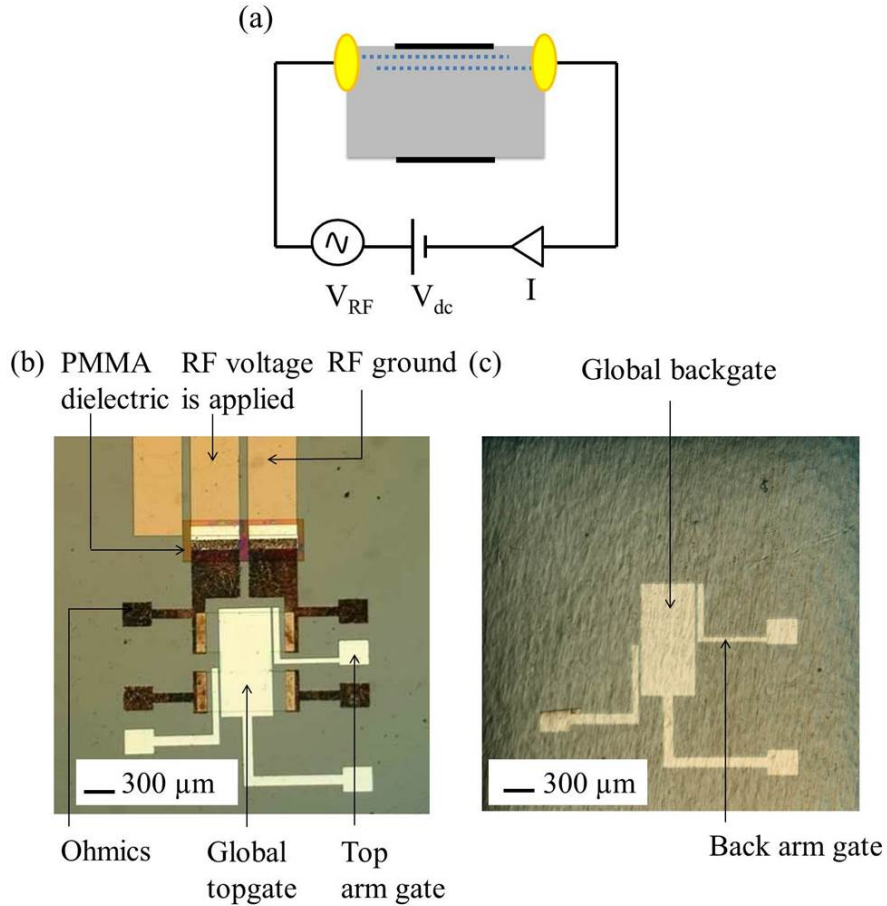


Figure 6.6: (a) Schematic of  $RF$  voltage applied  $V_{RF}$  in addition to the dc applied bias  $V_{dc}$  between the source drain contacts in a tunneling configuration. The current  $I$  is measured. The blue dotted lines represent the bilayer two dimensional electron gas layers. (b) Top side image of a device made for  $RF$  voltage applied across two of the ohmics. (c) Back side image of the same device.

across the source drain ohmics. The rough metallic surface is Ni/AuGe annealed to diffuse into the GaAs and contact the bilayer two dimensional electron gas. The white metallic regions are aluminium top gates. A burnt PMMA dielectric was patterned on top of the ohmics and then a gold coplanar waveguide structure was evaporated for  $RF$  injection through a parallel plate capacitor. Fig. 6.6 (c) is the backside of the same device. The device is thinned to  $\approx 50 \mu\text{m}$ . The backside lithography is done by viewing the front side in an IR camera. The detailed fabrication steps are enumerated in Appendix B. However, it was realized that imprinting a spatially

uniform *ac* voltage across the double quantum well in the  $\nu_T = 1$  state is not possible in this device geometry. The quantum Hall state offers a resistance of  $h/e^2$  and there are additional arm resistances. However, the parallel plate capacitance between the two layers 28 nm apart embedded in GaAs of dielectric constant 13 is  $4.1 \times 10^{-3}$  F/m<sup>2</sup> per unit area which is virtually a short for the *RF* frequency of 5 GHz. Hence the applied *RF* voltage would almost entirely drop across resistors external to the parallel plate capacitor due to the bilayer.

Exploring alternate avenues to imprint the *RF* on the bilayer led to exploring the idea of putting the *RF* across the global top and back gates as shown in Fig. 6.7 (a). The global top and backgates form a parallel plate capacitor with primarily GaAs as the dielectric. The *RF* voltage thus imposed would be spatially uniform and coincide with the entire region where filling factor  $\nu_T = 1$  is established. The center to center separation between the double quantum wells is 28 nm. The GaAs sample is thinned to 50  $\mu\text{m}$  and is nearly as thin a sample as can be handled in the present fabrication and wire-up technique. In order to get an *ac* excitation of  $V_\omega$ , 1800 times more *RF* voltage has to be applied across the top and bottom gates. This implies that 1800<sup>2</sup> times more *RF* power has to be delivered to the device than is needed across the double quantum well to generate the photon assisted tunneling processes. This could be problematic if the *RF* power got partially absorbed rather than all reflected as in the case of an ideal capacitor and could cause heating.

Fig. 6.7 (b) shows the top-view of a device (A) fabricated to apply *RF* between the global top and bottom gates. Aluminium is evaporated as the top gate as well as the arm gates. There are 4 ohmics made of diffused Ni(135Å)/AuGe(1600Å). The contact pads are also made of Ni(135Å)/AuGe(1600Å). The narrow interconnects between the ohmics/ arm top gates and the contact pads are made of nichrome to make it resistive in order to prevent *RF* currents leaking out to ground. Indium solder blobs are used to connect gold wires to the contact pads. Fig. 6.7 (c) is the backside image of the 50  $\mu\text{m}$  thinned device. The central aluminium backgate extends into triangular soldering pad away from the actual mesa. The resistive nichrome interconnects connect the arm back gates to the aluminium contact pads. The area of the tunnel junction underneath

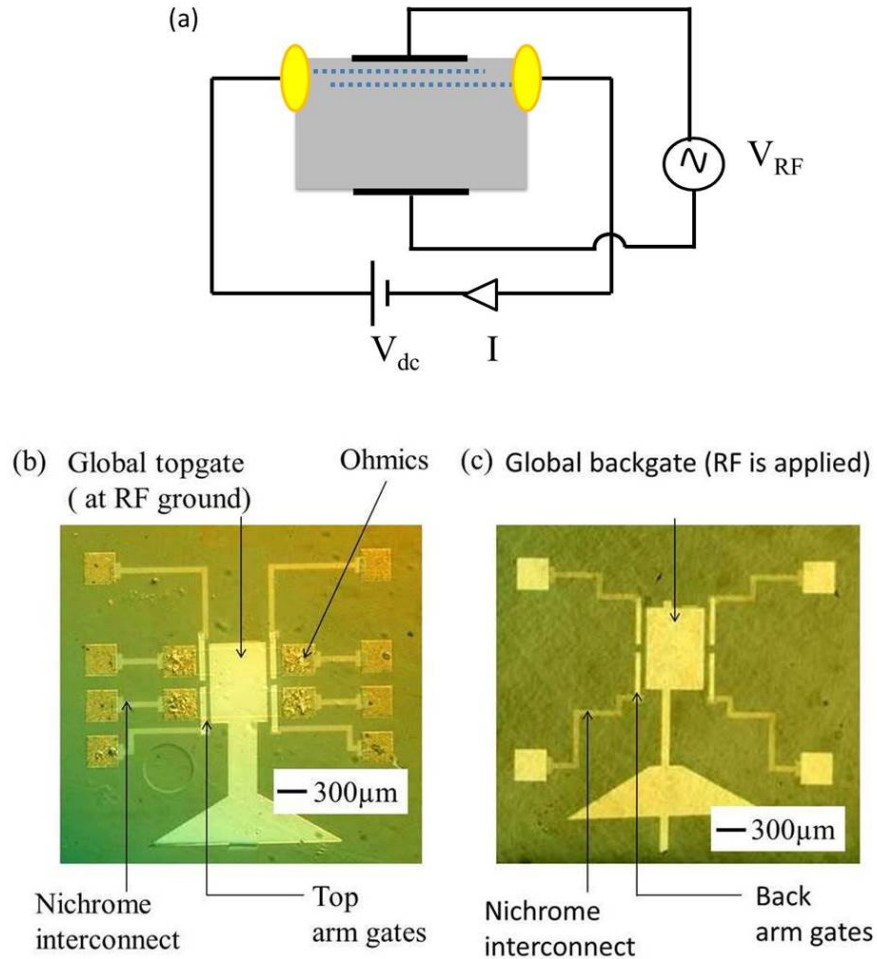


Figure 6.7: (a) Schematic of  $RF$  voltage applied  $V_{RF}$  applied between the global top and bottom gates. The blue dotted lines represent the bilayer. Bias voltage  $V_{dc}$  is the voltage applied across the tunnel junction and  $I$  is the tunneling current. (b) Top view of device (A) to apply  $RF$  across the global top and bottom gates. (c) Backside view of device (A).

the global top and back gates is  $550\ \mu\text{m} \times 675\ \mu\text{m}$ . Gold wires are connected to the back arm gates by silver epoxy. The wire to the main back gate which carries  $RF$  voltage is indium soldered to minimize contact resistance. The fabrication and wire-up steps are presented in further detail in Appendix B. Wirebonding could not be used as the device is fragile and floats on its gold wires. Wirebonding requires that the substrate be rigidly anchored in place.

The  $RF$  voltage applied on the back gate and  $RF$  ground applied on the top

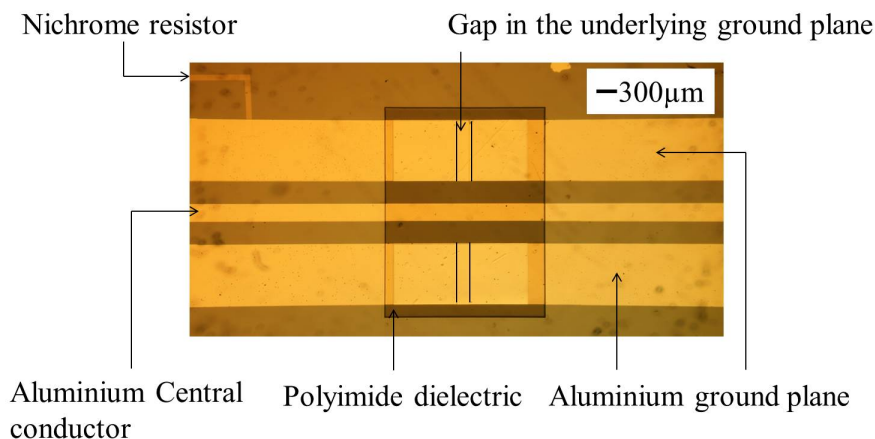


Figure 6.8: Image of a coplanar waveguide on pristine GaAs. The metal pattern is made of aluminium. The rectangle patterned in the middle is of polyimide. The  $RF$  is transmitted through the central conductor. The outer ground planes made of aluminium have a gap in the middle and aluminium patterned on top of the polyimide to make a capacitor geometry.

gate as well as the reverse situation is identical in terms of how much  $RF$  voltage difference  $V_\omega$  appears across the double quantum well. However, the common mode  $RF$  voltage is  $\approx 80$  times smaller when  $RF$  is on the back gate than when on the top gate. Hence this configuration was chosen. This gives rise to the question of how the addition of  $RF$  and  $dc$  signals can be performed on the gates. Using a cryogenic bias tee is a reliable way to perform this addition. Hence a bias tee was installed at the mixing chamber and the input signals were a back gate voltage and an  $RF$  excitation that got added together at its output. This central conductor was connected to the central conductor of a  $5\text{ mm} \times 10\text{ mm}$  GaAs coplanar waveguide and then connected to the back gate. The top gate has to have a  $dc$  voltage and also needs to be at  $RF$  ground. This was achieved by careful designing of the coplanar waveguide as shown in Fig. 6.8. The design of the coplanar waveguide is described in detail in Appendix C. The device is shown after wire-up in Fig. 6.9. After the wire-up, the sample is inserted into a 4.2 K dewar for preliminary characterization. The important test is to confirm that all the wires are connected.

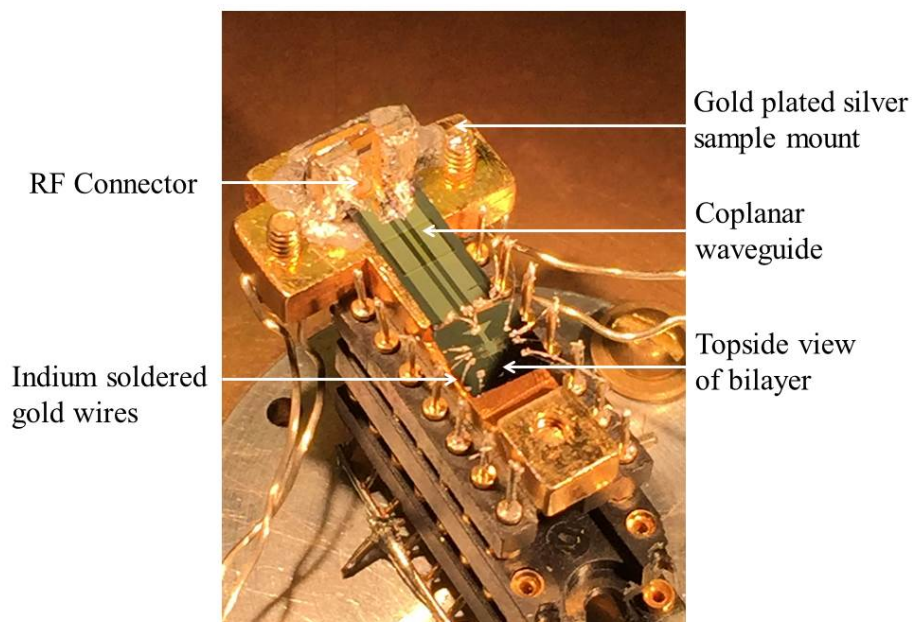


Figure 6.9: Image of the thinned bilayer sample after wire-up. The backgate is connected to the central conductor of the coplanar waveguide through which the  $RF$  voltage is applied. The topgate is connected to the ground planes of the coplanar waveguide also with indium soldered gold wires. The coplanar waveguide is connected to the  $RF$  connector at the sample mount with indium solder.

### 6.4.3 Cryostat modification

The remaining challenge is of connecting the room temperature  $RF$  source down to the cryogenic bias tee thermally anchored to the mixing chamber at  $\approx 10$  mK. The  $RF$  signal generator is also emitting room temperature 300 K Johnson noise. This Johnson noise needs to be filtered out. So a coax cable cannot run straight down to the mixing chamber. The Johnson noise power  $P_J$  is given by

$$P_J = 4K_B T \Delta f, \quad (6.17)$$

where  $K_B$  is the Boltzmann constant and  $\Delta f$  is the frequency bandwidth of the coax cable. The Johnson noise is intercepted by cryogenic attenuators. The attenuator

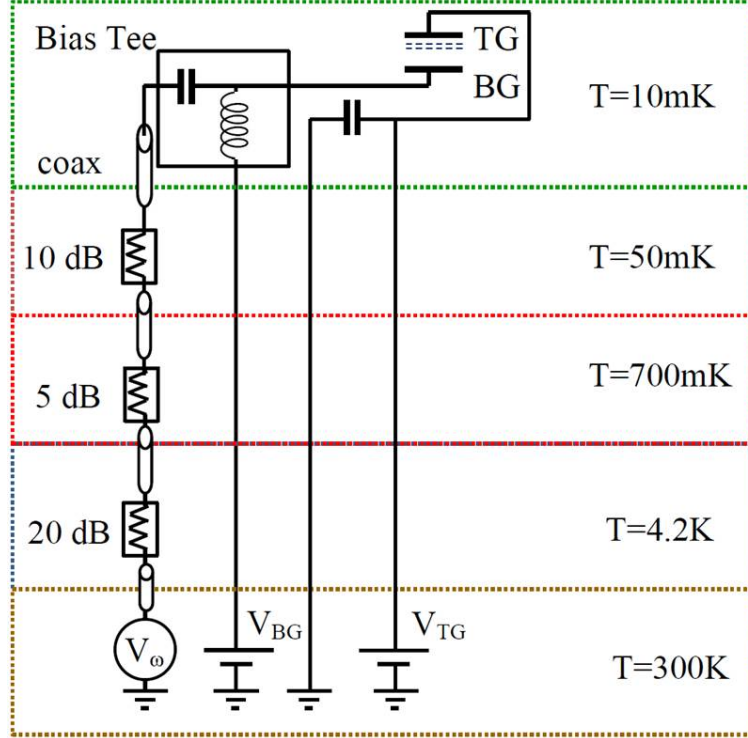


Figure 6.10: The measurement setup build in the dilution refrigerator for coupling the  $RF$  to the bilayer quantum Hall system is schematically represented. The device is represented as a parallel plate capacitor with top and back gates. The attenuators are represented as resistors. The attenuators are introduced for the purpose of reducing thermal Johnson noise. The five stages of the dilution refrigerator are represented as boxes. The temperatures go from room temperature 300 K to the mixing temperature 10 mK in stages.  $V_{TG}$  and  $V_{BG}$  are the gate voltages on the top and bottom gates, respectively.  $V_{\omega}$  is the  $RF$  voltage supplied by the signal generator. Adopted with modifications from Schuster's thesis [22]

value  $\alpha(dB)$  is given by

$$\alpha(dB) = 10 \log_{10}(T_i/T_f). \quad (6.18)$$

Going down from 300 K to 50 mK would require total attenuation of  $\approx 38$  dB inserted in three stages. In the real experimental situation, we installed a 20 dB, 5 dB, and 10 dB cryogenic attenuators from XMA Corporation at the 4.2 K, 0.7 K, and 50 mK respectively. This is a standard procedure to reduce the Johnson noise temperature to below 200 mK as used in experiments related to superconducting qubits. [22].

Fig. 6.10 shows schematic diagram of the set-up to inject  $RF$  and  $dc$  simultaneously. The boxes represent the different stages of the fridge from the room temperature sections at the bottom to the coldest mixing chamber at  $\approx 10$  mK up at the top. Fig. 6.11 shows the  $RF$  engineering done on the dilution refrigerator. With all

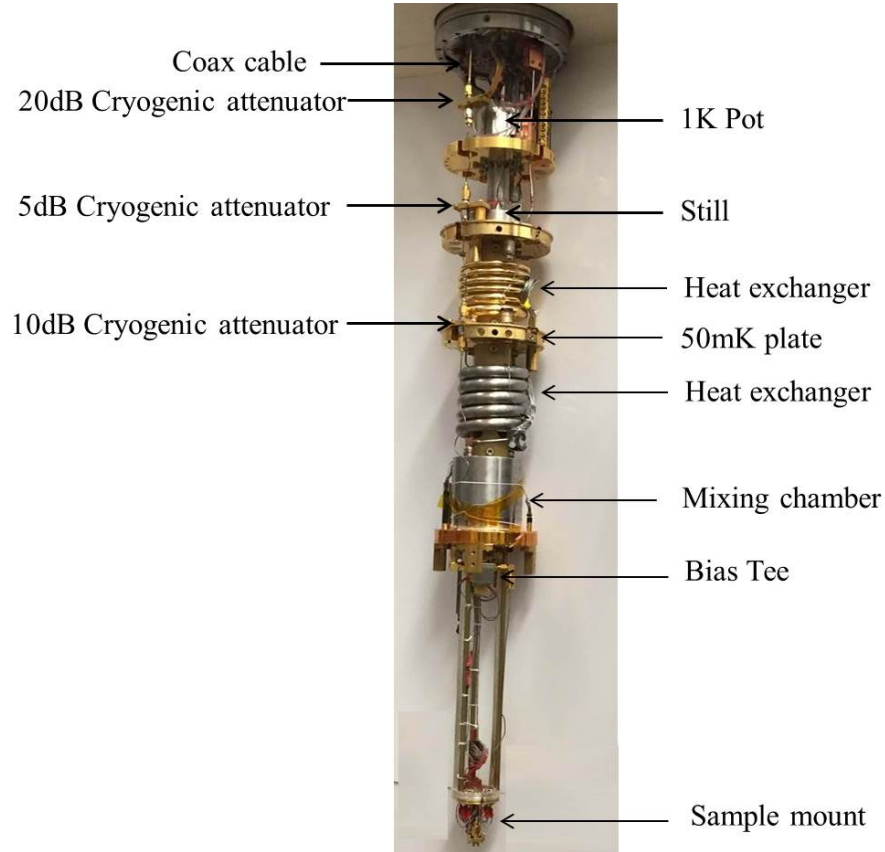


Figure 6.11: Image of the dilution refrigerator. The cryogenic attenuators, the coax cables and the bias tee are marked. The room temperature Johnson noise is attenuated as the signal travels through the coax cable. The 3 cryogenic attenuators of 20 db, 5 db, and 10 db are clamped to the 4.2 K plate, the 0.7 K still, and the 50 mK plates, respectively.

this work in place, the experiment was ready to be tried out.

#### 6.4.4 Power dependence

A 4-terminal tunneling  $I - V$  at  $\nu_T = 1$  as described in subsection 4.5.2 was obtained on device (A) at temperature  $\approx 15$  mK. This corresponds to the red trace in Fig.

6.12. The tunneling critical current  $I_c$  is 3.4 nA. Then the  $RF$  excitation is applied for a fixed frequency of 5 GHz and incremented gradually from -5 dbm to +15 dbm as shown in Fig. 6.12 (a). The tunneling critical current got smaller at higher powers. The slope of the tunneling “supercurrent branch” also increased at higher  $RF$  power and the data gap in the tunneling  $I - V$  disappeared with  $RF$ . The evolution of the tunneling  $I - V$  was similar to when the temperature of the sample was raised. For a comparison, the temperature dependence of the 4-terminal tunneling  $I - V$  was studied as shown in Fig 6.12 (b). For the ease of comparison, the tunneling  $I - V$

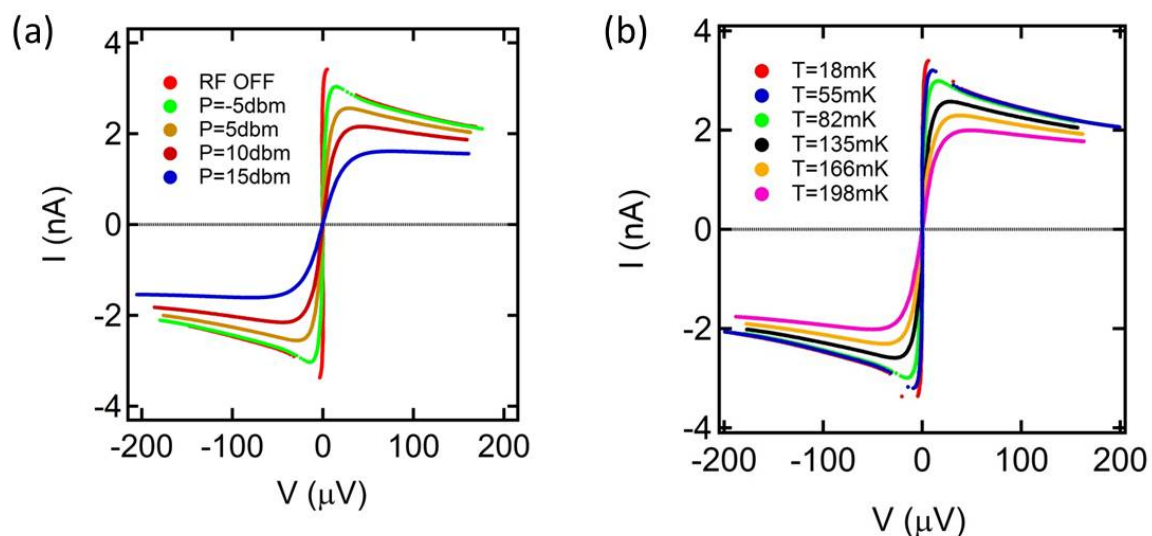


Figure 6.12: (a) Tunneling current  $I$  plotted vs. measured 4-terminal voltage  $V$  at  $T = 15$  mK,  $d/l = 1.52$ , and  $\theta = 0$  degrees. The  $RF$  frequency is 5 GHz.  $P$  denotes the different RF powers outputted at the signal generator (b) Temperature dependence of tunneling  $I - V$  without  $RF$  power for  $d/l = 1.52$  and  $\theta = 0$  degrees.

obtained at  $T = 15$  mK and signal generator  $RF$  power  $P = 5$  dbm is superimposed on tunneling  $I - V$  for  $T = 135$  mK as shown in Fig. 6.13. They matched almost perfectly, suggesting the electron gas was raised uniformly to an elevated temperature.

It became clear that thermal effects due to microwave radiation was the dominant effect that veiled the observation of more subtle phenomenon like photon assisted tunneling or Shapiro steps if present. This led to making an effort at understanding

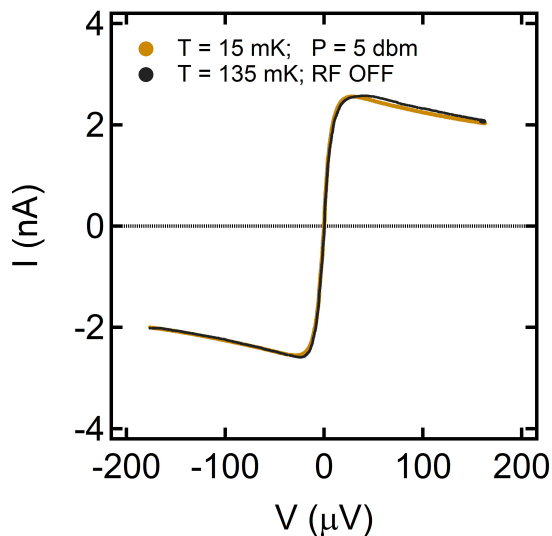


Figure 6.13: Yellow trace is tunneling current  $I$  plotted vs. measured 4-terminal voltage  $V$  at  $T = 15$  mK,  $d/l = 1.52$ , and  $\theta = 0$  degrees. The  $RF$  frequency is 5 GHz and power is 5 dbm at the signal generator output.

the heating mechanism in order to minimize it.

### 6.4.5 Frequency dependence

The most common mechanism of conversion of  $RF$  power into thermal energy is Joule heat. This Joule heat could be generated at several places. For example at the indium soldered gold wire due to capacitive displacement currents generated in charging and discharging of the parallel plate capacitor between the global topgate and backgate or within the electron gas itself in response to the common mode  $RF$  voltage present at the double quantum well. It is also generated at the cryogenic attenuators clamped to the 50 mK plate, 0.7 K still plate, and 4.2 K plate. Another possible heating mechanism is dielectric loss within the GaAs heterostructure itself. The frequency response might allow to distinguish these scenarios. For example, the Joule heat generated due to capacitive displacement current would be  $(V_{\omega} C \omega)^2 R$  where  $C$  is the parallel plate capacitance between the global top and bottom gates,  $R$  is the resistance of the aluminium and indium blob, and  $\omega$  is the angular frequency.

In order to assign a temperature  $T^*$  for a known power  $P$  at a fixed frequency  $f$ ,

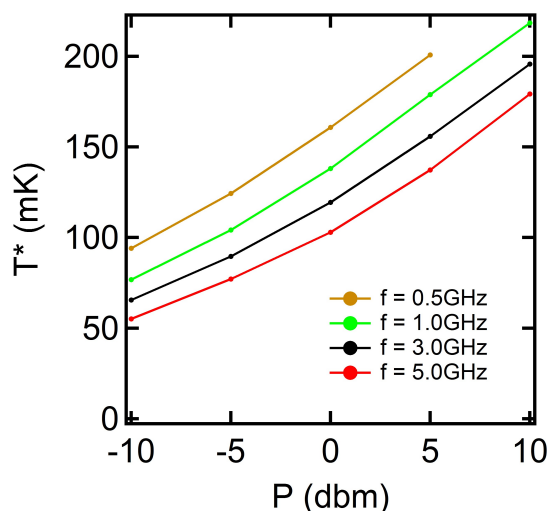


Figure 6.14: The deduced temperature  $T^*$  is plotted vs  $RF$  power at the signal generator output  $P$ . First with the  $RF$  power OFF, the temperature dependence of the critical current is made. Then the magnitude of the critical current is used to deduce the temperature  $T^*$  for measurements at  $T \approx 15$  mK and different  $RF$  powers. This measurement is done at several fixed frequencies.

we first calibrate the critical current  $I_c$  vs  $T$  from Fig. 6.12 (b). Then a temperature  $T^*$  is assigned from the critical current  $I_c$  in Fig. 6.12 (a) for a power  $P$ . Thus the curves of Fig. 6.14 are constructed for fixed frequencies.

The heating due to  $RF$  is more prominent at lower frequencies in the range 0.5 GHz - 5 GHz. This is inconsistent with Joule heating due to capacitive displacement currents. However, the power  $P$  is the  $RF$  power at the top of the cryostat. It suffers 35 db of attenuation due to the cryogenic attenuators. The insertion loss in the coax cables and bias tee increases with frequency  $f$  as measured at room temperature and might explain the observed frequency dependence. The 4.2 K insertion loss in the coax cables and bias tee is not known. It limits the interpretation of the frequency dependence.

#### 6.4.6 Two terminal vs. four terminal

A possible mechanism was that the Joule heat was generated as  $RF$  currents flow out to ground through the four ohmics. If two of the arms were cutoff as in a two-

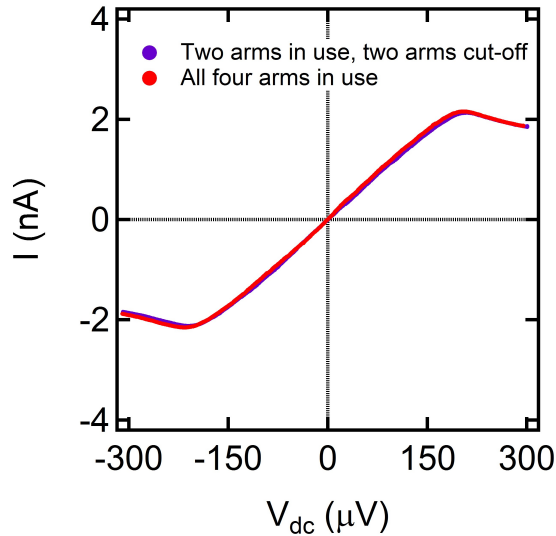


Figure 6.15: Two terminal  $I - V_{dc}$  is plotted. For the red trace, all four ohmics are connected to  $RF$  ground. For the purple trace, only two ohmics are connected to  $RF$  ground and the remaining arms are cutoff with depletion top gates

terminal tunneling configuration, the heating should reduce by a factor of two. Fig. 6.15 shows a comparison when all four arms are connected to  $RF$  ground (red trace) and when only two arms are connected to  $RF$  ground (purple trace). They are essentially identical and no reduction in  $RF$  induced temperature  $T^*$  is observed. This could be because the cooling pathway for the bilayer is also reduced by a factor of two and there is an exact cancelation between the reduction in heating and cooling pathways. Therefore the above test could not eliminate Joule heat within the bilayer as a possibility.

#### 6.4.7 Density dependence

A heating mechanism due to the bilayer two dimensional electron gas itself should be dependent on the electron density of the sample. Thus study of the density dependence of  $T^*$  for a fixed  $RF$  power and frequency could provide information for identifying the heating mechanism. The  $RF$  induced heating was therefore studied at a different electron density per layer while holding the electron density at balance in each layer. The evolution of the four terminal tunneling  $I - V$  was studied with

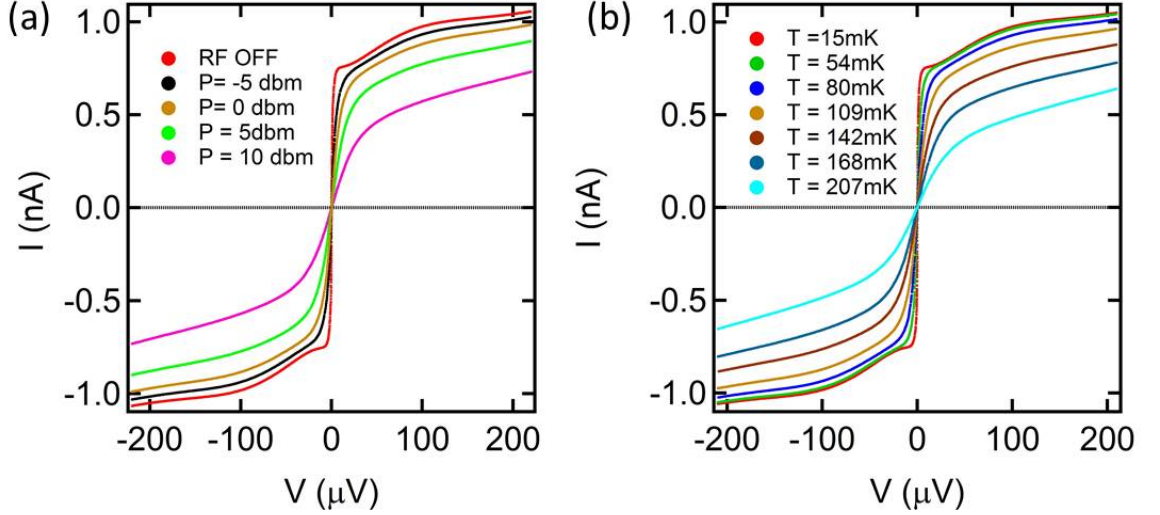


Figure 6.16: (a) Evolution of four terminal tunneling  $I - V$  at  $\nu_T = 1$  with increase in  $RF$  power  $P$  outputted from the frequency generator at  $d/l = 1.73$ ,  $T = 15$  mK, and  $\theta = 0$  degrees. (b) Temperature dependence of the four terminal tunneling  $I - V$  at  $\nu_T = 1$ ,  $d/l = 1.73$ , and  $\theta = 0$  degrees with  $RF$  OFF.

different  $RF$  power  $P$  at  $\nu_T = 1$  for a different  $d/l = 1.73$  at frequency  $f = 5$  GHz and is shown in Fig. 6.16 (a). The evolution of the four terminal tunneling  $I - V$  with temperature was also studied as shown in Fig. 6.16 (b). Extracting the critical currents for effective layer separation  $d/l = 1.73$  was difficult because of the smooth transition from the “supercurrent” branch to the resistive branch. Hence to deduce an effective temperature  $T^*$  for a given  $RF$  power and frequency  $f = 5$  GHz, the slope of the “supercurrent” branch was calibrated against temperature using Fig. 6.16 (b). The slope of the “supercurrent” branch in Fig. 6.16 (a) allowed one to assign a temperature for a  $RF$  power  $P$ . The blue trace in Fig. 6.17 was thus constructed. Fig. 6.17 demonstrates the independence of  $RF$  induced  $T^*$  on effective layer separation  $d/l$  and thereby also on electron density distributed equally per layer. This is evidence that the bilayer itself is not responsible for generating the Joule heat in response to the  $RF$  voltage.

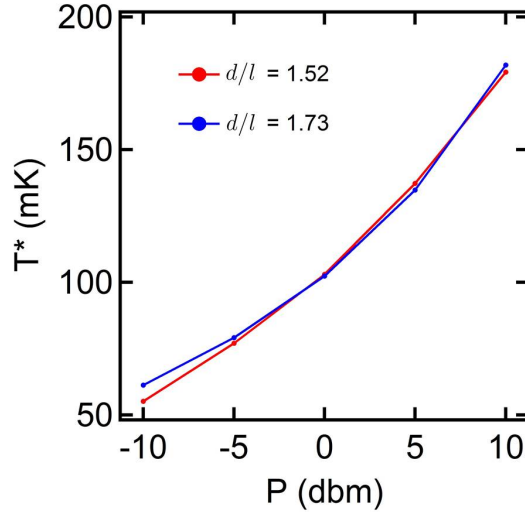


Figure 6.17: The temperature  $T^*$  deduced from tunneling measurements is plotted against the  $RF$  power  $P$  at the signal generator output. The  $RF$  induced heating effect is studied for two different electron gas densities and thereby different effective layer separations, i.e.,  $d/l = 1.52$ , and  $d/l = 1.73$ .

### 6.4.8 Area dependence

It could be due to capacitive displacement currents dissipating in the resistance  $R$  due to aluminium and the soldered indium blob. This Joule heat should be  $(V_\omega C \omega)^2 R$  as discussed earlier. As the parallel plate capacitance  $C$  is proportional to area  $A$ , the Joule heat can be minimized if the overlap area between the global top gate and global back gate is reduced. This led to reducing the area  $A$  in device (A), shown in Fig. 6.7 by a factor of  $\approx 10$  in the design of device (B). A device replica is shown in Fig. 6.18 (a) and Fig. 6.18 (b). One would expect a factor of  $\approx 100$  reduction in  $RF$  heating if this was the heating mechanism. Fig. 6.18 (c) shows a comparison of the temperature  $T^*$  for device (A) and device (B). The temperature  $T^*$  is deduced by adopting the same methodology as explained for Fig. 6.14. The smaller device (B) rises to the same temperature  $T^*$  for  $\approx 10$  times less power than device (A). The model of heating generated due to dissipation of capacitive displacement currents is inconsistent with this observation.

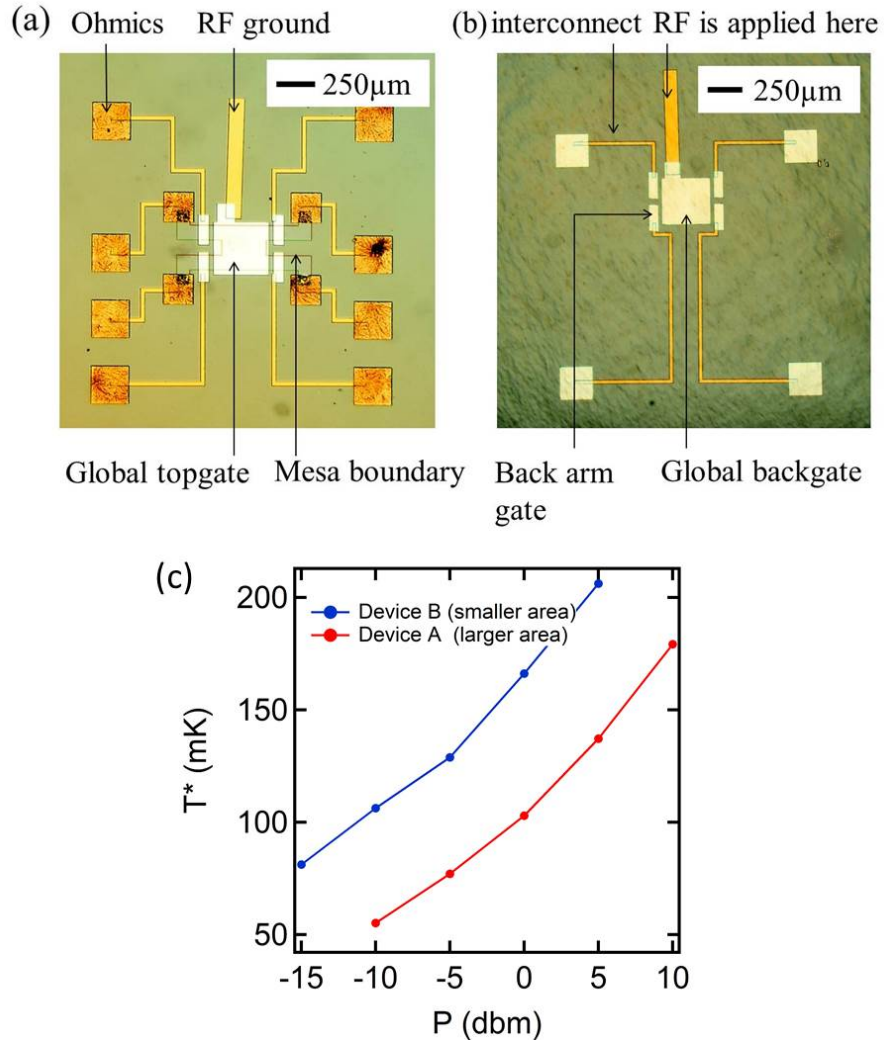


Figure 6.18: (a) Topview of a replica of device (B). (b) Backside view of a replica of device (B). Device (B) is a bilayer tunnel junction with the area underneath the global top and backgate  $350 \mu\text{m} \times 350 \mu\text{m}$ . The white metallized regions in Fig. 6.18 (a) and Fig. 6.18 (b) represent aluminium top and back gates, respectively. The two-dimensional electron gas regions are defined by the mesa boundary. The nichrome interconnects are  $25 \mu\text{m}$  wide. Rectangular gold pads are deposited on the top and backside to indium solder the *RF* gold wires. The sample is thinned down to  $50 \mu\text{m}$ . One difference between the replica and the actual device is that the interconnects are of nichrome in the original device and gold in the device replica. A detailed description of the fabrication process is found in Appendix B. (c) Comparison of the *RF* induced heating effect between device (A) and device (B). Device (B) has  $\approx 10$  times smaller overlap area between the global top gate and the global back gate.

## 6.5 Conclusion and future direction

In conclusion, an experiment was built from the ground up for the synthesis of microwave techniques with the bilayer quantum Hall state at  $\nu_T = 1$  at cryogenic temperature with the motivation to demonstrate *ac* Josephson like phenomenon. However, upon application of *RF* voltages between the parallel plate capacitor formed by the global top and bottom gates, an effect analogous to raising the temperature of the sample was found. A systematic investigation of the *RF* induced heating effects showed that the bilayer two dimensional gas itself was not responsible for the Joule heat. The effective temperature  $T^*$  for an applied *RF* power and frequency remained unchanged when two arms of the 4-terminal device were cut off. This temperature  $T^*$  was also independent of electron density in the bilayer. The charging discharging current of the capacitor formed by the global top and back gates also was not the source of Joule heating. The effective temperature  $T^*$  did not scale with the square of the area when devices of two different overlap areas between the global top and back gates were compared. Other possible sources leading to *RF* induced heating are power dissipated at the cryogenic attenuators bleeding into the device, the GaAs heterostructure itself absorbing the *RF* power, etc. The cooling down of the chip at cryogenic temperatures is poor as it relies purely on electronic thermal conduction. This can be improved by using thicker gold wires and increasing the number of gold wires connected to each ohmic. Changing the interconnect between the ohmic to the soldering pad from resistive nichrome to gold might help the chip to cool down better. Also, using superconducting coax from the cryogenic attenuator at the 50 mK plate down to the device sample mount would remove any heat dissipated at the cryogenic attenuators to bleed into the sample. The present device is  $\approx 50 \mu\text{m}$  thick while the centre to centre distance between the quantum wells is only 28 nm. This required us to apply *RF* voltage that was 1800 times larger than the relevant voltage drop  $V_\omega$  between the quantum wells. The device can be made about  $1 \mu\text{m}$  thick using a technique called epoxy bond and stop etch (EBASE) that is explained in detail in Spielman's thesis [71]. These are several possible ways in which the *RF* induced heat-

ing may be controlled. The minimization of  $RF$  induced heating is crucial for more subtle phenomenon like Shapiro steps or photon assisted tunneling to be observed.

## Conclusion

Initial evidence of Bose-Einstein Condensation of excitons in the  $\nu_T = 1$  state came in tunneling [2] and counterflow [16, 38, 10, 72, 73] experiments done on Hall bar devices. However, demonstration of a bulk condensate mode of transport was not possible in Hall bar devices as all the contacts were along the device boundary. Later experiments by Tiemann et al. [39, 42], Finck et al. [17, 6], and Nandi et al. [130, 49] were done in Corbino geometry to address this question. Both tunneling and “perfect” Coulomb drag experiments presented in this thesis are bulk phenomenon due to exciton condensation in the  $\nu_T = 1$ .

A detailed study of the Josephson-like tunneling phenomenon at  $\nu_T = 1$  [2] was undertaken in Chapter 4. The measured 4 terminal tunneling  $I-V$  was found in good agreement with a simple model of an overdamped voltage biased Josephson junction [3]. The dissipation in the “supercurrent” was found to remain small but finite down to 30 mK. The temperature dependence of this dissipation exhibited an activated behavior governed by the quantum Hall gap. The tunneling critical current  $I_c$  was found to be a macroscopic property of the tunnel junction [80, 42, 93, 95, 79, 3]. A new scaling behavior of the temperature dependence of the critical current  $I_c$  normalized by the lowest temperature value was observed.

In Chapter 5, Coulomb drag studies in a Corbino device in the bilayer quantum Hall state at  $\nu_T = 1$  demonstrated that driving electron current in one layer spontaneously generated hole currents in the other layer of equal magnitude. A simple explanation for such an observation is that electrons in one layer are tightly bound to holes in the other layer as in an exciton condensate. The binding interaction is purely Coulombic. Tunneling between the two layers is suppressed by application

of an in-plane magnetic field [9]. At elevated temperatures or increased effective layer separation, the drag current magnitude becomes smaller than the drive current magnitude due to quasi-particle transport happening simultaneously with excitonic transport. A model of excitonic superfluidity that incorporates dissipation-less counterflow transport due to charge neutral excitons and parallel transport due to charged quasi-particles is found to be in good agreement with the experimental observations.

In Chapter 6, an experiment was built from the ground up to apply  $RF$  voltages across the bilayer in addition to  $dc$  bias in the tunneling configuration. The  $RF$  engineering essential to synthesize microwave techniques with cryogenics was accomplished. However, applying  $RF$  power caused heating of the bilayer to a higher temperature  $T^*$  as inferred from tunneling data. It was demonstrated that the Joule heat was not generated by the bilayer two dimensional electron gas itself as it was independent of density. Comparison of  $RF$  induced heating in two tunnel junctions of overlap area between the global top and global backgate differing by a factor of  $\approx 10$  showed that Joule heat was not generated by the charging and discharging current of the parallel plate capacitor. The device where the  $RF$  voltage was applied across a smaller area capacitor got heated up to a higher effective temperature  $T^*$ . Possible ways to minimize  $RF$  induced heating in the future have been discussed.

## Future directions

Finally, several directions for future study are discussed below which would provide invaluable insights into the physics of the bilayer exciton condensate state at total filling fraction  $\nu_T = 1$ .

### **Exciton dissipation at $\nu_T = 1$ via multi-probe counterflow measurements in Corbino geometry**

The bulk transport of excitons in the Corbino device was found consistent with excitonic superfluidity [17, 130, 65] but a precise study of exciton dissipation could not

be done. Determining the dissipation in excitonic flow would require a multi-terminal Corbino device as shown in Fig 6.19. In such a device, bulk transport of excitons can

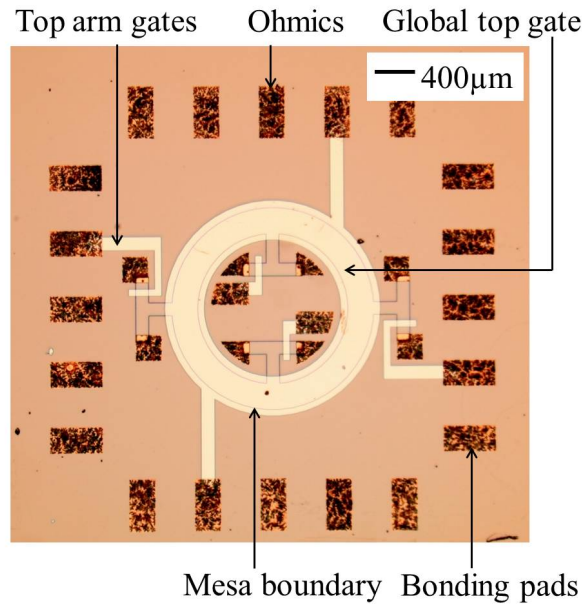


Figure 6.19: Top view of a eight-terminal Corbino device with four arms on the inner rim and four arms on the outer rim. The bilayer two-dimensional electron gas was removed by a solution etch from outside the mesa boundary. The Ni/AuGe ohmics were diffused in. The arm top gates and global top gates were made of evaporated aluminium. This device was fabricated as an initial step in this direction.

be setup either in the counterflow configuration as discussed in Section 5.5 or in the Corbino drag configuration as discussed in Section 5.7. The voltage drop between the top and bottom layers on the inner and outer rims of the Corbino device should be measured. The condition for dissipation-less transport is the equality of the voltage drop measured between the top and bottom layers for the inner and outer rims. For the quantum Hall state at  $\nu_T = 1$ , a finite temperature Kosterlitz Thouless phase transition was predicted by Moon et al. [62], which has not yet been experimentally observed [101]. A measurement of the exciton dissipation would be able to determine the nature of the phase transition.

## Lateral tunneling at $\nu_T = 1$

A sideways tunneling geometry was proposed by Wen and Zee [23] for the observation of fractional Josephson-like phenomenon. The tunneling geometry considered is shown in Fig. 6.20. It is predicted that this lateral tunneling configuration would

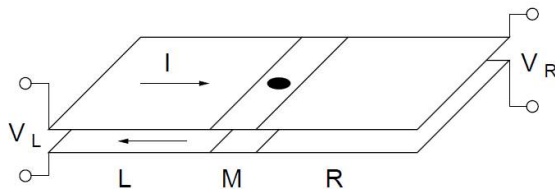


Figure 6.20: The barrier is marked by  $M$ . The electron density in each layer in this region is chosen such that each layer is in an incompressible fractional quantum Hall  $1/m$  state each but the two layers are independent of each other. The regions  $L$  and  $R$  are in the  $\nu_T = 1$  state. The tunneling current  $I$  flows antiparallel in the two layers. Reproduced from Wen and Zee [23].

exhibit ac-Josephson-like phenomenon [23] at

$$\hbar\omega = \frac{1}{m}e(V_L - V_R). \quad (6.19)$$

Here each layer is at filling factor  $1/m$  in the tunneling barrier.  $V_L$  and  $V_R$  are voltages applied between the top and bottom layers in the region  $L$  and region  $R$ , respectively. It would be interesting to experimentally investigate this tunneling geometry. The challenge in the lateral tunneling geometry is that in addition to tunneling between the exciton condensate states at  $\nu_T = 1$  in the regions  $L$  and  $R$ , tunneling between the quantum Hall edge channels would also be present. It would be an experimental challenge to distinguish these two contributions.

## Surface acoustic wave studies at $\nu_T = 1$

In GaAs single quantum wells, the surface acoustic waves have been used to reveal the presence of a Fermi surface at filling fraction  $\nu_T = 1/2$  by Willett et al. [152]. The surface acoustic waves (SAW) probe the electronic conductivity  $\sigma_{xx}(\Omega, \lambda)$  at a fixed

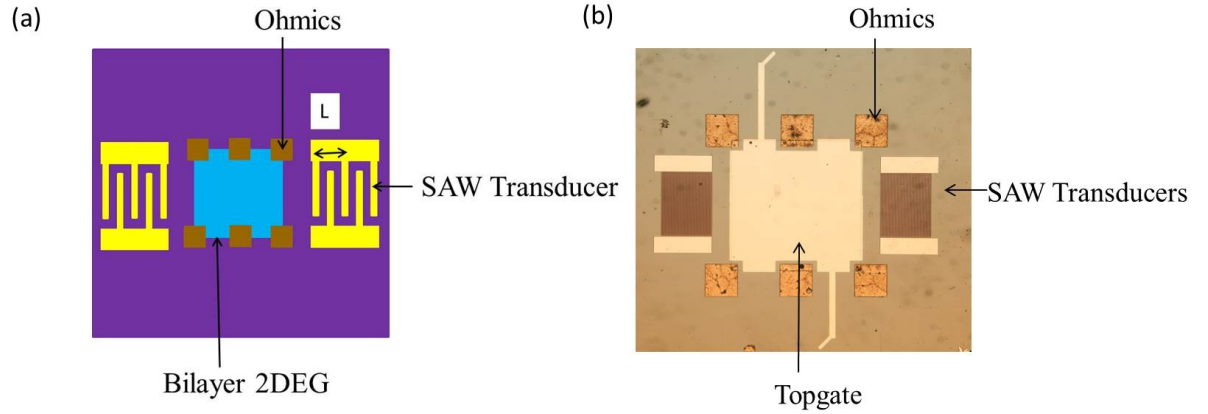


Figure 6.21: (a) Schematic diagram of a surface acoustic wave device. The bilayer two dimensional electron gas is confined to a square with evaporated ohmics marked in brown. The SAW transducers are marked in yellow and can be patterned by e-beam or photolithography. (b) Image of a bilayer SAW device courtesy of J Pollanen.

angular frequency  $\Omega$  and wavelength  $\lambda$  related as  $\lambda\Omega = 2\pi v_s$  where  $v_s$  is the sound velocity in GaAs. SAW studies have never been done on the quantum Hall bilayers. Studying the phase transition between two independent layers at  $\nu_T = 1/2 + 1/2$  to strongly correlated layers at  $\nu_T = 1$  with SAW might be interesting. One might also study the electron conductivity  $\sigma_{xx}(\Omega, \lambda)$  deduced from SAW measurements as a function of interlayer imbalance. Fig. 6.21 (a) shows a schematic of a SAW device with the bilayer two-dimensional electron gas etched into a square-shaped mesa. SAW transducers are patterned on either sides and act as transmitters and receivers. The SAW wavelength  $\lambda$  is such that  $n\lambda = L$ , where  $L$  is the centre to centre distance between two fingers marked in Fig. 6.21 (a). This is an ongoing effort in the group and Fig. 6.21 (b) is a bilayer SAW device being studied by J Pollanen.

### Transport anomalies at other total filling fractions

The bilayer quantum Hall state at total filling fraction  $\nu_T = 1/2$  was discovered by Eisenstein et al. [1]. This state has not been as vigorously investigated experimentally

as the  $\nu_T = 1$  state. The Halperin wavefunction [59] for the  $\nu_T = 1/2$  state is

$$|\phi_{331}\rangle = \prod_{j < k} (z_j - z_k)^3 \prod_{r < s} (w_r - w_s)^3 \prod_{j,r} (z_j - w_r)^1 e^{-\frac{1}{4} \sum_j |z_j|^2 + \sum_r |w_r|^2}. \quad (6.20)$$

Measurements of Hall resistance in counterflow configuration and Hall drag might provide insights into the nature of correlations present in this state.

In conclusion, the bilayer quantum Hall state at  $\nu_T = 1$  is a remarkable example of exciton condensation that has been revealed through several exotic transport anomalies, and yet questions about the existence of an *ac*-Josephson effect and Fraunhofer diffraction pattern in tunneling remain. With the emergence of graphene and topological insulators, there have been several proposals of exciton condensation in graphene-boronitride-graphene Vanderwaal heterostructures [153, 154, 155, 156, 157, 158, 159, 160] and between surface states of 3D topological insulators [161]. All these offer exciting new possibilities.

# Appendix A

## List of samples

- sample 1: 7-12-99.1JJ

The Corbino counterflow experiment by Finck et al. [17, 6], the Coulomb drag and tunneling experiments reported in this thesis were also done on the same sample. The as grown mobility of this sample was  $\approx 1 \times 10^6 \text{ cm}^2/(\text{Vs})$ . The total electron density was  $11 \times 10^{10} \text{ cm}^{-2}$ . The zero magnetic field tunneling conductance was  $1.3 \mu\text{S}$  for an annular ring of 1.4 mm outer diameter and 1.0 mm inner diameter.

- sample 2: 06-05-01.2F This sample was patterned into a  $250 \mu\text{m} \times 250 \mu\text{m}$  cross. It showed a tunneling conductance of  $0.6 \mu\text{S}$ . All the ohmics and top gates worked. However, the backgates were hysteretic which was attributed to the presence of an etch stop layer in this heterostructure. The as grown density of the sample was  $11 \times 10^{10} \text{ cm}^{-2}$ . This sample showed a decent  $\nu_T = 1$  tunneling peak at 300 mK. The back gate hysteresis was however a cause of concern.

- sample 3: 11-12-01.1-QUADI-F

All the ohmic contacts and top gates worked satisfactorily for this device. Two out of four arm backgates were strongly hysteretic. Also, the sample was found to be strongly tunneling. The zero magnetic field tunneling resistance was  $33 \mu\text{S}$  at 300 mK for a  $550 \mu\text{m} \times 675 \mu\text{m}$  tunnel junction which was broader compared to 7-12-99.1JJ . It showed a fairly decent  $\nu_T = 1$ . The mobility of the bottom

layer for this sample was  $\approx 1.1 \times 10^6 \text{ cm}^2/(\text{Vs})$  and it had a nominal density of  $0.69 \times 10^{11}$  per layer.

- sample 4: 10-30-01.1-QUADII-F

The as grown mobility of the bottom layer was found low at  $\approx 0.144 \times 10^6 \text{ cm}^2/(\text{Vs})$ . The mobility of the top layer was reasonable at  $\approx 0.725 \times 10^6 \text{ cm}^2/(\text{Vs})$ . The total electron density was  $11.6 \times 10^{10} \text{ cm}^{-2}$ . All the top and bottom gates showed satisfactory gate characteristics. The zero magnetic field tunneling resistance was  $7.14 \mu\text{S}$  at 300 mK for a  $550 \mu\text{m} \times 675 \mu\text{m}$  tunnel junction and was too broad compared to 7-12-99.1JJ, indicating the low mobility. It showed a fairly decent  $\nu_T = 1$  and quantum Hall transport.

## Appendix B

# Fabrication of photon assisted tunneling device

For the photon assisted tunneling device, standard fabrication recipes were followed with minor modifications. Fig. 6.7 in Chapter 6 is example of a device fabricated following the procedures described below.

### 1. Top-side processing

#### (a) Mesa etch

- i. A 5 mm × 5 mm bilayer sample is cleaved.
- ii. The sample is rinsed with acetone and isopropyl alcohol and blow dried with nitrogen gas.
- iii. AZ 5214 E photoresist is spun at 5000 rpm for 30 seconds.
- iv. The photoresist is baked at 100 ° C for 45 seconds.
- v. A UV exposure is done of the mesa pattern at 15 mW/cm<sup>2</sup> for 30 seconds.
- vi. It is developed in developer solution AZ 400K : DI (1:4) for 1 minute.
- vii. A postbake is done at 100 ° C for 1 minute and 15 seconds.
- viii. An etch of GaAs is done in freshly prepared H<sub>2</sub>O (100 mL): H<sub>3</sub>PO<sub>4</sub> (10 mL): H<sub>2</sub>O<sub>2</sub> (2 mL) for 6 minutes 30 seconds.
- ix. Immediately, the device is immersed in 2 beakers of de-ionized (DI) water.

- x. Liftoff is done in n-butyl acetate at 75 ° C for 15 minutes.
- xi. Device is rinsed in isopropyl alcohol.
- xii. The mesa etch height is ascertained using the Dektak.
- xiii. A picture of the device is taken.

(b) **Ohmics**

- i. The sample is rinsed with acetone and isopropyl alcohol and blow dried with nitrogen gas.
- ii. AZ 5214 E photoresist is spun at 5000 rpm for 30 seconds.
- iii. Photoresist is baked at 100 ° C for 45 seconds.
- iv. A UV exposure is done of the ohmic pattern at 15 mW/cm<sup>2</sup> for 30 seconds.
- v. Device is placed in developer solution AZ 400K: DI (1:4) for 1 minute.
- vi. Ni/AuGe (135 Å/1600 Å) is evaporated as ohmics.
- vii. Liftoff is done in n-butyl acetate at 75 ° C for 15 minutes.
- viii. Device is rinsed in isopropyl alcohol.
- ix. The annealing step is described here.
  - A. The chip is placed in the center of the strip.
  - B. It is purged for 5 minutes.
  - C. It is annealed at 440 °C for 15 minutes.
  - D. It is cooled down to room temperature.
- x. After the ohmics are annealed, a picture is taken of the device.

(c) **Nichrome interconnects**

- i. The sample is rinsed with acetone and isopropyl alcohol and blow dried with nitrogen gas.
- ii. AZ 5214 E photoresist is spun at 5000 rpm for 30 seconds.
- iii. Photoresist is baked at 100 ° C for 45 seconds.
- iv. A UV exposure of the nichrome interconnect pattern is done at 15 mW/cm<sup>2</sup> for 30 seconds.

- v. Sample is placed in developer solution AZ 400K : DI (1 : 4) for 1 minute.
- vi. 500 Å of nichrome is evaporated.
- vii. Liftoff is done in n-butyl acetate at 75 ° C for 15 minutes.
- viii. Sample is rinsed in isopropyl alcohol.
- ix. A picture is taken.

(d) **Aluminium topgates and microstrip ground plane**

Aluminium evaporation should be the last step of the top side processing as the developer solution AZ 400K : DI (1 : 4) has KOH and etches aluminium.

- i. The sample is rinsed with acetone and isopropyl alcohol and blow dried with nitrogen gas.
- ii. AZ 5214 E photoresist is spun at 5000 rpm for 30 seconds.
- iii. Photoresist is baked at 100 ° C for 45 seconds.
- iv. A UV exposure is done of the topgate pattern at 15 mW/cm<sup>2</sup> for 30 seconds.
- v. Sample is placed in developer solution AZ 400K : DI (1:4) for 1 minute.
- vi. A UV exposure is done of the microstrip ground plane pattern at 15 mW/cm<sup>2</sup> for 30 seconds.
- vii. Sample is placed in developer solution AZ 400K : DI (1:4) for 1 minute.
- viii. A UV exposure is done of the trainglular pattern at 15 mW/cm<sup>2</sup> for 30 seconds.
- ix. Sample is placed in developer solution AZ 400K : DI (1:4) for 1 minute.
- x. 1600 Å of aluminium is evaporated.
- xi. Liftoff is done in n-butyl acetate at 75 ° C for 15 minutes.
- xii. Sample is rinsed in isopropyl alcohol.
- xiii. A picture of the device is taken.

## 2. Back-side processing

### (a) Thinning

- i. Aluminium is removed on the quartz disc in KOH : DI solution.
- ii. KOH etches away aluminium. So preferably this is done a day before and left in a large beaker of DI. Then the quartz disc is left overnight inside the DI.
- iii. The quartz disc is placed on the hot plate at  $75^{\circ}\text{C}$  (setting 3).
- iv. Four pieces of wax are placed on the quartz disc to become molten. Three of them are placed on the vertices of an equilateral triangle and another at the center.
- v. The sample is placed topside face down on the central molten wax. With a wooden applicator, the sample is placed gently to spread the molten wax into a thin film that keeps the sample glued onto the quartz disc. Care is taken not to slip or else one might scratch the top side of the sample.
- vi. The starting thickness of the bilayer GaAs sample is measured.
- vii. Three pieces of scrap GaAs of similar thickness as the bilayer sample are identified. These are placed on the three vertices of the equilateral triangle. The excess wax is removed by acetone wetted cotton tipped applicator. This is a modification to the procedure followed earlier. It helps in reducing etching on the edges of the sample.
- viii. The bromine-methanol etch needs to be done with caution and sufficient protection. It has to be done in the acid hood. Acetone or isopropyl alcohol should never be allowed in the acid hood. Sufficient protection should be adopted like wearing lab coat, apron, heavy neoprene gloves, and face shield.
- ix. Inside the acid hood, the Bromine-Methanol etch solution is mixed in the ratio 80 mL Methanol : 5 mL Bromine. Bromine should be poured into methanol and not vice versa.

- x. The square glass slab is wrapped in a clean room wipe and taped down at the other side. No wrinkles should be present.
- xi. The quartz piece sticks to the teflon chuck under surface tension of water droplets applied between the quartz piece and the teflon chuck.
- xii. The side marked with a hole is the deeper end. The quartz disc is inserted into this end in the beginning. This deeper end only allows the etching to proceed to a certain thickness. Then it stops before the desired thickness of  $50\ \mu\text{m}$  is achieved. The idea is that this will allow all the 4 GaAs pieces to be etched down to the same thickness. This was however not found to be the case in most occasions.
- xiii. The clean room wipe should be wetted each time with bromine methanol solution before one starts swiping. The teflon chuck is rubbed against the Bromine wetted clean room wipe making figure of eight.
- xiv. The Onno sokki gauge is used to measure the thickness.
- xv. Once the sample cannot be thinned down any further, the quartz disc is placed in the shallower end of the teflon chuck.
- xvi. Whenever the swiping is stopped and the quartz disc removed, it should be immediately washed with flowing DI water. This will prevent holes from forming in the GaAs.
- xvii. The sample is thinned down to  $50\ \mu\text{m} \pm 5\ \mu\text{m}$  in the center of the bilayer device. This measurement should be done at the center with respect to all four sides.
- xviii. After completion of the thinning process, a picture is taken.

(b) **Nichrome interconnects**

- i. The sample is rinsed with acetone and isopropyl alcohol and blow dried with nitrogen gas.
- ii. AZ 5214 E photoresist is spun at 5000 rpm for 30 seconds.
- iii. Photoresist is baked at  $100\ ^\circ\text{C}$  for 45 seconds.

- iv. A UV exposure is done of the nichrome interconnect pattern at 15 mW/cm<sup>2</sup> for 30 seconds.
- v. Sample is placed in developer solution AZ 400 K : DI (1:4) for 1 minute.
- vi. 500 Å of nichrome is evaporated.
- vii. Liftoff is done in n-butyl acetate at 75 ° C for 15 minutes.
- viii. Sample is rinsed in isopropyl alcohol.

(c) **Aluminium backgates and central conductor of microstrip line**

- i. The sample is rinsed with acetone and isopropyl alcohol and blow dry with nitrogen gas.
- ii. AZ 5214 E photoresist is spin coated at 5000 rpm for 30 seconds.
- iii. Photoresist is baked at 100 ° C for 45 seconds.
- iv. A UV exposure is done of the topgate pattern at 15 mW/cm<sup>2</sup> for 30 seconds.
- v. Sample is placed in developer solution AZ 400K : DI (1:4) for 1 minute.
- vi. A UV exposure is done of the microstrip central conductor pattern at 15 mW/cm<sup>2</sup> for 30 seconds.
- vii. Sample is placed in developer solution AZ 400K : DI (1:4) for 1 minute.
- viii. A UV exposure is done of the cone pattern at 15 mW/cm<sup>2</sup> for 30 seconds.
- ix. Sample is placed in developer solution AZ 400K : DI (1:4) for 1 minute.
- x. 1600 Å of aluminium is evaporated.
- xi. Liftoff is done in n-butyl acetate at 75 ° C for 15 minutes.
- xii. Sample is rinsed in isopropyl alcohol.

(d) **Wax removal**

- i. A filter paper is placed in a petridish.
- ii. A magnetic stirrer is placed on it after being washed in DI water.
- iii. The quartz disc is placed with the sample facing down.

- iv. The petridish is filled with acetone. After 3 hours, the sample will fall off into the filter paper.
- v. The sample should be left undisturbed until it falls off.
- vi. The thinned sample should be only manoeuvred with filter paper.
- vii. A few drops of acetone are put on the thinned sample.
- viii. A filter paper is placed to soak up the acetone on the thinned sample.
- ix. This process is repeated for cleaning both sides of the thinned sample a few times.
- x. The thinned sample should never be sprayed with N<sub>2</sub> gas. This will lead to cracks in the sample.

(e) **Wire-up**

This step requires minute attention as the thinned sample is fragile.

- i. The teflon vacuum chuck used for wire-up should be first cleaned with acetone and IPA.
- ii. The thinned sample is placed top side facing up and held down with vacuum.
- iii. Indium blobs are placed on the soldering pads on thinned sample.
- iv. Pretinned gold wires are attached at 550 ° F onto the indium blob.
- v. Tugging gently on the indium wires helps to make sure the wires do not fall off.
- vi. Now the thinned sample is turned upside down to solder onto the backside. It should be held by vacuum before attempting to solder.
- vii. Indium solder to the triangle on the microstrip line.
- viii. The two microstrip line wires are trimmed really short.
- ix. The sample hangs face down onto a beaker with a few of its gold wires soldered to the rim of the beaker.
- x. The two parts of silver epoxy are mixed in equal weight ration of 2 gm each.

- xi. A sharpened wooden applicator is used to put tiny silver blobs on the central and arm bottom gates
- xii. The silver epoxy is cured for 1 hour. The curing temperature is chosen to be  $100^{\circ}\text{C}$  to keep it below the melting point of indium.
- xiii. After attaching all the topside and backside wires, pictures are taken of both sides.
- xiv. The thinned sample is mounted onto the gold plated silver sample holder and the premounted coplanar waveguide.
- xv. It should be possible to keep the sample flat to less than a degree by adjusting the gold wires. Detailed steps are explained below:
  - A. A laser light is focussed at an angle on the coplanar waveguide. The reflected light from the coplanar waveguide is marked on the ceiling.
  - B. The sample mount is adjusted to place the thinned sample under the laser light.
  - C. The sample is adjusted by the wires to see the reflected spot from the device coincide with its previous position due to the coplanar waveguide. In order to find which wires need to be pulled on, one can orient the entire sample mount to see how to coincide the laser spots.
  - D. Once the two laser spots coincide, the thinned sample is in plane with the coplanar waveguide.

## Appendix C

# Fabrication and measuring insertion loss of coplanar waveguide

A coplanar waveguide is designed that would act as an on-chip *dc* block for the outer conductor and has negligible leakage upto 1 V. Fig. 6.8 in Chapter 6 is an image of such a coplanar waveguide. Hence HD 8820 was chosen as the dielectric as it has very high dielectric breakdown voltage. The insertion loss of the device was optimized to be 0 db - 2 db in the range 1 GHz - 10 GHz range. The coplanar waveguide also served the important purpose of thermally heat sinking the inner and outer conductors of the *RF* coax cable at the mixing chamber temperature. The design of the coplanar waveguide was done using Sonet-lite software to be impedance matched to 50  $\Omega$ . The central conductor was made 300  $\mu\text{m}$  wide, ground planes 1000  $\mu\text{m}$  wide and the gap in-between the inner conductor and the ground planes was 350  $\mu\text{m}$ . The ground planes had a 200  $\mu\text{m}$  discontinuity. The dielectric is patterned to be a rectangle of 2200  $\mu\text{m} \times 3400 \mu\text{m}$ . The metal was chosen to be aluminium after experimenting with Cr/Au for sometime. But Cr/Au is problematic because during the  $N_2$  cure step of 60 minutes at 320  $^\circ\text{C}$ , Cr/Au diffuses in GaAs like an ohmic material and becomes  $\approx$  10 times more resistive. This leads to significant insertion loss. Aluminium was found to have none of these problems. Crosslinked PMMA dielectric was also explored but some devices had breakdown voltage  $< 1$  V.

### 1. Nichrome stub

- (a) A 5 mm × 9.5 mm bare GaAs piece is cleaved.
- (b) In order to get rid of every tiny spec of dust on the surface of the sample, it is sonicated in acetone.
- (c) The sample is rinsed with acetone and isopropyl alcohol and blow dried with nitrogen gas.
- (d) AZ 5214 E photoresist is spin-coated at 5000 rpm for 30 seconds.
- (e) Photoresist is baked at 100 ° C for 45 seconds.
- (f) A UV exposure is done of the coplanar waveguide bottom pattern at 15 mW/cm<sup>2</sup> for 30 seconds.
- (g) Sample is developed in AZ 400 K : DI (1 : 4) solution for 1 minute.
- (h) 150 Å of nichrome is evaporated.
- (i) Liftoff is done in n-butyl acetate at 75 ° C for 15 minutes.
- (j) Sample is rinsed in isopropyl alcohol.

## 2. First aluminium deposition

- (a) The sample is rinsed with acetone and isopropyl alcohol and dried with nitrogen gas.
- (b) AZ 5214 E photoresist is spun at 5000 rpm for 30 seconds.
- (c) Photoresist is baked at 100 ° C for 45 seconds.
- (d) A UV exposure is done of the coplanar waveguide bottom pattern at 15 mW/cm<sup>2</sup> for 30 seconds.
- (e) Sample is developed in AZ 400 K : DI (1 : 4) solution for 1 minute.
- (f) 1600 Å of aluminium is evaporated.
- (g) Liftoff is done in n-butyl acetate at 75 ° C for 15 minutes.
- (h) Sample is rinsed in isopropyl alcohol.

## 3. Patterning dielectric

- (a) The sample is rinsed with acetone and isopropyl alcohol and blow dried with nitrogen gas.
- (b) HD 8820 polyimide is spun at 5000 rpm for 45 seconds.
- (c) Polyimide is softbaked at  $120^{\circ}\text{C}$  for 3 minutes.
- (d) A UV exposure is done of the dielectric pattern at  $15\text{ mW/cm}^2$  for 3 minutes.
- (e) Polyimide is developed in AZ 400K : DI (1:4) solution for 1 minute. This development time is crucial. Because the developer is known to etch aluminium. Minimizing development time by increasing UV exposure time is recommended.
- (f) The polyimide is cured in nitrogen furnace (It is a good idea to do this step overnight)
  - i. The furnace is purged with 1 SLM of high purity nitrogen gas for 20 mins.
  - ii. The furnace is ramped to  $320^{\circ}\text{C}$  at  $3^{\circ}\text{C/min}$ .
  - iii. It is held at  $320^{\circ}\text{C}$  for 60 minutes.
  - iv. It is ramped down to room temperature at  $3^{\circ}\text{C/min}$ . In reality, this will take longer to cool down.
  - v. The coplanar waveguide sample is taken out once it has cooled down to room temperature.

#### 4. Second aluminium deposition

- (a) The sample is rinsed in acetone and isopropyl alcohol. Blow dried with nitrogen gas. It should become absolutely clean.
- (b) AZ 5214 E photoresist is spin coated at 5000 rpm for 30 seconds.
- (c) Photoresist is baked at  $100^{\circ}\text{C}$  for 45 seconds.
- (d) A UV exposure is done of the coplanar waveguide top pattern at  $15\text{ mW/cm}^2$  for 30 seconds.

- (e) The photoresist is developed in AZ 400 K : DI (1:4) solution for 1 minute.
- (f) 1600 Å of aluminium is evaporated.
- (g) Liftoff is done in n-butyl acetate at 75 ° C for 15 minutes.
- (h) Sample is rinsed in isopropyl alcohol.

#### 5. Insertion loss test

- (a) The coplanar waveguide is connected to the RF tester with indium soldered gold wires.
- (b) With the H83732B signal generator, an  $RF$  power = -10 dbm is applied.
- (c) The frequency is swept from 1 GHz to 10 GHz in steps of 1 GHz.
- (d) The net insertion loss is measured.
- (e) The actual insertion loss due to the coplanar waveguide is measured by subtracting the insertion loss in the coax cables. The coplanar waveguide made with the above recipe showed an insertion loss of 0 db - 2 db in the frequency range of 1 GHz to 10 GHz.

#### 6. Leakage

This is measured at 4.2 K. 10 V applied across the discontinuity on the ground plane showed a gate leakage of 3 nA. In another device which had a 200  $\mu\text{m}$  discontinuity on the central conductor as well, a 40 V across this discontinuity only gave a gate leakage of  $\leq 1$  nA.

# Bibliography

- [1] Eisenstein, J. P., Boebinger, G. S., Pfeiffer, L. N., West, K. W., and He, S. *Phys. Rev. Lett.* **68**(9), 1383 (1992).
- [2] Spielman, I. B., Eisenstein, J. P., Pfeiffer, L. N., and West, K. W. *Phys. Rev. Lett.* **84**(25), 5808 (2000).
- [3] Sodemann, I., Chen, H., and MacDonald, A. H. *arXiv preprint arXiv:1411.0008* (2014).
- [4] Fox, M. and Ispasoiu, R. *Springer Handbook of Electronic and Photonic Materials*. (2007).
- [5] Eisenstein, J. P., Pfeiffer, L. N., and West, K. W. *Appl. Phys. Lett.* **57**(22), 2324–2326 (1990).
- [6] Finck, A. D. K. *Studies of exciton condensation and transport in quantum Hall bilayers*. PhD thesis, California Institute of Technology, (2012).
- [7] Stormer, H. L. *Rev. Mod. Phys.* **71**(4), 875 (1999).
- [8] Murphy, S. Q., Eisenstein, J. P., Boebinger, G. S., Pfeiffer, L. N., and West, K. W. *Phys. Rev. Lett.* **72**(5), 728 (1994).
- [9] Spielman, I. B., Eisenstein, J. P., Pfeiffer, L. N., and West, K. W. *Phys. Rev. Lett.* **87**(3), 036803 (2001).
- [10] Kellogg, M., Eisenstein, J. P., Pfeiffer, L. N., and West, K. W. *Phys. Rev. Lett.* **93**(3), 036801 (2004).

- [11] Eisenstein, J. P., Pfeiffer, L. N., and West, K. W. *Appl. Phys. Lett.* **58**(14), 1497–1499 (1991).
- [12] Eisenstein, J. P., Pfeiffer, L. N., and West, K. W. *Phys. Rev. Lett.* **69**(26), 3804 (1992).
- [13] Steinbach, A., Joyez, P., Cottet, A., Esteve, D., Devoret, M. H., Huber, M. E., and Martinis, J. M. *Phys. Rev. Lett.* **87**(13), 137003 (2001).
- [14] Gramila, T. J., Eisenstein, J. P., MacDonald, A. H., Pfeiffer, L. N., and West, K. W. *Phys. Rev. Lett.* **66**(9), 1216 (1991).
- [15] Lilly, M. P., Eisenstein, J. P., Pfeiffer, L. N., and West, K. W. *Phys. Rev. Lett.* **80**(8), 1714 (1998).
- [16] Kellogg, M., Spielman, I. B., Eisenstein, J. P., Pfeiffer, L. N., and West, K. W. *Phys. Rev. Lett.* **88**(12), 126804 (2002).
- [17] Finck, A. D. K., Eisenstein, J. P., Pfeiffer, L. N., and West, K. W. *Phys. Rev. Lett.* **106**(23), 236807 (2011).
- [18] Su, J. J. and MacDonald, A. H. *Nature Physics* **4**(10), 799–802 (2008).
- [19] Tien, P. K. and Gordon, J. P. *Phys. Rev.* **129**(2), 647 (1963).
- [20] Kohlmann, J. and Behr, R. *Superconductivity - Theory and Applications* (2011).
- [21] Hyart, T. and Rosenow, B. *Phys. Rev. Lett.* **110**(7), 076806 (2013).
- [22] Schuster, D. I. *Circuit quantum electrodynamics.* (2007).
- [23] Wen, X. G. and Zee, A. *EPL (Europhysics Letters)* **35**(3), 227 (1996).
- [24] Bose, S. N. *Z. phys* **26**(3), 178 (1924).
- [25] Einstein, A. *Quantentheorie des einatomigen idealen Gases.* Akademie der Wissenschaften, in Kommission bei W. de Gruyter, (1924).

- [26] Einstein, A. *Preuss. Akad. Wiss., Phys. Math. Kl* **3**, 18 (1925).
- [27] Onnes, H. K. *Commun. Phys. Lab. Univ. Leiden* **12**(120), 1 (1911).
- [28] Onnes, H. K. *Commun. Phys. Lab. Univ. Leiden* **122**, 124 (1911).
- [29] Kapitza, P. *Nature* **141**(3558), 74 (1938).
- [30] Bardeen, J., Cooper, L. N., and Schrieffer, J. R. *Phys. Rev.* **108**(5), 1175 (1957).
- [31] Blatt, J. M., Böer, K. W., and Brandt, W. *Phys. Rev.* **126**(5), 1691 (1962).
- [32] Lozovik, Y. E. and Yudson, V. I. *JETP lett* **22**(11), 274–276 (1975).
- [33] Lozovik, Y. E. and Yudson, V. I. *Zh. Eksp. Teor. Fiz* **71**, 738–753 (1976).
- [34] Lerner, I. V. and Lozovik, Y. E. *Zh. Eksp. Teor. Fiz* **80**, 1488–1495 (1981).
- [35] Klitzing, K. V., Dorda, G., and Pepper, M. *Phys. Rev. Lett.* **45**(6), 494 (1980).
- [36] Tsui, D. C., Stormer, H. L., and Gossard, A. C. *Phys. Rev. Lett.* **48**(22), 1559 (1982).
- [37] Stern, A., Girvin, S. M., MacDonald, A. H., and Ma, N. *Phys. Rev. Lett.* **86**(9), 1829 (2001).
- [38] Kellogg, M., Eisenstein, J. P., Pfeiffer, L. N., and West, K. W. *Phys. Rev. Lett.* **90**(24), 246801 (2003).
- [39] Tiemann, L., Dietsche, W., Hauser, M., and von Klitzing, K. *New Journal of Physics* **10**(4), 045018 (2008).
- [40] Tiemann, L., Lok, J. G. S., Dietsche, W., von Klitzing, K., Muraki, K., Schuh, D., and Wegscheider, W. *Phys. Rev. B* **77**(3), 033306 (2008).
- [41] Tiemann, L., Lok, J. G. S., Dietsche, W., von Klitzing, K., Muraki, K., Schuh, D., and Wegscheider, W. *Physica E: Low-dimensional Systems and Nanostructures* **40**(5), 1034–1037 (2008).

- [42] Tiemann, L., Yoon, Y., Dietsche, W., Von Klitzing, K., and Wegscheider, W. *Phys. Rev. B* **80**(16), 165120 (2009).
- [43] Tiemann, L., Dietsche, W., Hauser, M., and von Klitzing, K. *International Journal of Modern Physics B* **23**(12n13), 2596–2602 (2009).
- [44] Büttiker, M., Imry, Y., Landauer, R., and Pinhas, S. *Phys. Rev. B* **31**(10), 6207 (1985).
- [45] Büttiker, M. *Phys. Rev. Lett.* **57**(14), 1761 (1986).
- [46] Jain, J. K. *Phys. Rev. Lett.* **63**(2), 199 (1989).
- [47] Willett, R., Eisenstein, J. P., Störmer, H. L., Tsui, D. C., Gossard, A. C., and English, J. H. *Phys. Rev. Lett.* **59**(15), 1776 (1987).
- [48] Eisenstein, J. P., Willett, R., Stormer, H. L., Tsui, D. C., Gossard, A. C., and English, J. H. *Phys. Rev. Lett.* **61**(8), 997 (1988).
- [49] Nandi, D., Khaire, T., Finck, A. D. K., Eisenstein, J. P., Pfeiffer, L. N., and West, K. W. *Phys. Rev. B* **88**(16), 165308 (2013).
- [50] Cho, A. Y. and Arthur, J. R. *Progress in solid state chemistry* **10**, 157–191 (1975).
- [51] Manfra, M. *Annu. Rev. Condens. Matter Phys.* **5** (2014).
- [52] Panish, M. B. *Science* **208**(4446), 916–922 (1980).
- [53] Dingle, R., Störmer, H. L., Gossard, A. C., and Wiegmann, W. *Appl. Phys. Lett.* **33**(7), 665–667 (1978).
- [54] Van der Pauw, L. J. *Philips technical review* **20**(8), 220–224 (1958).
- [55] Jain, J. K. *Composite fermions*. Cambridge University Press, (2007).
- [56] Ashcroft, N. W. and Mermin, N. D. *Solid State Physics (Holt, Rinehart and Winston, New York, 1976)*. (2005).

- [57] Laughlin, R. B. *Phys. Rev. Lett.* **50**(18), 1395 (1983).
- [58] Lilly, M. P., Cooper, K. B., Eisenstein, J. P., Pfeiffer, L. N., and West, K. W. *Phys. Rev. Lett.* **82**(2), 394 (1999).
- [59] Halperin, B. I. *Helv. Phys. Acta* **56**(1-3), 75 (1983).
- [60] Chakraborty, T. and Pietiläinen, P. *Phys. Rev. Lett.* **59**(24), 2784 (1987).
- [61] Yang, K., Moon, K., Zheng, L., MacDonald, A. H., Girvin, S. M., Yoshioka, D., and Zhang, S. C. *Phys. Rev. Lett.* **72**(5), 732 (1994).
- [62] Moon, K., Mori, H., Yang, K., Girvin, S. M., MacDonald, A. H., Zheng, L., Yoshioka, D., and Zhang, S. C. *Phys. Rev. B* **51**(8), 5138 (1995).
- [63] Yang, K., Moon, K., Belkhir, L., Mori, H., Girvin, S. M., MacDonald, A. H., Zheng, L., and Yoshioka, D. *Phys. Rev. B* **54**(16), 11644 (1996).
- [64] Ezawa, Z. F. *Phys. Rev. B* **51**(16), 11152 (1995).
- [65] Eisenstein, J. P., Finck, A. D. K., Nandi, D., Pfeiffer, L. N., and West, K. W. In *Journal of Physics: Conference Series*, volume 456, 012009. IOP Publishing, (2013).
- [66] Moskaleiko, S. A. *Soviet Physics-Solid State* **4**(1), 199–204 (1962).
- [67] Keldysh, L. V. and Kopaev, Y. V. *SOVIET PHYSICS SOLID STATE, USSR* **6**(9), 2219 (1965).
- [68] Wen, X. G. and Zee, A. *Phys. Rev. Lett.* **69**(12), 1811 (1992).
- [69] Wen, X. G. and Zee, A. *Phys. Rev. B* **47**(4), 2265 (1993).
- [70] Fertig, H. A. *Phys. Rev. B* **40**(2), 1087 (1989).
- [71] Spielman, I. B. *Evidence for the Josephson effect in quantum Hall bilayers*. PhD thesis, California Institute of Technology, (2004).

- [72] Tutuc, E., Shayegan, M., and Huse, D. A. *Phys. Rev. Lett.* **93**(3), 036802 (2004).
- [73] Wiersma, R. D., Lok, J. G. S., Kraus, S., Dietsche, W., Von Klitzing, K., Schuh, D., Bichler, M., Tranitz, H. P., and Wegscheider, W. *Phys. Rev. Lett.* **93**(26), 266805 (2004).
- [74] Yoon, Y., Tiemann, L., Schmult, S., Dietsche, W., von Klitzing, K., and Wegscheider, W. *Phys. Rev. Lett.* **104**(11), 116802 (2010).
- [75] Fogler, M. M. and Wilczek, F. *Phys. Rev. Lett.* **86**(9), 1833 (2001).
- [76] Joglekar, T. N. and MacDonald, A. H. *Phys. Rev. Lett.* **87**(19), 196802 (2001).
- [77] Fertig, H. A. and Straley, J. P. *Phys. Rev. Lett.* **91**(4), 046806 (2003).
- [78] Rossi, E., Núñez, A. S., and MacDonald, A. H. *Phys. Rev. Lett.* **95**(26), 266804 (2005).
- [79] Hyart, T. and Rosenow, B. *Phys. Rev. B* **83**(15), 155315 (2011).
- [80] Finck, A. D. K., Champagne, A. R., Eisenstein, J. P., and Pfeiffer, L. N. and West, K. W. *Phys. Rev. B* **78**(7), 075302 (2008).
- [81] Murphy, S. Q., Eisenstein, J. P., Pfeiffer, L. N., and West, K. W. *Phys. Rev. B* **52**(20), 14825 (1995).
- [82] Ashoori, R. C., Lebens, J. A., Bigelow, N. P., and Silsbee, R. H. *Phys. Rev. Lett.* **64**(6), 681 (1990).
- [83] Ashoori, R. C., Lebens, J. A., Bigelow, N. P., and Silsbee, R. H. *Phys. Rev. B* **48**(7), 4616 (1993).
- [84] Balents, L. and Radzihovsky, L. *Phys. Rev. Lett.* **86**(9), 1825 (2001).
- [85] Fertig, H. A. and Murthy, G. *Phys. Rev. Lett.* **95**(15), 156802 (2005).
- [86] Wang, Z. *Phys. Rev. Lett.* **94**(17), 176804 (2005).

- [87] Fertig, H. A. and Murthy, G. *Solid state commun.* **140**(2), 83–87 (2006).
- [88] Ambegaokar, V. and Halperin, B. I. *Phys. Rev. Lett.* **22**(25), 1364 (1969).
- [89] Spielman, I. B., Kellogg, M., Eisenstein, J. P., Pfeiffer, L. N., and West, K. W. *Phys. Rev. B* **70**(8), 081303 (2004).
- [90] Huse, D. A. *Phys. Rev. B* **72**(6), 064514 (2005).
- [91] Bourassa, J., Roostaei, B., Côté, R., Fertig, H. A., and Mullen, K. *Phys. Rev. B* **74**(19), 195320 (2006).
- [92] Roostaei, B., Mullen, K. J., Fertig, H. A., and Simon, S. H. *Phys. Rev. Lett.* **101**(4), 046804 (2008).
- [93] Eastham, P. R., Cooper, N. R., and Lee, D. K. K. *Phys. Rev. B* **80**(4), 045302 (2009).
- [94] Sun, J., Murthy, G., Fertig, H. A., and Bray-Ali, N. *Phys. Rev. B* **81**(19), 195314 (2010).
- [95] Eastham, P. R., Cooper, N. R., and Lee, D. K. K. *Phys. Rev. Lett.* **105**(23), 236805 (2010).
- [96] Lee, D. K. K., Eastham, P. R., and Cooper, N. R. *Advances in Condensed Matter Physics* **2011** (2011).
- [97] Lay, T. S., Suen, Y. W., Manoharan, H. C., Ying, X., Santos, M. B., and Shayegani, M. *Phys. Rev. B* **50**(23), 17725 (1994).
- [98] Troyer, M. and Sachdev, S. *Phys. Rev. Lett.* **81**(24), 5418 (1998).
- [99] Sheng, D. N., Balents, L., and Wang, Z. *Phys. Rev. Lett.* **91**(11), 116802 (2003).
- [100] Eisenstein, J. P. and MacDonald, A. H. *Nature* **432**(7018), 691–694 (2004).
- [101] Champagne, A. R., Eisenstein, J. P., Pfeiffer, L. N., and West, K. W. *Phys. Rev. Lett.* **100**(9), 096801 (2008).

- [102] Ambegaokar, V. and Baratoff, A. *Phys. Rev. Lett.* **10**(11), 486 (1963).
- [103] Huang, X., Dietsche, W., Hauser, M., and von Klitzing, K. *Phys. Rev. Lett.* **109**(15), 156802 (2012).
- [104] Eisenstein, J. P. *Annu. Rev. Condens. Matter Phys.* **5**(1), 159–181 (2014).
- [105] Pogrebinskii, M. B. *Soviet Physics-Semiconductors* **11**(4), 372–376 (1977).
- [106] Price, P. J. *Physica B+ C* **117**, 750–752 (1983).
- [107] Rojo, A. G. *Journal of Physics: Condensed Matter* **11**(5), R31 (1999).
- [108] Tso, H. C., Vasilopoulos, P., and Peeters, F. M. *Phys. Rev. Lett.* **68**(16), 2516 (1992).
- [109] Gurevich, V. L., Pevzner, V. B., and Fenton, E. W. *Journal of Physics: Condensed Matter* **10**(11), 2551 (1998).
- [110] Ponomarenko, V. V. and Averin, D. V. *Phys. Rev. Lett.* **85**(23), 4928 (2000).
- [111] Debray, P., Zverev, V. N., Gurevich, V., Klesse, R., and Newrock, R. S. *Semiconductor science and technology* **17**(11), R21 (2002).
- [112] Pustilnik, M., Mishchenko, E. G., Glazman, L. I., and Andreev, A. V. *Phys. Rev. Lett.* **91**(12), 126805 (2003).
- [113] Fiete, G. A., Le Hur, K., and Balents, L. *Phys. Rev. B* **73**(16), 165104 (2006).
- [114] Tse, W. K. and Sarma, S. D. *Phys. Rev. B* **75**(4), 045333 (2007).
- [115] Laroche, D., Gervais, G., Lilly, M. P., and Reno, J. L. *Nature nanotechnology* **6**(12), 793–797 (2011).
- [116] Laroche, D., Gervais, G., Lilly, M. P., and Reno, J. L. *Science* **343**(6171), 631–634 (2014).
- [117] Jauho, A. P. and Smith, H. *Phys. Rev. B* **47**(8), 4420 (1993).

- [118] Zheng, L. and MacDonald, A. H. *Phys. Rev. B* **48**(11), 8203 (1993).
- [119] Flensberg, K. and Hu, B. Y. K. *Phys. Rev. B* **52**(20), 14796 (1995).
- [120] Kamenev, A. and Oreg, Y. *Phys. Rev. B* **52**(10), 7516 (1995).
- [121] Hu, B. Y. K. *Phys. Rev. Lett.* **85**(4), 820 (2000).
- [122] Croxall, A. F., Gupta, K. D., Nicoll, C. A., Thangaraj, M., Beere, H. E., Farrer, I., Ritchie, D. A., and Pepper, M. *Phys. Rev. Lett.* **101**(24), 246801 (2008).
- [123] Seamons, J. A., Morath, C. P., Reno, J. L., and Lilly, M. P. *Phys. Rev. Lett.* **102**(2), 026804 (2009).
- [124] Gramila, T. J., Eisenstein, J. P., MacDonald, A. H., Pfeiffer, L. N., and West, K. W. *Surface science* **263**(1), 446–450 (1992).
- [125] Gramila, T. J., Eisenstein, J. P., MacDonald, A. H., Pfeiffer, L. N., and West, K. W. *Phys. Rev. B* **47**(19), 12957 (1993).
- [126] Gramila, T. J., Eisenstein, J. P., MacDonald, A. H., Pfeiffer, L. N., and West, K. W. *Physica B: Condensed Matter* **197**(1), 442–448 (1994).
- [127] Bønsager, M. C., Flensberg, K., Hu, B. Y. K., and MacDonald, A. H. *Phys. Rev. B* **57**(12), 7085 (1998).
- [128] Badalyan, S. M. and Rössler, U. *Phys. Rev. B* **59**(8), 5643 (1999).
- [129] Noh, H., Zelakiewicz, S., Gramila, T. J., Pfeiffer, L. N., and West, K. W. *Phys. Rev. B* **59**(20), 13114 (1999).
- [130] Nandi, D., Finck, A. D. K., Eisenstein, J. P., Pfeiffer, L. N., and West, K. W. *Nature* **488**(7412), 481–484 (2012).
- [131] Fil, D. V. and Shevchenko, S. I. *Low Temperature Physics* **33**(9), 780–782 (2007).
- [132] Feynman, R. P. *Phys. Rev.* **94**(2), 262 (1954).

- [133] Kouwenhoven, L. P., Jauhar, S., Orenstein, J., McEuen, P. L., Nagamune, Y., Motohisa, J., and Sakaki, H. *Phys. Rev. Lett.* **73**(25), 3443 (1994).
- [134] Stafford, C. A. and Wingreen, N. S. *Phys. Rev. Lett.* **76**(11), 1916 (1996).
- [135] Kouwenhoven, L., Jauhar, S., McCormick, K., Dixon, D., McEuen, P., Nazarov, Y. V., Van der Vaart, N., and Foxon, C. *Physical Review B* **50**(3), 2019 (1994).
- [136] Josephson, B. D. *Phys. Lett.* **1**(7), 251–253 (1962).
- [137] Shapiro, S. *Phys. Rev. Lett.* **11**(2), 80 (1963).
- [138] Shapiro, S., Janus, A. R., and Holly, S. *Rev. Mod. Phys.* **36**(1), 223 (1964).
- [139] Josephson, B. D. *Rev. Mod. Phys.* **36**(1), 216 (1964).
- [140] Josephson, B. D. *Advances in Physics* **14**(56), 419–451 (1965).
- [141] Richards, P. L. and Anderson, P. W. *Phys. Rev. Lett.* **14**(14), 540 (1965).
- [142] Khorana, B. M. and Chandrasekhar, B. S. *Phys. Rev. Lett.* **18**(7), 230 (1967).
- [143] Richards, P. L. *Phys. Rev. A* **2**(4), 1532 (1970).
- [144] Sukhatme, K., Mukharsky, Y., Chui, T., and Pearson, D. *Nature* **411**(6835), 280–283 (2001).
- [145] Giovanazzi, S., Smerzi, A., and Fantoni, S. *Phys. Rev. Lett.* **84**(20), 4521 (2000).
- [146] Kasevich, M. A. *Science* **298**(5597), 1363–1368 (2002).
- [147] Levy, S., Lahoud, E., Shomroni, I., and Steinhauer, J. *Nature* **449**(7162), 579–583 (2007).
- [148] Ancilotto, F., Salasnich, L., and Toigo, F. *Phys. Rev. A* **79**(3), 033627 (2009).
- [149] Radzihovsky, L. and Gurarie, V. *Phys. Rev. A* **81**(6), 063609 (2010).
- [150] Dayem, A. and Martin, R. J. *Phys. Rev. Lett.* **8**(6), 246 (1962).

- [151] Grimes, C. C. and Shapiro, S. *Phys. Rev.* **169**(2), 397 (1968).
- [152] Willett, R. L., Ruel, R. R., West, K. W., and Pfeiffer, L. N. *Phys. Rev. Lett.* **71**(23), 3846 (1993).
- [153] Zhang, C. H. and Joglekar, Y. N. *Phys. Rev. B* **77**(23), 233405 (2008).
- [154] Min, H., Bistritzer, R., Su, J. J., and MacDonald, A. H. *Phys. Rev. B* **78**(12), 121401 (2008).
- [155] Seradjeh, B., Weber, H., and Franz, M. *Phys. Rev. Lett.* **101**(24), 246404 (2008).
- [156] Kharitonov, M. Y. and Efetov, K. B. *Phys. Rev. B* **78**(24), 241401 (2008).
- [157] Bistritzer, R. and MacDonald, A. H. *Phys. Rev. Lett.* **101**(25), 256406 (2008).
- [158] Berman, O. L., Lozovik, Y. E., and Gumbs, G. *Phys. Rev. B* **77**(15), 155433 (2008).
- [159] Kharitonov, M. Y. and Efetov, K. B. *Semiconductor Science and Technology* **25**(3), 034004 (2010).
- [160] Barlas, Y., Côté, R., Lambert, J., and MacDonald, A. H. *Phys. Rev. Lett.* **104**(9), 096802 (2010).
- [161] Seradjeh, B., Moore, J. E., and Franz, M. *Phys. Rev. Lett.* **103**(6), 066402 (2009).